Effective Date: April 22, 2011
Revision -

GSFC JPSS CMO
December 5, 2011
Released

Joint Polar Satellite System (JPSS) Ground Project
Code 474
474-00047

Joint Polar Satellite System (JPSS) VIIRS Sea Ice Characterization Algorithm Theoretical Basis Document (ATBD)

For Public Release

The information provided herein does not contain technical data as defined in the International Traffic in Arms Regulations (ITAR) 22 CFC 120.10. This document has been approved For Public Release to the NOAA Comprehensive Large Array-data Stewardship System (CLASS).

National Aeronautics and Space Administration

Goddard Space Flight Center
Greenbelt, Maryland

This page intentionally left blank.

Joint Polar Satellite System (JPSS)
VIIRS Sea Ice Characterization
Algorithm Theoretical Basis Document
(ATBD)

JPSS Electronic Signature Page

Prepared By:

Neal Baker
JPSS Data Products and Algorithms, Senior Engineering Advisor
(Electronic Approvals available online at (https://jpssmis.gsfc.nasa.gov/mainmenu_dsp.cfm)

Approved By:

Heather Kilcoyne
DPA Manager
(Electronic Approvals available online at (https://jpssmis.gsfc.nasa.gov/mainmenu_dsp.cfm)

Goddard Space Flight Center
Greenbelt, Maryland

This page intentionally left blank.

Preface

This document is under JPSS Ground AERB configuration control. Once this document is approved, JPSS approved changes are handled in accordance with Class I and Class II change control requirements as described in the JPSS Configuration Management Procedures, and changes to this document shall be made by complete revision.

Any questions should be addressed to:

JPSS Ground Project Configuration Management Office
NASA/GSFC
Code 474
Greenbelt, MD 20771

This page intentionally left blank.

Change History Log

Revision	Effective Date	Description of Changes (Reference the CCR & CCB/ERB Approve Date)
Original	04/22/2011	**474-CCR-11-0062:** This version baselines D41063, VIIRS Sea Ice Characterization Algorithm Theoretical Basis Document ATDB (REF Y2409), Rev F, dated 12/02/2009, as a JPSS document, version Rev –. This is the version that was approved for NPP launch. Per NPOESS CDFCB - External, Volume V – Metadata, doc number D34862-05, this has been approved for Public Release into CLASS. This CCR was approved by the JPSS Algorithm ERB on April 22, 2011.

This page intentionally left blank.

Northrop Grumman Space & Mission Systems Corp.
Space Technology
One Space Park
Redondo Beach, CA 90278

Engineering & Manufacturing Development (EMD) Phase
Acquisition & Operations Contract

CAGE NO. 11982

National Polar-Orbiting Operational Environmental Satellite System (NPOESS) VIIRS Sea Ice Characterization Algorithm Theoretical Basis Document (ref Y2409)

Document Date: 2 December 2009 **Document Number: D41063**
Revision: F

PREPARED BY:
Robert Mahoney, Models & Simulations

ELECTRONIC APPROVAL SIGNATURES:

Merit Shoucri, Models & Simulation Lead

Prepared by
Northrop Grumman Space Technology
One Space Park
Redondo Beach, CA 90278

Under
Contract No. F04701-02-C-0502

Prepared for
Department of the Air Force
NPOESS Integrated Program Office
C/O SMC/CIK
2420 Vela Way, Suite 1467-A8
Los Angeles AFB, CA 90245-4659

Northrop Grumman Space & Mission Systems Corp.
Space Technology
One Space Park
Redondo Beach, CA 90278

NORTHROP GRUMMAN

Raytheon

Revision/Change Record

Document Number D41063

Revision	Document Date	Revision/Change Description	Pages Affected
---	30 Sep. 2005	Initial Release – NGST Document number D41063 supersedes Raytheon Document number Y2409 Additionally, changes related to SPCR 870 for implementation of sub-granule processing (ECR A066) have been made.	29, 37, 118
A	18 Oct. 2006	Changes approved per ECR – A108 Rev-A Modifications under SPCR 1059. Deleted references to Ice Edge Location and Ice Concentration ARP and fresh water ice retrieval. Deleted references to Aerosol Model Index IP as a required input data set in table 5 and on page 30. Corrected processing flow figures 4-8. Deleted tunable parameter description tables in favor of referencing OAD documents where these tables are more appropriately described. Corrected references to regridded Ancillary data products to be moderate resolution instead of imagery resolution. Deleted table 12. Ice Reflectance LUT in favor OAD where this is more appropriately described. Deleted figures 9 & 10 processing flow diagrams. Deleted table 13 in favor or referencing the Ice Quality OAD. Deleted Ice Edge Location algorithm description. Corrected formatting problem with equation 3.3.5.1.2 present in previous version. Added reference to exception handling for pixels with good thermal data but missing reflectance tie points	TOC, 2, 7-8, 10-12, 18, 20-25, 29, 33-35, 37-38, 43-46, 49, 54-61, 63-64, 89, 96-100, 114
B	11 Dec 2006	Rev-B Modifications under SPCR 1103. Added references to include NAAPS based aerosols optical thickness (AOT) as the source for AOT data for night only granules Updated figure 4 on page 17 to include NAAPS data.. Updated table 5 on page 25 to emphasize VIIRS AOT IP data are for day granules. Added references on page 26 and 37 to user of NAAPS data for night only granules. Added entry in table 10 page 29 for NAAPS data. Added reference to NAAPS product description documentation on page 95.	17. 25, 26, 29, 37, 95
C	12 Feb. 2007	Rev-C Modification made under SPCR 1133 This SPCR authorizes the removal of all modification released as Rev B of this document. All references to NAAPS and night only granules has been removed. This document supersedes all modification made in Rev B.	17. 25, 26, 29, 37, 95
D	9 August 2007	Rev-D modifications made under SPCR 1174. Corrected an incorrect section number reference to the section for discussion of Snow Depth Climatology LUT. Section 3.3.2.3 corrected to refer to section 3.3.5.1.1 "Analytical Snow Depth/Ice Thickness LUT 1) Added NGST "D" number references for ATB documents throughout the document. 2) Corrected incorrect wavelengths listed for bands M15, M16 in table on page. Deleted table 4. 3) Reference VIIRS Radiometric Calibration ATBD instead of table 4 on page 4) Update revision section 5) Document header Rev D and date updated	1) p 29 2)pages 1,2,11-20 24-29, 35, 36,39,60 3)page 14 4) page 78 5) page 3 6) All

Northrop Grumman Space & Mission Systems Corp.
Space Technology
One Space Park
Redondo Beach, CA 90278

NORTHROP GRUMMAN

Raytheon

Revision/Change Record

Document Number D41063

Revision	Document Date	Revision/Change Description	Pages Affected
E	14 April 2008	Rev-E modifications made under SPCRs 1282; 1295 for removal of Multi-year ice classification and change of horizontal cell size from 3x3 to 2x2 pixel aggregation. 1) Modified abstract to reflect system specification requirement for ice classification. 2) Added Rev. E revision description as first paragraph of section 1.4 3) Updated NPOESS system specification (table 1) 4) Corrected error in section 2.4.1 describing pixels passed for processing. 5) Modified section 2.4.2 to reflect requirement to retrieve New/Young and All other ice. 6) Removed previous ice age IP from flow chart (figure 4) 7) Changed Ice Mask IP to Ice Quality Flags IP 8) Modified Sea Ice Age flow chart (figure 7) to reflect removal of Multi-year ice processing. 9) Removed reference to Multi-year processing 10) Added VIIRS 750 SDR to list of inputs, removed sea ice thickness LUT from list of inputs in table 5 and added description about use of moderated resolution for geolocation of the horizontal cells. 11) Clarified description for use of Cloud Optical Thickness 12) Updated section for Surface Temperature to ice classification, Clarified exclusion from process of probably cloudy pixels. Modified Land/Water mask criteria to state that EDR is report for oceans, for consistency with System Specfication. 13) Changed Ice Thickness LUT to Ice Age LUT in section on Ice Age/Thickness. Added wording "or data bases" to avoid restricting the source of the climatology snow depth to only a model based snow depth. 14) Eliminated Previous Ice Age from Table 10. 15) Modified second paragraph of section 3.3.1.2 to state ice age classification is for New/Young and All other ice. 16) Added clarification to definitions of the Sea Ice Range and Cloud Phase quality flags in section 3.3.2. 17) Restated wording of ice classifications to reflect that classifications are performed for New/Young and All other ice. 18) Delete section 3.3.5.3 Discrimination Between First Year Ice and Multi-year ice. 19) Deleted references to Multi-year classification processing	1) p ix 2) p 2 3) p 6 4) p 14 5) p15 6) p 16 7) p 17-18 8) p 20 9) p21-22 10) p 23 11) p 24 12) p24-25 13) p26 14) p27 15) p29 16) p35 17) p40 18) p50 19) p69;79-80
F	2 December 2009	Rev-F modifications made under ECR A-263, SPCRs 1471, 1494 for 1) Corrected error in text font color throughout the document. 2) Corrected table numbers and section numbers throughout the document 3) Added description of ice tie point adjustment to section 3.3.3 (SPCR 1494) Also corrected an existing error in the ATBD related to the band weighted average ice fraction computation.(SPCR 1471(	all all p. 35-40

TABLE OF CONTENTS

LIST OF FIGURES

Page

LIST OF TABLES

Page

GLOSSARY OF ACRONYMS

AM0	Air Mass Zero
AMSR	Advanced Microwave Scanning Radiometer
AOT	Aerosol Optical Thickness
ATBD	Algorithm Theoretical Basis Document
AVHRR	Advanced Very High Resolution Radiometer
AVIRIS	Airborne Visible/Infrared Imaging Spectrometer
BRDF	Bidirectional Reflectance Distribution Function
BRF	Bidirectional Reflectance Factor
CDR	Critical Design Review
cm	centimeter
CMIS	Conical Scanning Microwave Imager/Sounder
COT	Cloud Optical Thickness
CrIMMS	Cross-track Infrared Sounder / Advanced Technology Microwave Sounder
DISORT	Discrete Ordinates Radiative Transfer
DoD	Department of Defense
DV	Daytime Visible
EDR	Environmental Data Record
EOS	Earth Observing System (and Edge of Scan)
ERS	European Remote Sensing Satellite
FIRE-ACE	First ISCCP Regional Experiment–Arctic Cloud Experiment
GC-NET	Greenland Climate Network
GCM	General Circulation Model
GIFOV	Ground Instantaneous Field of View
GLERL	Great Lakes Environmental Research Laboratory
GLI	Global Imager
GSD	Ground Sample Distance
HCS	Horizontal Cell Size
HDRF	Hemispherical-Directional Reflectance Factor
HRI	Horizontal Reporting Interval
HSI	Horizontal Sampling Interval
HSR	Horizontal Spatial Resolution
IABP	International Arctic Buoy Program
IDPS	Interface Data Processing Segment
IORD	Integrated Operational Requirements Document
IP	Intermediate Product
IPT	Integrated Product Team

IPW	Image Processing Workbench
IR	Infrared
ISCCP	International Satellite Cloud Climatology Project
km	kilometer
LLLS	Low Level Light Sensor
LUT	Look Up Table
LWIR	Long Wave Infrared
m	meter
MAS	MODIS Airborne Simulator
MCC	Maximum Cross Correlation
MODIS	Moderate Resolution Imaging Spectroradiometer
MTF	Modulation Transfer Function
NASA	National Aeronautics and Space Administration
NCEP	National Centers for Environmental Prediction
NEdT	Noise Equivalent Delta Temperature
NGST	Northrop Grumman Space Technology
NIR	Near Infrared
NOAA	National Oceanic and Atmospheric Administration
NPOESS	National Polar-Orbiting Operational Environmental Satellite System
NPP	NPOESS Preparatory Project
NSCAT	NASA Scatterometer
OLS	Operational Linescan System
OOT	Ozone Optical Thickness
P^3I	Pre-Planned Product Improvement
PDR	Preliminary Design Review
PW	Precipitable Water
RDR	Raw Data Record
RMS	Root Mean Square
RTM	Radiative Transfer Model
SAR	Synthetic Aperture Radar
SBRS	Santa Barbara Remote Sensing
SDR	Sensor Data Record
SDSM	Solar Diffuser Stability Monitor
SeaWIFS	Sea-viewing Wide Field-of-view Sensor
SNR	Signal to Noise Ratio
SRD	Sensor Requirements Document
SRF	Spectral Response Function

SSM/I	Special Sensor Microwave/Imager
SSPR	Shared System Performance Responsibility
SWE	Snow Water Equivalent
SWIR	Short Wave Infrared
SZA	Solar Zenith Angle
TBD	To Be Determined
TBR	To Be Reviewed
THEMIS	Thermal Emission Imaging System
TIROS	Television Infrared Observing System
TOA	Top of Atmosphere
UV	Ultraviolet
VHRR	Very High Resolution Radiometer
VIIRS	Visible/Infrared Imager/Radiometer Suite
Vis-IR	Visible-Infrared
VOAT	VIIRS Operational Algorithm Team
WINCE	Winter Cloud Experiment
WVOT	Water Vapor Optical Thickness

ABSTRACT

The following document is revision E of the Algorithm Theoretical Basis Document (ATBD) for retrieval of the Sea Ice Characterization Environmental Data Record (EDR) from Top-of-Atmosphere (TOA) reflectances and Brightness Temperatures received by the National Polar-orbiting Operational Environmental Satellite System (NPOESS) Visible/Infrared Imager/Radiometer Suite (VIIRS). Sea Ice Characterization, a VIIRS level 2 product, is one of the required VIIRS EDR products, as stated in the NPOESS System Specification [SY15-0007]. The purpose of this document is to describe the theoretical basis and development process of the algorithms to retrieve ice concentration and ice age, to satisfy the EDR requirements in the NPOESS System Specification.

We retrieve ice concentration from an automated algorithm. The algorithm includes the derivation of ice fraction for imagery resolution pixels, using tie point analysis of ice surface temperature and/or surface reflectance. Operational capability is achieved by the use of local search windows to derive ice and water tie points and by automated cloud masking. Optimized parameters of a search window and band weight reduce tie point errors and provide a seamless day/night transition. Ice concentration is retrieved as a swath product at imagery resolution with measurement uncertainty better than 0.1 in most cases.

The algorithm for ice concentration produces the Ice Concentration Retained IP, Ice Reflectance Retained IP and Ice Temperature Retained IP files. These Retained IPs are not explicitly required by the NPOESS System Specification, but would be useful to analysts at operational ice centers and for Calibration/Validation purposes.

The NPOESS System Specification requires that the Sea Ice is classified as Ice-free, New/Young or All other types at a horizontal cell size of 2.4 km under clear conditions with a probability of correct typing of 70%. Objective requirements are to perform classification at a 90% probability of correct typing.

Our algorithm classifies ice type by using two methods. Nighttime discrimination of New/Young ice from All other thicker ice is achieved by an energy balance derivation of ice thickness from ice temperature. Daytime discrimination of New/Young ice from All other thicker ice is achieved by application of a reflectance threshold. The document covers all Sea Ice Characterization EDR processing. In particular, it describes algorithms for Ice Concentration and Sea Ice Age.

1.0 INTRODUCTION

1.1 PURPOSE

This Algorithm Theoretical Basis Document (ATBD) explains the mathematical background to derive the Sea Ice Characterization Environmental Data Record (EDR). In addition, this document provides an overview of the required input data, the physical theory, assumptions and limitations, and a sensitivity study of the described algorithm. The one EDR described in this document is part of the NPOESS/VIIRS team software package of EDRs.

Sea Ice Characterization EDR algorithm consists of four components:

(1) Determination of data quality and associated weights

(2) Determination of ice concentration

(3) Determination of Ice Age

1.2 SCOPE

This document covers the theoretical basis for the derivation of the Sea Ice Characterization EDR. The purpose and scope of this document are described in Section 1 while Section 2 gives an overview of the retrieval objectives. Section 3 describes the algorithm, its input data, the theoretical background, the EDR performance analysis, error budget, and plans for initialization and validation. Section 4 lists assumptions and limitations. Section 5 contains a list of referenced publications.

1.3 VIIRS DOCUMENTS

This document contains references to other Northrop Grumman and Raytheon VIIRS documents, designated by a document number, which is given in italicized brackets. The VIIRS documents cited in this document are:

[D42821] - Operational Algorithm Description Document for VIIRS Sea Ice Quality Intermediate Product (IP) and Surface Temperature IP (Rev B)

[D42820] - Operational Algorithm Description Document for VIIRS Sea Ice Concentration Intermediate Product (Rev B)

[D39593] - Operational Algorithm Description Document for VIIRS Sea Ice Age Environmental Data Record (Rev A)

[D36385] - EDR Interdependency Report (Rev D)

[SY15-0007] - NPOESS System Specification (Rev N)

[PS 154640-101] - VIIRS Sensor Specification

[Y2388 (D43313)] - VIIRS Aerosol Properties ATBD

[D43761 (Y2405)] - VIIRS Ice Surface Temperature ATBD

[D43777 (Y3261)] - VIIRS Radiometric Calibration ATBD

[D43766 (Y2412)] - VIIRS Cloud Mask ATBD

[D43767 (Y2466)] - VIIRS Imagery ATBD

[D43776 (Y3258)] - VIIRS Geolocation ATBD

[D43778 (Y7051)] - VIIRS Gridding ATBD

[Y2468] - VIIRS Operations Concept document

[Y2469] - VIIRS Context Level Software Architecture

[Y2470] - VIIRS Interface Control Document

[Y2471] - VIIRS Aerosol Module Level Software Architecture

[Y2472] - VIIRS Cloud Module Level Software Architecture

[Y2477] - VIIRS Snow Ice Module Level Software Architecture

[Y2478] - VIIRS Build-RDR Module Level Software Architecture Document

[Y2479] - VIIRS Build SDR Module Level Software Architecture

[Y3231] - VIIRS Sea Ice Age Unit Level Detailed Design Document

[Y3235] - VIIRS Ice Concentration Unit Level Detailed Design Document

[Y3236] - VIIRS Software Integration and Test Plan

[Y3237] - VIIRS Algorithm Verification and Validation Plan

[Y3270] - VIIRS System Verification and Validation Plan

[Y3277] - VIIRS Aerosol Module Level Interface Control Document

[Y3278] - VIIRS Cloud Module Level Interface Control Document

[Y4963] - VIIRS Imagery Technical Interchange Meeting

[Y0010880] – VIIRS Surface Temperature IP Unit Level Detailed Design Document

[Y0011649] – VIIRS Ice Quality Unit Level Detailed Design Document

1.4 REVISIONS

Revision F of the Sea Ice Characterization ATBD dated December 2, 2009 implements changes for an optional ice tie point adjustment scheme for the Sea Ice Concentration IP algorithm for cases in which no open water is found in a local search window.

Revision E of the VIIRS Sea Ice Characterization ATBD dated April 10, 2008 implements changes for removal of the Multi-year ice classification requirement. Multi-year sea ice age classification is no longer required by the NPOESS System Specification and the Multi-year retrieval algorithm logic has been removed.

Revision D of the VIIRS Sea Ice Characterization ATBD dated August 8, 2007 corrects reference to the section describing the Analytical Snow Depth/Ice Thickness LUT as section 3.3.5.1.1 Documents numbers corresponding to NGST "D" numbers have been added for the ATBD documents. The VIIRS band and wavelengths for the thermal bands have been corrected in the tables on page 14

Revision A of the VIIRS Sea Ice Characterization ATBD, dated October 18, 2006 eliminates references to the Aerosol Model Index IP as an input, the Ice Edge Location Application and Ice Concentration Applied Research Products. Also eliminated are tunable parameter tables more appropriately described in the Sea Ice Characterization Operational Algorithm Documents for the VIIRS Sea Ice Quality and Surface Temperature IP, VIIRS Sea Ice Concentration IP, and the VIIRS Sea Ice Age EDR. The corrupted format of equation 3.3.51.2 has been corrected in this version and references to imagery resolution ancillary input files have been changed to moderate resolution consistent with the EDR Interdependency Report (EDRIR) document (D36385.)

The fourth revision of version 5 of the VIIRS Sea Ice Characterization ATBD, dated March 2005 contains a minor revision, consisting of brief clarification of the ice tie point determination and the addition of a description of the process to classify Ice Age types by the use of a Previous Ice Age IP. It should be noted that the Fresh Water Ice Edge Location Application has been eliminated from algorithm The Ice Concentration ARP also has been eliminated from this algorithm. . The second revision, dated December 2004, was a major revision, reflecting algorithm development performed under the VIIRS Algorithm Continuance contract. Note that the document title has been changed. Previous versions of this ATBD were titled “VIIRS Sea Ice Age/Edge Motion ATBD”. The first revision of version 5, dated April 2002, was a minor revision of version 5.0, which was released in March 2002 as part of the Raytheon NPOESS/VIIRS Critical Design Review (CDR) package. The first two versions were developed in response to VIIRS Sensor Requirements Document (SRD), revision 1, dated August 3, 1998. The first version was dated October 1998. The second version was dated June 1999. The third version, dated May 2000, was developed in response to VIIRS Sensor Requirements Document (SRD), Version 2, Revision a, dated 04 November 1999 and was submitted as part of the Raytheon NPOESS/VIIRS Preliminary Design Review (PDR) and Proposal packages.

Changes for version 3 were largely in response to revisions in the SRD. They included:

- Modification of the process flow
- Additional fresh water ice test results, from an expanded test data set
- A revised fresh water ice specification, with supporting error analysis and error budget

The primary purpose of version 4, dated May 2001, was to respond to VIIRS Algorithm Watch List items generated by the VIIRS Operational Algorithm Team (VOAT). An additional purpose is to incorporate minor revisions generated by an internal Raytheon review since the VIIRS PDR. Changes since version 3 included:

- Inclusion of directional correction factors
- Expanded description of input data, including VIIRS gridded data
- Revision and enhancement of the process flow description

Version 5 incorporated the post-PDR developments in software architecture and detailed design that bring the algorithm to a CDR level of maturity. Changes since version 4 included:

- Additional development of the algorithm, with a detailed process flow and a detailed description of the Look Up Tables (LUTs).
- The introduction of an Ice Quality process which performs pixel masking and pixel weighting
- The introduction of a fixed external polar grid for the image pairs input to the MCC.
- The use of motion vectors from a sequence of image pairs for Ice Edge Motion

Version 5, revision 2 was developed in the NPOESS EMD phase as part of the VIIRS Algorithm Continuance work, under the direction of the NPOESS Shared System Performance Responsibility (SSPR) contractor, Northrop Grumman Space Technology (NGST). Changes include:

- The elimination of the Ice Edge Motion unit. This unit has been eliminated because the ice edge motion product was deleted from the EDR requirements.
- Simplification of the Ice Edge Location unit. The use of an autocorrelation function to select a window size has been dropped, because analysis has failed to demonstrate that it will perform adequately. This aspect of the algorithm was intended for diffuse ice edges, and was never needed to meet requirements.
- The development and expansion of modeled reflectance in the Ice Reflectance LUT. In the previous version, the LUT contained surface reflectance models derived from MODTRAN 4.0. In the revised version, the LUT contains directional TOA reflectance (TOA BRDF) derived from the Discrete Ordinates Radiative Transfer (DISORT) and 6S radiative transfer models (RTMs).
- The use of observed TOA reflectance instead of derived surface reflectance as input data. Observed reflectance is compared to modeled TOA BRDF to derive reflectance-based ice age.

- The development of the Snow Depth/Ice Thickness LUT. In the previous version, the LUT included ice growth times from observed surface air temperature and recent snowfall history. Ice growth times were used to estimate snow depth. The new LUT contains snow depth modeled directly from climatology. The reliance on recent surface air temperature and snowfall history has been eliminated. Snow depth is used in the derivation of ice age.
- The addition of a LUT containing broad-band atmospheric transmittance. The LUT is derived from the 6S RTM. Transmittance is used to compute the shortwave flux in the surface temperature based derivation of ice age.

2.0 EXPERIMENT OVERVIEW

2.1 OBJECTIVES OF THE RETRIEVAL

2.1.1 Sea Ice Characterization

The content of the Sea Ice Characterization EDR includes ice concentration and ice age. Ice concentration is defined as the fraction of a given area of sea water covered by ice. Sea ice age is defined as the time that has passed since the formation of the surface layer of an ice covered region of the ocean. The objective of the VIIRS sea ice retrieval is to achieve the performance specifications designed to meet the requirements stated in the NPOESS System Specification. These are listed in Table 1.

Table 1. Specification of the NPOESS Sea Ice Characterization EDR

Units:
Ice Age: WMO Nomenclature Class
Ice edge Concentration: Tenths

Paragraph	Subject	Specified Value
	a. Horizontal Cell Size (Ice Age)	
40.7.8-1a	1. Clear	2.4 km
40.7.8-2	b. Horizontal Reporting Interval	HCS
40.7.8-3	c. Horizontal Coverage	Oceans
	d. Measurement Range	
40.7.8-4a	1. Ice Age Classes, Clear	Ice-free, New/Young ice, All other ice
	e. Probability of Correct Typing (Ice Age)	
40.7.8-6a	1. Ice-free	70%
40.7.8-6b	2. New/Young	70%
40.7.8-6c	3. All other ice	70%
40.7.8-8	g. Mapping Uncertainty, 3 Sigma	1.5 km
40.7.8-9	h. Max Local Average Revisit Time	24 hrs
40.7.8-12	j. Latency	NPP - 150 min. NPOESS 8 hr
	m. Degraded Clear Measurement Condition for Probability of Correct Typing: [VIIRS Degradation]	
40.7.8-15a	1. Thermal Contrast 1.5 K (TBR) to 2.2 K Between Ice and Open Water	60% (TBR)
40.7.8-15b	2. Snow Fall 6 cm to 10 cm	60% (TBR)
	n. Excluded Clear Measurement Condition for Probability of Correct Typing:	
40.7.8-16a	1. Thermal Contrast < 1.5 K (TBR) Between Ice and Open Water	
40.7.8-16a	2. Snow Fall 10 cm (TBR)	
40.7.8-16b	3.Aerosol Optical Thickness > 1.0	
40.7.8-16c	4 Sun Glint	

The ice concentration requirement is restricted to CMIS (passive microwave). Because the VIIRS algorithm for ice age requires a derivation of sea ice concentration, the

algorithm is able to write this information in an Ice Concentration Retained IP that can be used in conjunction with the Sea Ice Characterization EDR.

The polar oceans comprise approximately 6.5% of the Earth's surface and are covered by sea ice at some time during the course of the annual cycle. At its maximum extent, sea ice blankets ~19 x 10^6 km^2 of the Southern Hemisphere and ~14 x 10^6 km^2 of the Northern Hemisphere. In the Arctic, nearly half of the late-winter maximum of sea ice cover survives the summer melt season and is classified as Multi-year ice. The net export of Multi-year sea ice through the Fram Strait is balanced by production of Multi-year ice in the Arctic basin. In the Antarctic, more than 90% of the sea ice found at the time of maximum extent in the late austral winter is formed, grows, and completely melts during the annual cycle and as such is classified as First Year ice.

Long-term trends in the extent of the polar sea ice pack can be a valuable indicator of global climate change. This is particularly true for polar regions, which are believed to be sensitive to global warming, but are too remote for comprehensive *in situ* monitoring.

Sea ice age is defined as the time that has passed since the formation of the surface layer of an ice covered region of the ocean. The content of the Sea Ice Characterization EDR includes the typing of areas of sea ice by age. The definition of ice age is intended to apply to the actual age of the ice that happens to be at a particular location. It is not intended to mean the time interval that has passed since ice first formed at that spot. The definition of ice age implies a Lagrangian description of ice type redistribution.

The heat budget of the polar regions is significantly affected by the presence of sea ice and by its annual cycle of growth and decay. Sea ice significantly inhibits the vertical flux of latent and sensible heat from the ocean to the atmosphere and reflects a large fraction of the incident solar radiation. The insulating properties of sea ice are strongly dependent on its thickness, which is directly linked to its age (Yu and Rothrock, 1996). Information on the extent of various ice age types is necessary for accurate general circulation models (GCMs) in the polar regions. GCMs do not simulate the Arctic climate very well (Bromwich and Tzeng, 1994), indicating the need to improve measurements of the global cover of sea ice of various age types. Information about ice age is also important for commercial and military operations in polar seas.

In practice, ice types are characterized by stage of development. Stage of development, ice age, and ice thickness represent different sides of the same thermodynamic process—ice growth—but their meaning is different. Variability in ice thickness, to a great degree, depends upon location, climatic conditions, and season. Changes in these conditions will lead to a different rate of ice growth and quite different ice thickness achieved for the same period of time after ice formation. Our interpretation of the Integrated Operational Requirements Document (IORD) is that stage of development of ice cover is of greater interest for Arctic and Antarctic operations and research than is the actual time that has passed since the formation of ice. Stage of development is included in the international system of sea-ice symbols and routinely

used in ice charts. It is a standard and most commonly used parameter describing the formation and growth of ice cover.

Our algorithm will provide information on stage of development for a horizontal cell, to meet requirements.

2.2 ALGORITHM HERITAGE

2.2.1 Sea Ice

2.2.1.1 Passive Microwave

The classification of sea ice concentration and sea ice age from passive microwave brightness temperatures is well-established (Eppler *et al.*, 1992), and currently forms the basis for global sea ice retrieval at various ice centers (Boardman *et al.*, 1995; Partington and Steffen, 1998).

A uniform slab of clear ice will emit microwave radiation proportional to its thickness. However, there can be many air bubbles and brine pockets that are unevenly distributed throughout the ice. The bubbles lower the emissivity, resulting in brightness temperature variations (Hall *et al*, 1981). Surface features, produced by freeze/thaw events and motion-driven collisions, will also modify the microwave signal (Eppler *et al*, 1992). The same features affect surface albedo, suggesting that there should be correlations between microwave and reflectance signatures of sea ice.

2.2.1.2 Synthetic Aperture Radar

Synthetic aperture radar (SAR) observations of sea ice have shown that radar backscatter signatures are characteristic of ice type, and can be used for classifying sea ice cover by imagery analysis (Jeffries, *et al*., 1994; Hall, *et al*., 1994). RADARSAT observations are being incorporated into the ice typing retrievals at ice centers. SAR-based retrievals have the advantage of good spatial resolution and allow coverage under cloudy conditions. Disadvantages are the limited aerial coverage and the lack of reliable automated classification algorithms. An additional disadvantage from an operational standpoint is the lack of contemporaneous data, since RADARSAT is on a separate platform. RADARSAT data would be useful for validation purposes.

2.2.1.3 Visible-Infrared

Until recently, retrieval of sea ice concentration from visible-infrared data has been hampered by the inability to effectively discriminate the visible-infrared signals from snow/ice surfaces and clouds. The launch of the Moderate Resolution Imaging Spectroradiometer (MODIS) aboard the EOS Terra and Aqua platforms has allowed for global retrievals of ice cover (**http://modis-snow-ice.gsfc.nasa.gov/sea.html**), because the short wave infrared (SWIR) bands on MODIS do discriminate between the

signals from clouds and snow/ice. MODIS provides a global ice cover product, using a binary ice/water classification algorithm (Hall et al., 1998, 2001a).

The MODIS algorithm does not provide a sub-pixel resolution ice concentration. Sub-pixel resolution ice concentration has been retrieved from National Oceanic and Atmospheric Administration (NOAA) Advanced Very High Resolution Radiometer (AVHRR) data, by the use of ice and water reflectance tie points (Massom and Comiso, 1994). The AVHRR retrievals have been limited to local areas, because there has been no reliable method to obtain global tie points. One well-established characteristic of sea ice is the wide range in reflectance observed in first-year ice of various types and thickness (Grenfell and Maykutt, 1977; Grenfell and Perovich, 1984). This characteristic is an important limiting factor in reflectance-based retrieval of ice concentration in the absence of snow cover (Massom and Comiso, 1994). Our search window technique (Section 3.3.5.2.1) handles this problem by characterizing the local ice reflectance empirically.

The classification of sea ice age from visible-infrared data alone is difficult. Thick First Year ice is similar to Multi-year ice in its reflectance properties. Also, most sea ice surfaces will be snow covered. As a result, the use of measured albedo to classify ice age types on a global basis has not been established, though some regionally based classifications have been made, using the AVHRR channel 2 (Massom and Comiso, 1994). Older ice tends to be colder in the winter, allowing for age typing derived from surface temperature, as derived from AVHRR channel 4 (Massom and Comiso, 1994). An alternative approach shows promise. Yu and Rothrock (1996) and Lindsay and Rothrock (1993) have incorporated albedo and temperature data from AVHRR into an energy balance model to derive the thickness of the ice, with a reported accuracy of 50%.

Regional and seasonal ice conditions can be used in energy balance models along with observed temperature to infer age type. The incorporation of air temperature and snow depth as ancillary data will improve the accuracy of a classification of ice type using an energy balance model. The energy balance method has been incorporated into our ice age algorithm, as discussed in Section 3.3.2.2.

2.2.1.4 MODIS Airborne Simulator

MODIS pre-launch activity uses data from the various campaigns of the MODIS Airborne Simulator (MAS). We will also make use of this data for initialization and pre-launch characterization, as we discuss in Section 3.5.6 of this document. MAS data have also been used for our EDR performance analysis (c.f. Section 4.1).

2.2.1.5 Passive Microwave

Passive microwave observations of first year sea ice have made a valuable contribution to the study of polar regions (Eppler *et al.,* 1992).

2.3 INSTRUMENT CHARACTERISTICS

The VIIRS instrument can be pictured as a convergence of three existing sensors.

The Operational Linescan System (OLS) is the operational visible/infrared scanner for the Department of Defense (DoD). Its unique strengths are controlled growth in spatial resolution through rotation of the ground instantaneous field of view (GIFOV) and the existence of a low-level light sensor (LLLS) capable of detecting visible radiation at night. OLS has primarily served as a data source for manual analysis of imagery. The Advanced Very High Resolution Radiometer (AVHRR) is the operational visible/infrared sensor flown on the National Oceanic and Atmospheric Administration (NOAA) Television Infrared Observation Satellite (TIROS-N) series of satellites (Planet, 1988). Its unique strengths are low operational and production cost and the presence of five spectral channels that can be used in a wide number of combinations to produce operational and research products. In December 1999, the National Aeronautics and Space Administration (NASA) launched the Earth Observing System (EOS) morning satellite, *Terra*, which includes the Moderate Resolution Imaging Spectroradiometer (MODIS). This sensor possesses an unprecedented array of thirty-two spectral bands at resolutions ranging from 250 m to 1 km at nadir, allowing for unparalleled accuracy in a wide range of satellite-based environmental measurements. A second MODIS sensor was included on the EOS afternoon satellite *Aqua*, launched May 4, 2002.

VIIRS will reside on a platform of the National Polar-orbiting Operational Environmental Satellite System (NPOESS) series of satellites. It is intended to be the product of a convergence between DoD, NOAA and NASA in the form of a single visible/infrared sensor capable of satisfying the needs of all three communities, as well as the research community beyond. As such, VIIRS will require three key attributes: high spatial resolution with controlled growth off nadir, minimal production and operational cost, and a large number of spectral bands to satisfy the requirements for generating accurate operational and scientific products.

The VIIRS sensor specification is based on the sensor requirements of the National Polar-orbiting Operational Environmental Satellite System (NPOESS) and on EDR thresholds and objectives. The Sea Ice Characterization algorithms take as input geolocated, calibrated Sensor Data Records (SDRs) generated from VIIRS I1 (640 nm) and I2 (865 nm) Imagery bands and three VIIRS moderate resolution bands I5 (11450 nm), M15 (10763 nm) and M16 (12013 nm) *[D43777]*. The SDRs are obtained from VIIRS RDRs by an RDR to SDR process. The RDRs are obtained by a rotating telescope scanning mechanism that minimizes the effects of solar impingement and scattered light. Figure 1 illustrates the design concept for VIIRS, designed and built by Raytheon Santa Barbara Remote Sensing (SBRS). VIIRS is essentially a combination of SeaWiFS foreoptics and an all-reflective modification of MODIS/THEMIS aft-optics. Calibration is performed onboard using a solar diffuser for short wavelengths and a blackbody source and deep space view for thermal wavelengths. A solar diffuser stability monitor (SDSM) is also included to track the performance of the solar diffuser. The VIIRS scan will extend to 56 degrees on either side of nadir, providing a swath of 3000 km for the nominal satellite altitude of 833 km.

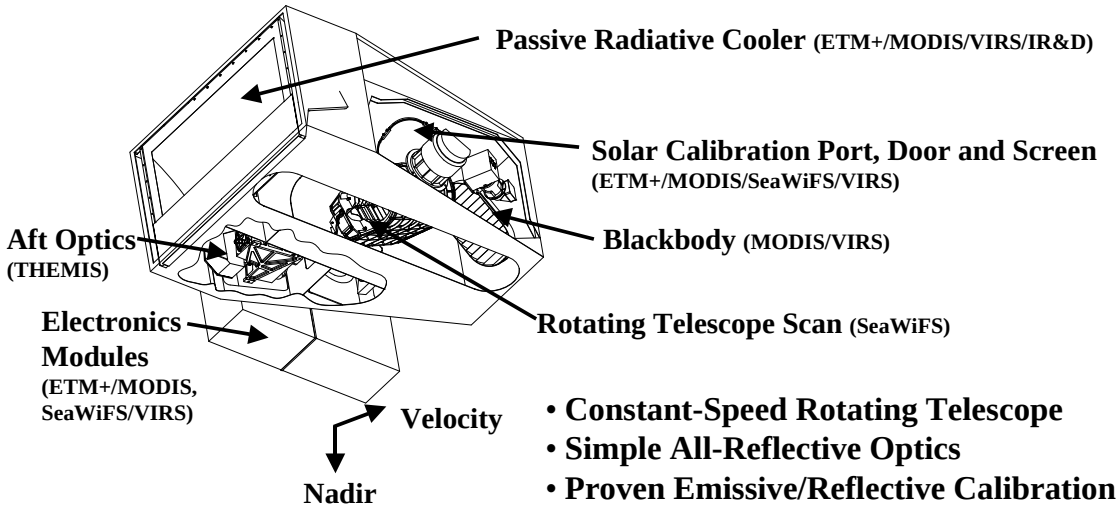

Figure 1. Summary of VIIRS design concepts and heritage.

The VIIRS Sensor Requirements Document (SRD) placed explicit requirements on spatial resolution for the VIIRS sensor. Specifically, the horizontal spatial resolution (HSR) of bands used to meet threshold Imagery EDR requirements must be no greater than 400 m at nadir and 800 m at the edge of the scan. This led to the development of a unique scanning approach which optimizes both spatial resolution and signal to noise ratio (SNR) across the scan. The concept is summarized in Figure 2 for the imagery (fine resolution) bands. The VIIRS detectors are rectangular, with the smaller dimension along the scan. At nadir, three detector footprints are aggregated to form a single VIIRS "pixel." Moving along the scan away from nadir, the detector footprints become larger both along track and along scan, due to geometric effects and the curvature of the Earth. The effects are much larger along scan. At 31.59 degrees in scan angle, the aggregation scheme is changed from 3x1 to 2x1. A similar switch from 2x1 to 1x1 aggregation occurs at 44.68 degrees. The VIIRS scan consequently exhibits a pixel growth factor of only 2 both along track and along scan, compared with a growth factor of 6 along scan which would be realized without the use of the aggregation scheme. This scanning approach allows VIIRS to provide imagery at 800-m resolution or finer globally, with 375-m resolution at nadir. Additionally, due to the imagery requirements for VIIRS and the "sliver" detector design, MTF performance will be extremely sharp (0.5 at Nyquist).

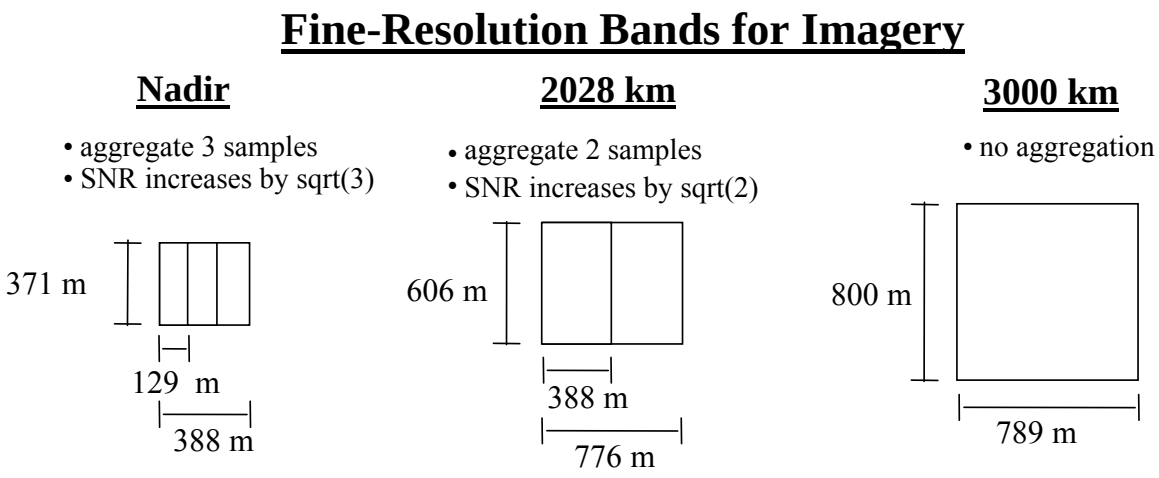

Figure 2. VIIRS detector footprint aggregation scheme for Imagery “pixels”.

Figure 3, showing the Horizontal Sampling Interval (HSI) that results from the combination scan/aggregation scheme, illustrates the benefits of the aggregation scheme for spatial resolution.

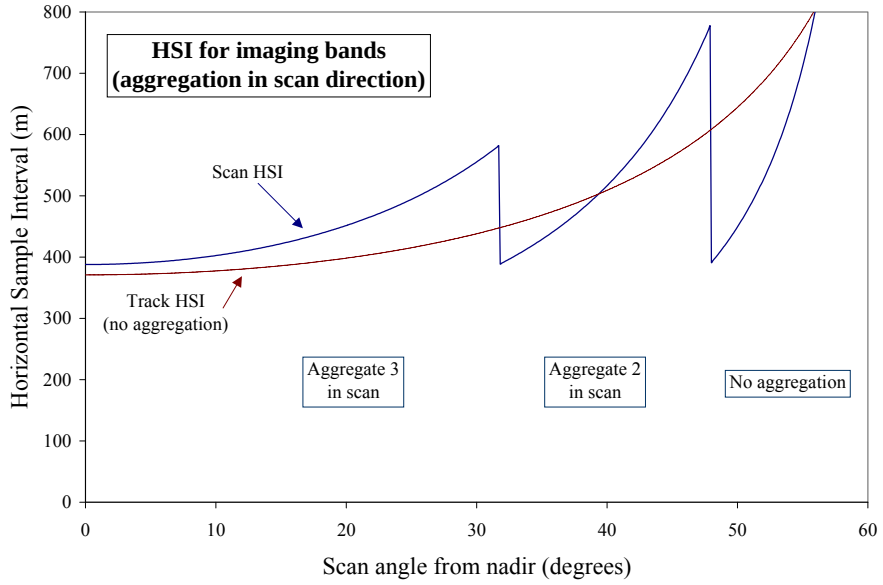

Figure 3. Horizontal Sampling Interval (HSI) for imagery bands

The aggregation switch points occur at scan angles of 31.59 degrees (3 to 2 aggregation) and 44.68 degrees (2 to no aggregation).

The performance characteristics of the bands used by the Sea Ice Characterization algorithm, listed in Table 2, are obtained from the VIIRS Sensor Specification Document *[PS 154640-101]* and the VIIRS Radiometric Calibration ATBD *[D43777].* The VIIRS sensor has been designed from the NPOESS sensor requirements and the flowdown of EDR requirements. Complete details on the instrument design are provided in the Raytheon VIIRS Sensor Specification Document *[PS154640-101]*.

The algorithm uses TOA reflectance in three bands at imagery resolution and surface temperature. The surface temperature is derived at imagery resolution from a three-band algorithm (two moderate resolution bands and one imagery resolution band).

Table 2 lists the characteristics of these bands.

Table 2. Sea Ice Characterization Algorithm – Input Data Summary (Spatial)

VIIRS Band	λ(μm)	Δλ(μm)	GSD[1] (m) at Nadir (Track x Scan)	HCS[2] (m) at Nadir (Track x Scan)	GSD (m) at Edge of Scan (Track x Scan)	HCS (m) at Edge of Scan (Track x Scan)
I1	0.640	0.080	371 x 131	371 x 393	800 x 800	800 x 800
I2	0.865	0.039	371 x 131	371 x 393	800 x 800	800 x 800
M15	10.76	1.0	742 x 262	742 x 742	1600 x 1600	1600 x 1600
I5	11.45	1.9	371 x 131	371 x 392	800 x 800	800 x 800
M16	12.01	0.95	742 x 262	742 x 742	1600 x 1600	1600 x 1600

[1] - Ground Sample Distance

[2] - Horizontal Cell Size

Additional details on the instrument design are provided in the Raytheon VIIRS Sensor Specification document *[PS 154640-101]*.

2.4 RETRIEVAL STRATEGY

2.4.1 Ice Concentration

The input data will consist of a two-dimensional grid of surface pixels in the form of geolocated TOA reflectance for bands I1 and I2 and geolocated surface temperature. TOA reflectance will be supplied by the VIIRS EV_375M SDR *[D43777]*. The surface temperature will be supplied by a Surface Temperature IP *[D43761].*

Each pixel will be examined for its suitability. A pixel weighting process is followed, using an Ice Quality LUT to assign pixel weights according to band, various atmospheric conditions, and various surface conditions (c.f. Section 3.3.2). The Cloud Mask algorithm *[D43766]* will identify pixels that should be excluded from processing due to cloud contamination and will also supply a land/water mask. Pixels designated as ocean by the land/water mask and as clear or probably clear by the cloud mask will be passed for processing. Pixels designated as “probably clear” or “thin cirrus” will be given a reduced pixel weight, and will have a quality flag attached to them. The solar/sensor angles, aerosol optical thickness, and cloud optical thickness for each pixel will be used to derive pixel quality and pixel weight for each band. These will determine whether the pixel is rejected, passed for further processing with a quality flag attached, or passed for further processing without reservation.

For each pixel that has been passed for further processing, ice and water tie points will be determined, using a moving local search window to identify local tie points. The fraction of ice cover in each pixel will be computed from a standard tie point equation, following the prescription described in Section 3.3.3.

The process flow to implement ice concentration retrieval is outlined in Section 3.1.

2.4.2 Ice Age

The VIIRS Ice Age algorithm classifies each ice-covered VIIRS pixel as Ice free, New/Young ice, or All other ice. A pixel is treated as ice-covered if its derived ice concentration is greater than a TBD threshold value, obtained from the Ice Age LUT.

Our algorithm classifies ice type by using two methods:

(1) Nighttime discrimination of New/Young ice from thicker First Year and Multi-year ice is achieved by an energy balance derivation of ice thickness from ice temperature.

(2) Daytime discrimination of New/Young ice from thicker First Year and Multi-year ice is achieved by application of a reflectance threshold.

Both methods use ice surface reflectance and ice surface temperature derived from VIIRS data. Different ice types exhibit different albedo and different surface temperature. This physical basis is used for discrimination between New/Young and All other ice types. The use of reflectance of visible and near-infrared bands or ice surface temperature is an effective way to retrieve ice type for relatively thin ice cover.

Older ice tends to be colder in the winter, allowing for age classification from surface temperature. Regional and seasonal ice conditions can be used in an energy balance model, along with observed surface temperature, to calculate ice thickness. The incorporation of air temperature (and snow depth) as ancillary data will improve the accuracy of calculations, using an energy balance model. Classification of ice types on the basis of surface reflectance is a straightforward process. We also recommend the development of regional LUTs to transform retrieved ice surface reflectance into ice age.

The input data will consist of 2-dimensional images of geolocated ice surface reflectance and geolocated ice surface temperature, produced by the ice concentration algorithm *[D43063]*. The input data will include pixel quality and pixel/band weights, obtained from the Ice Quality Flags IP and the Ice Weights IP. Pixel quality and pixel weights are determined from several factors, including solar/sensor angles, cloud conditions, and aerosol conditions. Each pixel with ice concentration greater than a specified threshold will be processed for ice type classification. New/Young or All other ice will be classified from reflectance during daytime or from temperature during nighttime.

3.0 ALGORITHM DESCRIPTION

3.1 PROCESSING OUTLINE

Input data, described in Section 3.2, is read in. Pixels within the pre-specified horizontal coverage range are passed into the ice units. The algorithm consists of three separate software units:

1) Ice Quality
2) Ice Concentration
3) Ice Age

These units are linked in a common software process, as shown in Figure 4.

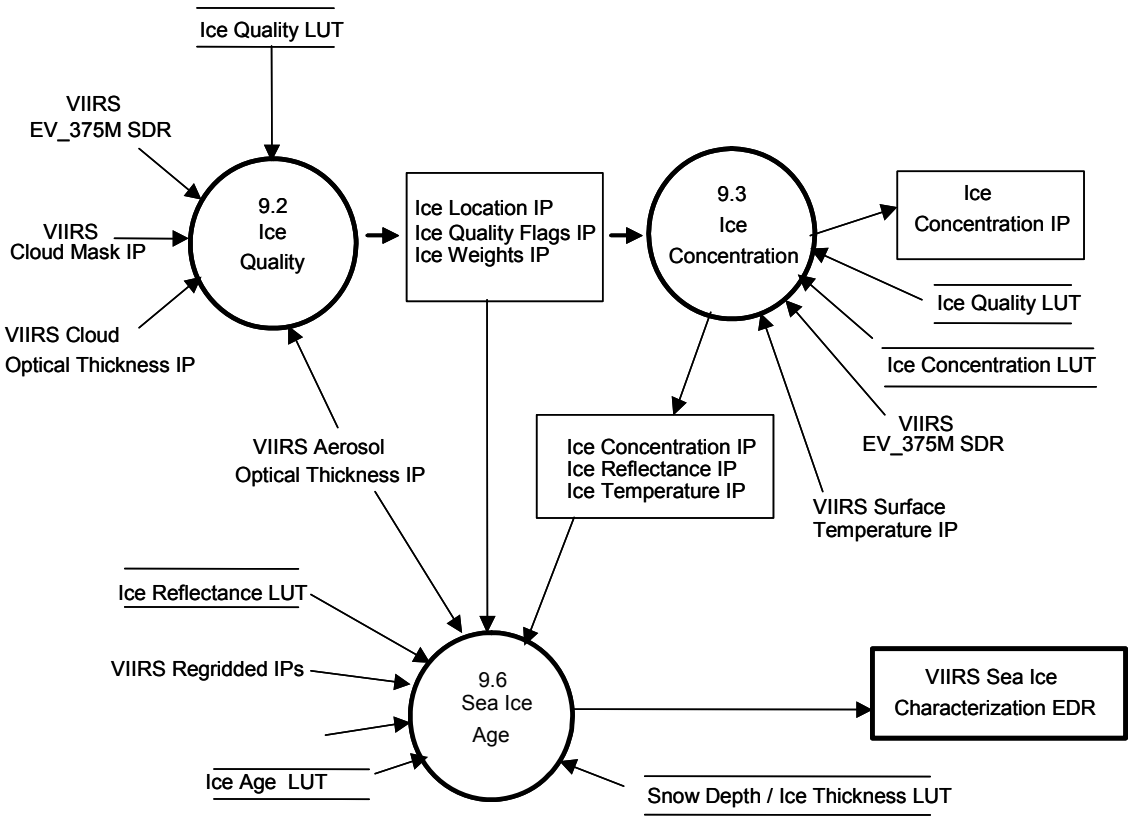

Figure 4. Process flow for the Sea Ice Characterization EDR algorithm

3.1.1 Ice Quality

The *Ice Quality* process (Section 3.3.2) performs pixel masking and pixel weighting. The process flow is shown in Figure 5.

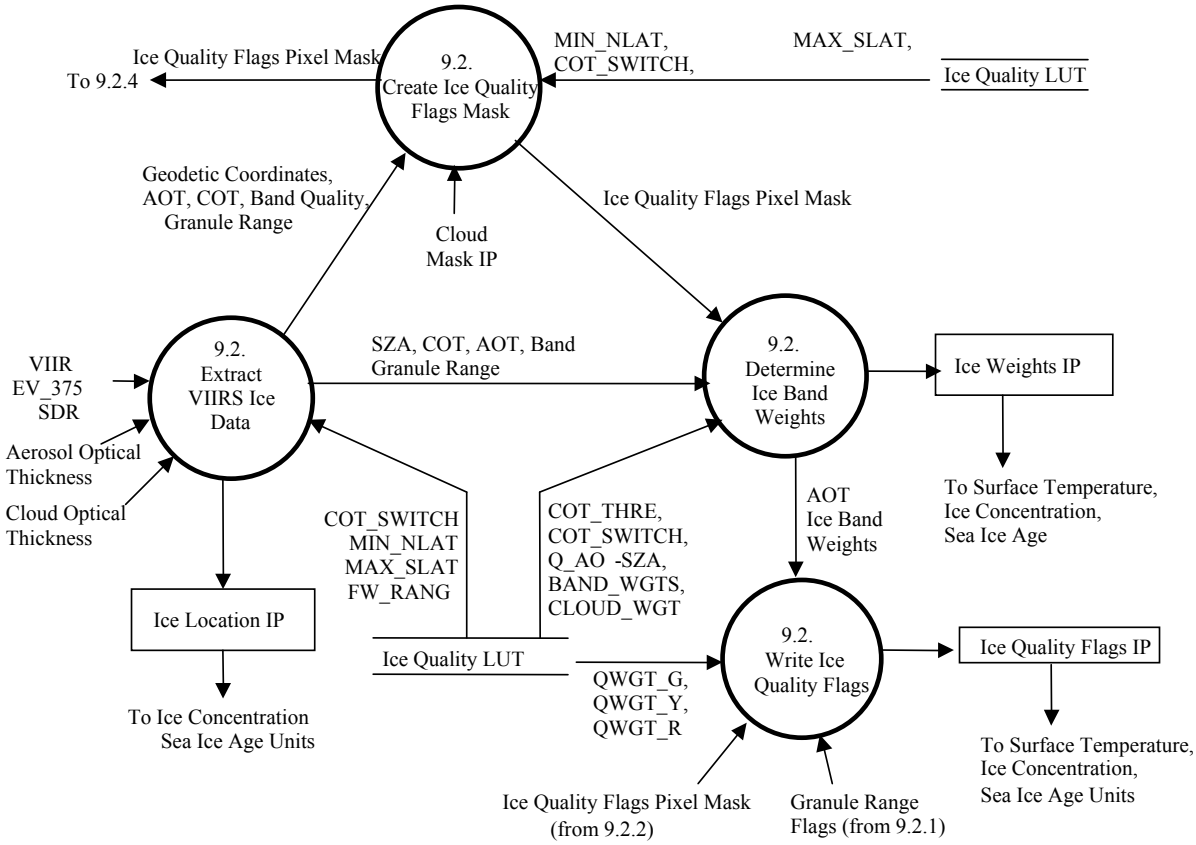

Figure 5. Process flow for the Ice Quality software unit.

The process uses information in the VIIRS EV_375M SDR *[D43777]*, VIIRS Aerosol Optical Thickness IP *[D43313]*, VIIRS Cloud Optical Thickness IP *[D43750]*, VIIRS Cloud Mask IP *[D43766]*, and an Ice Quality LUT. The process produces a pixel quality mask and pixel weights for each band. The process produces the Ice Location IP, the Ice Quality Flags IP, and the Ice Weights IP.

The process flow is described in detail in the VIIRS Snow/Ice Module Level Software Architecture document *[Y2477]* and the Ice Quality Unit Level detailed design document *[Y0011649]*.

3.1.2 Ice Concentration

The *Ice Concentration* process (Section 3.3.3) derives the fractional ice cover of a pixel. The process flow is shown in Figure 6. Note that the Ice Concentration ARP has been eliminated and will not be produced operationally .

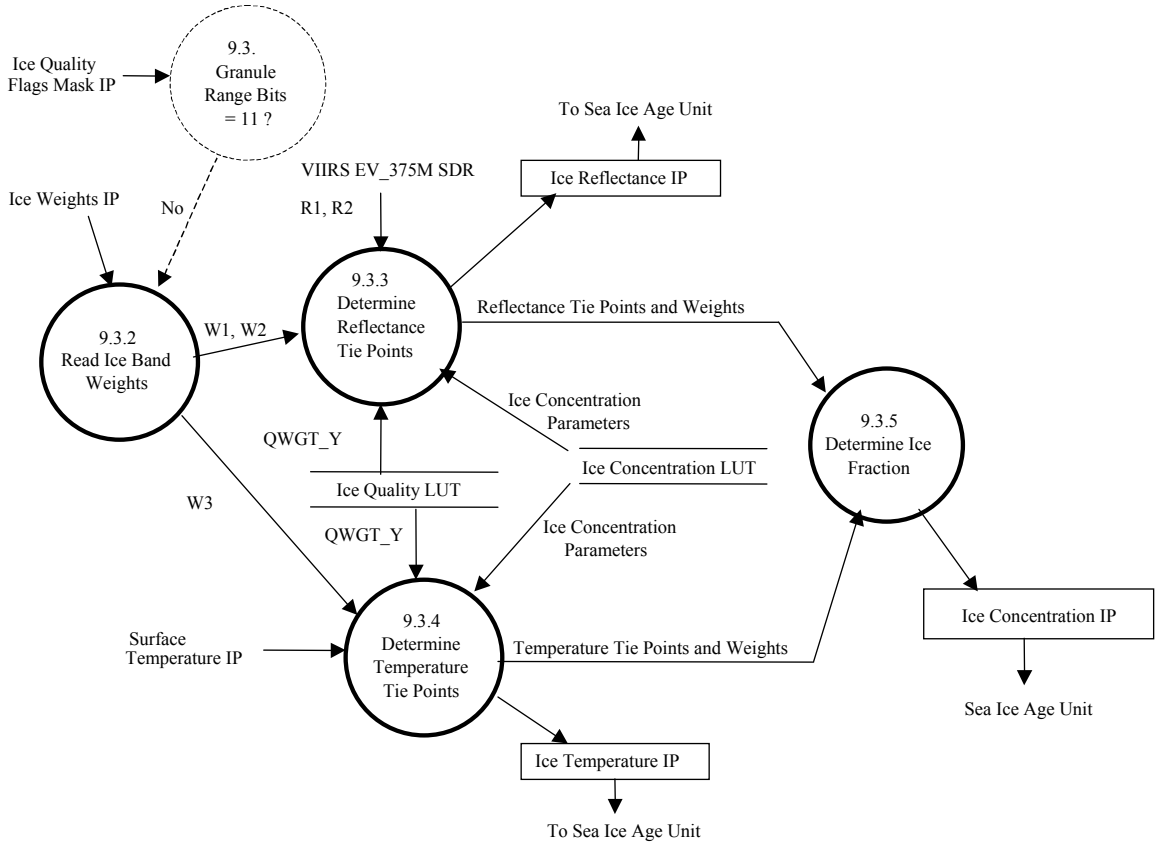

Figure 6. Process flow for the Ice Concentration software unit.

The process uses information in the VIIRS EV_375M SDR *[D43777]*, VIIRS Surface Temperature IP, the Ice Quality Flags, Ice Weights, and Ice Location IPs from the Ice Quality unit *[Y0011649]*, an Ice Concentration LUT, and an Ice Quality LUT.

Ice concentration, ice temperature and ice reflectance are derived for each pixel within the Horizontal Coverage region. Two Top-of-Atmosphere (TOA) reflectance images are passed into the Ice Concentration unit. The images, from VIIRS imagery resolution bands I1 (Visible) and I2 (Near Infrared (NIR)), are obtained from the VIIRS EV_375M SDR *[D43777]*. Bad pixels are identified from quality information in the Ice Quality Flags IP and Ice Weights IP. Ice concentration is calculated for each good pixel, using a tie point algorithm (c.f. Section 3.3.3). The ice tie points are derived for each good quality pixel and written to the Ice Reflectance IP.

The surface temperature image is passed into the Ice Concentration unit. The image is obtained from the VIIRS Surface Temperature IP, at imagery resolution. Bad pixels are identified from quality information in the Ice Quality Flags IP, Ice Weights IP, and Surface Temperature IP *[D43761]*. Ice concentration is calculated for each good pixel, using a tie point algorithm (c.f. Section 3.3.3). The ice tie points are derived for each good quality pixel and written to the Ice Temperature IP.

The combined ice concentration for each pixel is calculated as the weighted mean of the three individual results (I1 reflectance, I2 reflectance, surface temperature). Concentration weights for each pixel are calculated as the sum of the individual band weights. The band weights are obtained from the Ice Weights IP.

The process produces ice concentration and concentration weights for each imagery resolution pixel.

The process flow is described in detail in the VIIRS Snow/Ice Module Level Software Architecture document *[Y2477]* and the Ice Concentration Unit Level detailed design document *[Y3235]*.

3.1.3 Ice Age

The *Ice Age* process (Section 3.3.5) derives the fractional ice cover of a pixel. The process flow is shown in Figure 7.

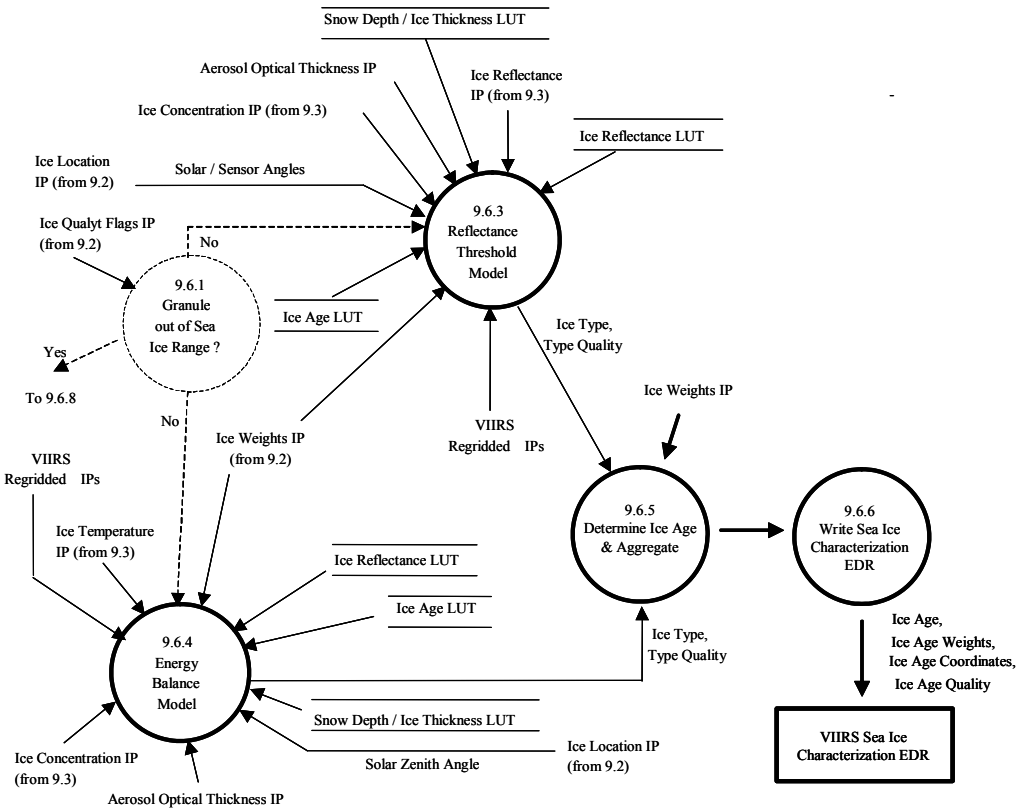

Figure 7. Process flow for the Ice Age software unit.

Each pixel with ice concentration greater than a specified threshold is processed to classify it as either New/Young (thickness less than 30 cm (TBR)) or All other ice types,

The VIIRS Sea Ice Age algorithm uses two methods:

The *Reflectance Threshold Model* process discriminates New/Young ice from thicker First Year and Multi-year ice by application of modeled TOA ice reflectance to derived I1 and I2 ice reflectance. An Ice Reflectance LUT is used to obtain model I1 and I2 band TOA ice reflectance. The following steps are implemented:

a. Snow depth on the ice cover is modeled as a function of ice thickness, using climatological snow depth data in the Snow Depth/Ice Thickness LUT.

b. Model TOA ice reflectance for each of the two imagery bands, appropriate for the pixel solar/viewing angles, atmospheric conditions, and snow depth, are acquired from the Ice Reflectance LUT.

c. For each of the two imagery bands, the model TOA ice reflectance is compared to the observed TOA ice reflectance to derive ice thickness.

d. The pixel is classified as New/Young ice if its derived ice thickness is less than a threshold value. Otherwise, it is classified as All other ice. The threshold value is obtained from the Ice Age LUT. If the classifications from the two bands agree, the pixel is assigned that classification. If the classifications from the two bands differ, the pixel is assigned the classification from the band with the greater weight, and a quality flag is set.

The *Energy Balance Model* process discriminates New/Young ice from All other thicker ice by an energy balance derivation of ice thickness from ice temperature. Surface air temperature, surface air humidity, surface wind velocity, surface pressure, and snow depth are required ancillary data for this method. Climatological snow depth is obtained from the Snow Depth/Ice Thickness LUT. The following steps are implemented:

a. Snow depth on the ice cover is modeled as a function of ice thickness, using climatological snow depth data in the Snow Depth/Ice Thickness LUT.

b. Surface air temperature, surface air humidity, surface pressure, and surface wind velocity are obtained from a VIIRS regridded IPs. These IPs will contain the most recent available data from the National Centers for Environmental Prediction (NCEP) forecasts or from CMIS.

c. Snow depth for the threshold ice thickness (30 cm, TBD) is computed from an energy balance (heat flux) equation that expresses ice thickness as a function of ice surface temperature, surface air temperature, surface air humidity, surface pressure, surface wind velocity, and snow depth.

d. The pixel is classified as New/Young ice if the computed snow depth is less than the climatology LUT snow depth value for the threshold ice thickness bin value,

Both methods use surface reflectance and surface temperature corresponding to ice itself, corrected according to ice fraction retrieved by the ice concentration algorithm. The pixels are aggregated to a horizontal cell. The size of the cell is determined by a pre-set value obtained from the Ice Age LUT. The ice types for each pixel in the cell are

examined for consistency. The predominant ice type is selected as the cell type. If there is no predominant type, the cell is typed as “All other ice”.

For each cell, the types from reflectance and temperature are compared. If they are different, the type with the greater weight is selected and a quality flag is set.

Ice type for each horizontal cell is written to the VIIRS Sea Ice Characterization EDR. Quality flags are also written to the EDR.

The process flow is described in detail in the VIIRS Snow/Ice Module Level Software Architecture document *[Y2477]* and the Ice Age Unit Level detailed design document *[Y3231]*.

3.2 ALGORITHM INPUT

3.2.1 VIIRS Data

The VIIRS Sea Ice Characterization EDR requires the VIIRS data listed in Table 3.

Table 3. VIIRS Data for the Sea Ice Characterization EDR

Input Data	Source of Data
Instrument (Band) Quality	VIIRS EV_375M SDR
Geodetic Coordinates	VIIRS EV_375M SDR
Geodetic Coordinates	VIIRS EV_750M SDR
Solar/Sensor Angles	VIIRS EV_375M SDR
Aerosol Optical Thickness (AOT)	VIIRS Aerosol Optical Thickness IP
Cloud Optical Thickness (COT)	VIIRS Cloud Optical Thickness IP
Visible TOA Reflectance	VIIRS EV_375M SDR
Near IR TOA Reflectance	VIIRS EV_375M SDR
Surface Temperature	VIIRS Surface Temperature IP
Cloud Mask	VIIRS Cloud Mask IP
Land/Water Mask	VIIRS Cloud Mask IP
Ice Quality Parameters	VIIRS Ice Quality LUT
Ice Concentration Parameters	VIIRS Ice Concentration LUT
Ice Age Parameters	VIIRS Ice Age LUT
Ice Broadband Albedo	VIIRS Ice Reflectance LUT
Ice Spectral Albedo	VIIRS Ice Reflectance LUT
Ice TOA Reflectance	VIIRS Ice Reflectance LUT
Snow Depth from Climatology	VIIRS Snow Depth/Ice Thickness LUT
Atmospheric Transmittance	VIIRS Atmospheric Transmittance LUT

Instrument (Band) Quality

The VIIRS EV_375M SDR will contain quality flags for each band at imagery pixel resolution. Pixels with bad quality for a given band will be assigned zero band weight.

Geodetic Coordinates

The VIIRS EV_375M SDR will contain geodetic latitude and longitude of each imagery resolution pixel. Geodetic coordinates will be used to exclude pixels outside of the Horizontal Coverage range for the EDR (c.f. Table 1). This exclusion is quite useful in reducing the VIIRS processing load, as most VIIRS granules will be outside of the range. Granule out of range flags will allow the ground system to bypass all EDR processing for those granules. The geodetic coordinates will also be used to extract the climatological snow depth. The VIIRS EV_750M SDR will contain geodetic latitude and longitude of each moderate resolution pixel. The moderate resolution geodetic coordinates will be used to and to derive latitude/longitude coordinates for the horizontal cells of the VIIRS swath, which will be written to the output EDR file.

Solar / Sensor Angles

The solar zenith angle (SZA) will be used to determine the relative weight of the reflectance-based and temperature-based retrievals. Each of the bands (I1, I2, and I5) will have pixel weights. Bands I1 and I2 will be progressively de-weighted as the SZA increases, providing a seamless transition across the terminator. The weighting function will be determined by pre-launch validation, as part of the initialization plan, and will be adjusted off-line by post-launch validation. The weighting function will be obtained from the Ice Quality LUT.

The SZA, viewing zenith angle (VZA) and relative azimuth angle (RELAZ) will be used in the *Reflectance Threshold Model* process to derive the expected TOA ice reflectance from the model TOA reflectance stored in the Ice Reflectance LUT (c.f. Section 3.3.1.3).

SZA will also be used in the derivation of the atmospheric transmittance in the *Energy Balance Model* process.

Aerosol Optical Thickness

Aerosol optical thickness (AOT) is obtained at moderate pixel resolution from the Aerosol Optical Thickness IP. It is used in the *Ice Quality* process to derive pixel quality and pixel weight, and in the *Reflectance Threshold Model* process to derive the expected TOA ice reflectance from the model TOA reflectance stored in the Ice Reflectance LUT (c.f. Section 3.3.1.3). It is also used in the derivation of the atmospheric transmittance in the *Energy Balance Model* process.

Cloud Optical Thickness

Cloud optical thickness (COT) is obtained at moderate pixel resolution from the Aerosol Optical Thickness IP. It is used in the *Ice Quality* process to derive pixel quality and pixel weight, as a switchable supplement to the Cloud Mask.

Visible and Near Infrared TOA Reflectance

Discrimination of ice from open water can be made on the basis of their reflectance spectra. The VIIRS EV375M SDR *[Y3216]* will supply TOA Reflectance for the I1 and I2 bands used by the *Ice Concentration* process *[Y3235]* to determine ice reflectance and ice concentration.

Surface Temperature

Surface temperature of the ice is needed for ice concentration retrieval at night, and is often useful for daytime retrievals. The VIIRS Surface Temperature IP algorithm *[D43761]* will determine the surface temperature for each imaged pixel, which will be supplied as a Surface Temperature IP *[D43761]*. The *Ice Concentration* process uses surface temperature to determine ice temperature and ice concentration. The *Sea Ice Age* process *[Y3231]* uses ice temperature to classify pixels as New/Young ice or All other ice.

Cloud Mask

The VIIRS cloud mask *[D43766]* is expected to derive a status of confident clear / probably clear / probably cloudy / confident cloudy for each pixel, building on MODIS cloud mask heritage (Ackerman *et al.*, 1997). Pixels classified as “cloudy” will be excluded from further processing. Pixels classified as “probably cloudy” are also expected to be excluded but their exclusion is controlled through quality de-weighting. This determination must depend on an assessment of the cloud mask performance, particularly over snow and ice surfaces. Pixels classified as “probably clear” will be processed. For these pixels, the pixel weight will be reduced by a factor obtained from the Ice Quality LUT, and a pixel quality flag will be written to the output EDR. Pixels classified as “confident clear” will be processed with no weight reduction. It is anticipated that the cloud mask will also flag pixels that are shadowed by clouds. In that case, a cloud shadow weight reduction factor will be assigned to those pixels and a shadow quality flag will be written to the EDR. The cloud mask will also supply thin cirrus, sun glint, and active fire flags, which our algorithm will use to assign pixel weight and pixel quality to the data.

Land / Water Mask

The EDR will be reported for ocean pixels within the Horizontal Coverage range. Land pixels, Inland Water pixels, Coastal pixels and pixels outside of the Horizontal Coverage range will be excluded from further processing. Information on Land/Ocean/Inland Water/Coastline status will be obtained from the Cloud Mask IP, using the best quality land/water map available.

Ice Quality Parameters

A set of input parameters will be obtained from a pre-set VIIRS Ice Quality LUT. The parameters include ranges for sea ice horizontal coverage and fresh water ice horizontal coverage. Pixels outside of the horizontal coverage range will be de-weighted so that they will be excluded from processing. The parameters also include a switch determining whether to use the Cloud Mask IP or the Cloud Optical Thickness IP for cloud masking, default relative weights for the I1, I2, and I5 bands, and weight reduction factors for various types of clouds, AOT, and SZA. The values of these parameters will be determined by initialization and validation activities (Section 4.3).

Ice Concentration Parameters

A set of input parameters will be obtained from a pre-set VIIRS Ice Concentration LUT..

These parameters direct the implementation of the ice concentration algorithm *[Y2466]* in the Ice Concentration software unit. They include search window pixel size, ice/water thresholds, and histogram bin sizes. The values of these parameters will be determined by initialization and validation activities (Section 4.4).

Ice Age Parameters

A set of input parameters will be obtained from a pre-set VIIRS Ice Age These parameters direct the implementation of the ice age algorithm in the Sea Ice Age

software unit. They include the minimum required ice concentration, the minimum required pixel/band weights, the horizontal cell size, the values of physical constants used for energy balance, sensor noise models.

Ice Age / Thickness

The threshold thickness value separating Young ice from older ice, obtained from the Ice Age LUT. Currently, the LUT contains a single value (0.3 meters). Potentially, it can be expanded to a dependence on region and season.

Ice Broadband Albedo

Model ice broadband albedo is stored in the Ice Reflectance LUT as a function of ice thickness and snow depth on the ice. The model is derived from a combined 6s/DISORT radiative transfer model (RTM), as described in Section 3.3.1.3. The *Energy Balance Model* process uses the ice broadband albedo to estimate the downward shortwave energy flux.

Ice Spectral Albedo

Model ice spectral albedo is stored in the Ice Reflectance LUT as a function of ice thickness and snow depth on the ice. The model is derived from a combined 6s/DISORT radiative transfer model (RTM), as described in Section 3.3.1.3.

Ice TOA Reflectance

Model TOA reflectance is stored in the Ice Reflectance LUT as a function of ice thickness, snow depth on the ice, solar/viewing angles, and atmospheric conditions. The model is derived from a combined 6s/DISORT radiative transfer model (RTM), as described in Section 3.3.1.3. The *Reflectance Threshold Model* process compares model reflectance to observed reflectance to derive ice thickness.

Snow Depth from Climatology

The energy balance equation includes snow depth. The flux through the ice sheet is very sensitive to the depth of its snow cover, because of the relatively low thermal conductivity of snow (c.f. Equation 3.3.2.1.10). A relatively shallow snow cover can therefore significantly affect the surface temperature. This has been a serious impediment to operational retrieval of ice age from IR data. Shallow snow cover (< 10 cm) is not easily derived from passive microwave. We must therefore estimate snow depth from climatological models or data bases. The average snow depth for a given ice thickness is modeled from a climatological average of surface air temperature and snowfall rate for the appropriate region and season. It will be a function of time interval that has elapsed since the beginning of ice formation, hence ice thickness. Climatological snow depth is derived as a function of ice thickness, location (latitude/longitude), and date, and is stored in a Snow Depth/Ice Thickness LUT. See section 3.3.4.1.1 for a discussion of the development of this LUT.

Atmospheric Transmittance

The atmospheric transmittance of the downward shortwave flux is used by the *Energy Balance Model* process to derive the expected shortwave flux incident on the snow/ice surface. It is modeled as a function of SZA, AOT, and aerosol model, using the 6s RTM, and is stored in an Atmospheric Transmittance LUT. See Section 3.3.4.1 for a discussion of the development of this LUT.

3.2.2 Non-VIIRS data

The required Non-VIIRS data for the Sea Ice Characterization EDR is summarized in Table 4.

Table 4. Ancillary Non-VIIRS data for the VIIRS Sea Ice Characterization EDR

Input Data	Source of Data	Reference
Water Vapor Optical Thickness	VIIRS Regridded IP	*[Y7051]*
Ozone Optical Thickness	VIIRS Regridded IP	*[Y7051]*
Surface Air Temperature	VIIRS Regridded IP	*[Y7051]*
Surface Humidity	VIIRS Regridded IP	*[Y7051]*
Surface Pressure	VIIRS Regridded IP	*[Y7051]*
Surface Wind Speed	VIIRS Regridded IP	*[Y7051]*

Water Vapor Optical Thickness

Total precipitable water (PW) is obtained at moderate pixel from a VIIRS regridded IP *[Y7051].* Water vapor optical thickness (WVOT) is computed from PW, and used in the *Reflectance Threshold Model* process to derive the expected TOA ice reflectance from the model TOA reflectance stored in the Ice Reflectance LUT (c.f. Section 3.3.1.3).

Ozone Optical Thickness

Total column ozone profile is obtained at moderate pixel resolution from a VIIRS regridded IP *[Y7051].* Ozone optical thickness (OOT) is computed from the total column ozone profile, and used in the *Reflectance Threshold Model* process to derive the expected TOA ice reflectance from the model TOA reflectance stored in the Ice Reflectance LUT (c.f. Section 3.3.1.3).

Surface Air Temperature

The *Energy Balance Process* requires recent surface air temperature to calculate the heat flux through the ice sheet, as discussed in Section 3.3.5.1. Surface air temperature will be obtained from NCEP forecasts and regridded to the VIIRS moderate resolution swath. If NCEP data are not available, it would be desirable to have a fallback source. Air temperature can be determined by NPP/CrIMMS and NPOESS/CMIS as a boundary condition on the Atmospheric Vertical Temperature Profile EDR. It will be desirable for

CrIMMS and CMIS to report surface air temperature, though it is not a specified requirement for either sensor.

Surface Air Humidity

The *Energy Balance Process* requires an estimate of surface air humidity to calculate the heat flux through the ice sheet, as discussed in Section 3.3.4.1. Surface air humidity will be obtained from NCEP forecasts and regridded to the VIIRS moderate resolution swath. If NCEP data are not available, it would be desirable to have a fallback source. Air temperature can be determined by NPP/CrIMMS as a boundary condition on the Atmospheric Vertical Moisture Profile EDR. It will be desirable for CrIMMS to report surface air humidity, though it is not a specified requirement for either sensor.

Surface Pressure

The *Energy Balance Process* requires an estimate of surface pressure to calculate the heat flux through the ice sheet, as discussed in Section 3.3.4.1. Surface pressure will be obtained from NCEP forecasts and regridded to the VIIRS moderate resolution swath.

Surface Wind Velocity

The *Energy Balance Process* requires an estimate of surface wind velocity to calculate the heat flux through the ice sheet, as discussed in Section 3.3.4.1. Surface wind velocity will be obtained from NCEP forecasts and regridded to the VIIRS moderate resolution swath.

3.3 THEORETICAL DESCRIPTION OF THE RETRIEVAL

In the following sections, the mathematical background of the processes outlined in Section 3.1 will be described. These processes only apply to regions that successfully passed the quality examinations.

3.3.1 Physics of the problem

Ice age and concentration are derived from the differences in reflectance and temperature characteristic of ice in various stages of development. The characteristics of ice surfaces are influenced by snow cover. An understanding of the effect of snow on the surface reflectance and surface temperature is required.

3.3.1.1 Snow Reflectance

The reflectance of snow is unique among land cover types. It is among the brightest of natural substances in the visible and near-infrared part of the spectrum, but it is also often the darkest in the short wave infrared (Dozier, 1989). The spectral albedo of snow is wavelength-dependent, and this spectral dependency is controlled by the imaginary part *(k)* of the complex refractive index. This reaches a minimum at a wavelength of

about 0.46 microns, and increases by a factor of $10^6 – 10^7$ as wavelength increases out to 2.5 microns (Warren, 1982; Dozier, 1989).

Light in snow is scattered primarily by refraction through the ice grains. Nearly 89 percent is refracted through the grain, and 8 percent is scattered after internal reflections (Bohren and Barkstrom, 1974). Because ice is so transparent to visible radiation, snow reflectance is only weakly sensitive to grain size in bands below 0.7 microns, but sensitive to light absorbing impurities in the snow and, for optically-thin snowpacks, to snow water equivalent (SWE; Wiscombe and Warren, 1980; Grenfell, Perovich, and Ogren, 1981). Because light absorption by ice is much stronger in bands above 1.4 microns, reflectance at these wavelengths is relatively insensitive to absorbing impurities and SWE, but sensitive to changes in grain size, especially for grain radii less than 500 microns. Light absorbing particulates, such as dust and soot, affect snow reflectance out to 0.9 microns (Warren and Wiscombe, 1980), so the 0.86 micron band is sensitive to both absorbing impurities and grain size.

Clouds and snow are both bright across the visible and near-infrared region, but clouds are much brighter than snow in the short wave infrared (SWIR). This is because the smaller size of the scatterers in clouds decreases the probability of absorption in this spectral region where ice and water are moderately absorptive (Crane and Anderson, 1984; Dozier, 1984, 1989). Conversely, bodies of open water are dark at all wavelengths. Vegetation is dark in the visible bands because of absorption by photosynthetic pigments, but has a maximum reflectance between 0.7 and 1.3 microns. Because of leaf cell structure (Hoffer, 1978), SWIR reflectance is inversely related to leaf water content for healthy vegetation. Nevertheless, the reflectance at wavelengths longer than 1.5 microns is still high compared to that of snow. Most rock and soil spectra are the reverse of snow's. Absorption by iron oxides and organic matter strongly reduce visible reflectance, while those in the SWIR remain high.

3.3.1.2 Ice Reflectance

Reflectance from ice surfaces differs from snow reflectance because the ice consists of sheets rather than grains. Clear ice slabs are highly transmitting (Bolsenga, 1983). Reflectance occurs by scattering from impurities, such as brine pockets and air bubbles. Therefore, the reflectance observed from natural ice surfaces is highly variable, depending on the condition of impurities for a given ice sheet. Given the wide variety of ice conditions in nature, ice reflectance is not as well determined as snow reflectance, which is amenable to Mie scattering theory (Warren, 1982) Studies of ice reflectance thus tend to be empirical.

Remote sensing studies of sea ice are relatively widespread and are of significant potential benefits. The wide range in spectral albedo observed in sea ice of various types and thickness is a well-established characteristic of sea ice. This characteristic is an important factor in the reflectance-based retrieval of ice age for New/Young ice from All other thicker ice.

Spectral albedo of sea ice at various bands undergoes significant changes depending upon ice structure and the condition of the ice surface. Spectral reflectance curves differ for different ice age. Each ice age has its own unique spectral signature, as shown in Table 5.

Table 5. Reflectance Characteristics of Ice Age Types

Stage of ice development	Characteristic thickness	Ice color	International nomenclature	SRD classes		Our interpretation of classes
Initial ice crystals	Less than 5 cm	Dark, mat	New ice	New Ice		New ice
Mat thin elastic ice	Up to 10 cm	Mat, whitish	Nilas			
Gray bending stable ice	10 – 30 cm	Grey, grey-white	Young ice	Young ice		Young ice
White fracturing ice of First Year grow period	More than 30 cm	White, light green, Greenish	First Year ice	First Year ice		First Year ice
Ice in the second year cycle of development	N/A	Green-blue	Second-Year ice		Old ice	Multi-year ice
Ice surviving more that two year cycles	N/A	Blue	Multi-Year ice	M-y ice		

On the whole, ice reflectance is correlated with ice age as it varies during the seasonal cycle. The correlation of snow depth with stage of development also contributes to the characteristic reflectance signature of different ice age classes.

3.3.1.3 TOA Reflectance Model

The expected TOA directional reflectance (TOA Bidirectional Reflectance Distribution Function (BRDF)) is derived from a combination of the DISORT and 6S radiative transfer models (RTMs). The TOA reflectance is computed and stored in the Ice Reflectance LUT for operational application of the sea ice algorithm.The VIIRS Ice Reflectance LUT is used to provide modeled TOA reflectance in two VIIRS imagery resolution bands for a variety of solar, sensor, and local angles, ice thickness, snow depth, and atmospheric conditions: The 6s V4.1 (Vermote et al. 1997) atmospheric radiative transfer model is used to model the top-of-the-atmosphere (TOA) reflectance.

In computing the TOA reflectance for each VIIRS band, the surface is assumed to be non-Lambertian and thus requires specification of the angular distribution of reflectance for each snow depth and ice thickness. To provide 6s with the surface BRDF, the DISORT (Stamnes et al. 1988) model is used to compute the BRDF data files. DISORT uses as input, three optical properties of snow and ice (optical depth, single scattering albedo, and the asymmetry parameter). Four output files from DISORT are read into 6s. These are:

(1) The spherical albedo

(2) The BRF for a specified solar zenith angle, computed at 10 discrete viewing zenith angles and 13 discrete relative azimuth angles (as specified by the 6S subroutine “brdfgrid”)

(3) The BRF for a sun at a specified viewing zenith angle, computed at 10 discrete solar zenith angles and 13 discrete relative azimuth angles (as specified by the 6S subroutine “brdfgrid”)

(4) The BRF for the sun at the specific solar zenith angle, sensor at the specific viewing zenith angle, and for the specific relative azimuth angle of the observation.

For additional information on brdfgrid, see the 6S User’s Guide Version 2, p141 (Vermote et al., 1997).

The computed TOA reflectance for each band, ice thickness, and snow depth is stored in the LUT.

The 6s radiative transfer model predicts the satellite signal from 0.25 to 4.0 microns assuming cloudless atmosphere. The main atmospheric effects (gaseous absorption by water vapor, carbon dioxide, oxygen and ozone; scattering by molecules and aerosols) are taken into account. Non-uniform surfaces may be considered, as well as bidirectional reflectances as boundary conditions, The 6s V4.1 model was written by Eric Vermote at NASA GSFC and can be accessed via anonymous ftp through kratmos.gsfc.nasa.gov.

Several changes were made to the original version of 6s in order to populate the LUT. One change was to hard-code several parameters into 6s. These include setting the observation platform to be satellite, setting the surface elevation to be 0, setting the atmospheric profile to be US62 (but you can vary the column amounts of water vapor and ozone), and selecting a non-Lambertian surface. It was decided to set the surface elevation to be 0 in the interests of simplification, to avoid a surface elevation parameter in the LUTs.

The core of the modeling effort that creates bidirectional reflectance factor (BRF) data for the snow/ice surface is the Discrete Ordinates Radiative Transfer (DISORT; Stamnes et al., 1988) code. DISORT is a plane-parallel radiative transfer program that is highly versatile for modeling scattering and absorption in particulate media. It works for a wide range of the electromagnetic spectrum from the UV to the microwave. It is a one-dimensional model with the vertical coordinate expressed in optical depth. DISORT can accommodate multiple layers of particulate media. Angular coordinates, for illumination and reflection, are expressed as azimuthal angles and polar angles. The number of computational polar angles (“streams”) influence the accuracy of the result. For computation of intensities, 48 streams are recommended. While the computations are performed for specific polar angles, the radiant quantities can be computed for any angle desired by the user.

Generating bidirectional reflectance factor (BRF) data with the Discrete Ordinates Radiative Transfer (DISORT) is performed using multiple steps.. All of this code requires the libraries from the software package Image Processing Workbench (IPW). This software is freely available from the University of California Santa Barbara Snow

Hydrology Research Group. Ice refractive indices (real and imaginary parts) are computed in the program refdxice, using interpolation from tables of refractive index data. This code uses refractive index data from Warren 1984, subsequent corrections by Warren (as described in the refdxice code documentation), as well as those of Kou et al, 1994. For each VIIRS channel used in the LUT, the refractive indices are computed for the wavelengths of the spectral response function (SRF) for each VIIRS channel.

The single scattering albedo and the asymmetry parameter are computed in the program miefast. Miefast is a C program wrapper for a Fortran 77 program originally written by Wiscombe's Mie calculation routine. The C wrapper was written by Jeff Dozier in 1987 and contributed to the IPW software package.

The spectral effective Mie parameters are computed for a mixture of ice particles and brine inclusions using a cross-sectional area weighting approach. Cross sectional area per unit volume of sea ice is computed for each particle type using the following equation: $A = N\pi r^2$ where, N is the number of particles in a cubic meter of ice and r is the particle effective radius. Particle weighting coefficients used in the linearization are calculated by normalizing the value of A for each particle type by the total cross-sectional area of all particles in a unit volume. The weights are then used to compute effective Mie parameters as follows:

$$\varpi_{eff} = c_{ice}\varpi_{ice} + c_{brine}\varpi_{brine}$$
$$\tau_{eff} = c_{ice}\tau_{ice} + c_{brine}\tau_{brine}$$

where the c values are the weights for ice and brine. In this program, brine concentrations are assumed to vary inversely with ice thickness so that an ice thickness of 5cm has a brine concentration of 0.20 (20%) and an ice thickness of 50 cm has a brine concentration of 0.02 (2%). These values are in line with those given in Perovich, 1996.

The extinction efficiency, particle size and snow thickness are used to compute optical thickness for the snow layer. Clean snow with a grain radius of 250 microns is assumed. Snow depths ranging from 0.25 to 3 cm are modeled. For snow depths greater than 3 cm, the TOA reflectance is insensitive to the thickness of the underlying ice sheet.

BRF, spherical albedo, and directional reflectance (rodir) are computed in the discord program. DISCORD is a C-program wrapper for the Fortran 77 program DISORT. DISORT is the program in which all the radiative transfer computations take place. DISCORD provides a command line interface for DISORT and allows it to be easily run from within a shell script. discord is part of Dr. Jeff Dozier's (UC-Santa Barbara) set of contributed programs to the IPW software package.

Inputs to discord include the number of computational streams (currently set at 48), reflectance of the substrate (currently set at 0.01), cosine of the solar zenith angle, direct and diffuse irradiance (diffuse irradiance is zero, direct irradiance is normalized by the solar cosine so that the total irradiance = 1.0), viewing zenith cosines (for viewing

zenith angles 0-80 in 10 degree increments and 85 degrees), relative azimuth angles (0 to 360 in 30 degree increments), and an argument that specified that the intensities should be computed only at the snow/ice surface. TOA reflectances were computed for the 6S maritime and continental aerosol models. The aerosol model index which determines the aerosol type to be retrieved from the LUT is determined based on an Arctic Haze AOT threshold defined as a tunable parameter. The aerosol model index is set to maritime for AOT values less than the threshold value. The sea ice algorithm interpolates between the nodes to derive an expected TOA reflectance for the conditions at a given pixel.

3.3.1.4 Water Reflectance

The reflectance spectral signature of open water is significantly different from snow/ice reflectance, except for the thinnest ice surfaces. This reflectance contrast allows for a calculation of ice fraction during daytime by the derivation of distinct ice and water reflectance tie points. The algorithm for retrieval of ice concentration *[Y2466, D43761]* derives the tie points. The ice reflectance tie points are passed to the ice age daytime algorithm.

3.3.1.5 Surface Temperature

During a great part of the seasonal cycle, infrared bands will be the only available information to retrieve ice age and ice fraction. Infrared radiance allows us to calculate surface temperature. Infrared information is useful when there are thermal contrasts between water and ice surfaces.

Changes in sea ice surface temperature are governed by the joint influence of vertical heat fluxes of different origin. The intensity of turbulent exchange by heat between the atmosphere and underlying ice surface, as well as the surface balance of long-wave radiation, directly depend on ice surface temperature. Vertical heat flux through ice cover is an explicit function of the vertical ice temperature profile, which depends on ice surface temperature. Thus, all main components of heat exchange between the atmosphere and the underlying ice surface (except short-wave radiation fluxes) are explicit functions of ice surface temperature.

In the winter, heat flux between the atmosphere and ice is compensated by ice growth at the underside of the ice. There are no vertical changes in heat flux at the boundary between air and ice surface. At the same time, many components of heat flux depend on ice surface temperature. Therefore, conditions of conservation of vertical heat flux at the surface can be fulfilled only if ice surface temperature is adjusted to varying influencing environmental conditions.

Ice thickness is the main factor determining vertical heat flux through the ice under specified atmospheric conditions. Thus, a general conclusion about the relation between ice surface temperature and thermodynamic processes in ice cover and atmospheric boundary layer can be formulated. Ice surface temperature is determined

by the processes of vertical heat exchange and is a distinctive indicator of ice thickness. Given the same atmospheric conditions, New or Young ice will have a lower surface temperature than thicker First Year ice.

3.3.2 Ice Quality and Ice Weights

The quality of the VIIRS Sea Ice Characterization EDR products will be degraded by the presence of clouds and aerosols in the path of the TOA radiance that is received at the sensor. Clouds and aerosols will have a varying effect, depending on optical thickness, type, and wavelength. Degradation will also occur due to effects of coastline and sun glint. To account for these varying degradations, we determine weights for each pixel/band combination for probably cloudy, thin cirrus, cloud shadow and aerosol contaminated pixels.

The *Ice Quality* process performs pixel masking and pixel weighting, using information in the VIIRS EV_375M SDR *[D43777]*, VIIRS Aerosol Optical Thickness IP *[Y2388]*, VIIRS Cloud Optical Thickness IP *[Y2472]*, VIIRS Cloud Mask IP *[Y2412]*, and the Ice Quality LUT (c.f. Section 3.2.1). The process produces an imagery resolution pixel quality flag mask and pixel weights for each band.

The “Sea Ice Range” flag is set if the VIIRS Cloud Mask IP *[D43766]* indicates that the pixel is not entirely an ocean surface or if the pixel latitude is outside of the sea ice latitude range. The “Fresh Water Ice Range” flag is set if the VIIRS Cloud Mask IP *[D43766]* indicates that the pixel is entirely an ocean surface or if the pixel location (latitude, longitude) is outside of the fresh water ice (latitude, longitude) range. The “Coastline” flag is set if the VIIRS Cloud Mask IP indicates that the pixel contains coastline. The “Cloud Quality” flag reproduces the Cloud Confidence bits of the VIIRS Cloud Mask IP. The “Thin Cirrus” flag reproduces the Thin Cirrus bits of the VIIRS Cloud Mask IP. The “Cloud Shadow” flag is set if the VIIRS Cloud Mask IP indicates that the pixel contains cloud shadow. The “Cloud Phase” flag indicating "Water, Ice Mixed" are based on remapped Cloud Phase bits of the VIIRS Cloud Mask IP. The “Fire” flag is set if the VIIRS Cloud Mask IP indicates that the pixel contains an active fire. The “Sun Glint” ” flag is set if the VIIRS Cloud Mask IP indicates that the pixel is contaminated by sun glint. The “Band Quality” flags are set if the VIIRS SDR indicates that the pixel contains bad data for that band.

The “Overall Quality” flag contains two bits for each band. These bits indicate “Green”, “Green/Yellow”, “Yellow/Red”, and “Red” quality. The algorithm assigns one of the four quality conditions to each (pixel, band) combination by determining weights. If the (pixel, band) weight is greater than the “Green” threshold value, a “Green” quality is assigned. If the (pixel, band) weight is less than the “Green” threshold value and greater than the “Yellow” threshold value, a “Green/Yellow” quality is assigned. If the (pixel, band) weight is less than the “Green/Yellow” threshold value and greater than the “Yellow/Red” threshold value, a “Yellow/Red” quality is assigned. Finally, if the (pixel, band) weight is less than the “Yellow/Red” threshold value, a “Red” quality is assigned.

The weights are obtained by reducing an initialized band weight (w_0) by various weight reduction factors:

$$w(band,pixel) = w_0(band)*w_1(band,pixel)*w_2(band, pixel)*\ldots*w_N(band,pixel) \quad (3.3.2.1)$$

where w_N are the various weight reduction factors. These include Clouds, Cloud Shadows, Thin Cirrus and Aerosols. Weight reduction factors are obtained from the Ice Quality LUT (c.f. Table 6). It is expected that these factors will be revised by future algorithm performance analysis.

The ice quality bits for each pixel are written to an Ice Quality Flags IP, for use by the Ice Concentration, and Ice Age software units. The band weights for each pixel are written to an Ice Weights IP, for use by the Ice Concentration, and Ice Age software units.

3.3.3 Mathematical Description of the Ice Concentration Algorithm

Under conditions where there is a predominant ice type in a local area, ice fraction for each imaged pixel can be retrieved by the direct application of a tie point method. The tie point is a special case of spectral mixture analysis, restricted to two end members. The end member signatures are derived from identifying pure pixels in the scene.

The ice fraction for a mixed pixel is:

$$f(p) = (b_p - b_{water}) / (b_{ice} - b_{water}) \quad (3.3.3.1)$$

where: $f(p)$ is the calculated ice fraction
b_{ice} is the brightness value of a pure ice pixel
b_{water} is the brightness value of a pure water pixel
b_p is the brightness value of the pixel

Our algorithm acquires three independent brightness values for each pixel. These are a visible reflectance, a near IR reflectance, and a temperature. To take advantage of all of the available information, our algorithm computes a band weighted average ice fraction. In that case:

$$f(p) = (\Sigma_j (w_j)(b_{jp} - b_{jwater}) / (b_{jice} - b_{jwater})) / \Sigma_j w_j \quad (3.3.3.2)$$

or:

$$f(p) = \Sigma_j (w_j \ f_j(p)) / \Sigma_j w_j \quad (3.3.3.3)$$

where: $f(p)$ is the calculated ice fraction

$f_j(p)$ is the ice fraction calculated from band j
w_j is the relative quality weight in band j
b_{jice} is the jth brightness value of a pure ice pixel
b_{jwater} is the jth brightness value of a pure water pixel
b_{jp} is the jth brightness value of the pixel

The relative quality weight w_j, included to allow for other band-dependent factors, is obtained from the Ice Weights IP. This IP, produced by the Ice Quality process, contains pixel weights for each band, determined by clouds, SZA, AOT, etc.

Our approach is to calculate ice fraction for each band, according to equation 3.3.3.1, and derive a band-weighted ice fraction, according to equation 3.3.3.3. Errors in deriving b_{ice} *and* b_{water} have been an obstacle to achieving global operational ice concentration retrieval. Our algorithm greatly reduces these errors by deriving tie points from the scene. During the melt sea season, melt pond water formed over ice with above freezing temperatures during day can result in failure of the thermal band retrieval due to ice detection failure (no thermal band ice tie point). The band weighted mean fraction is therefore computed with only the contributions from the reflective band retrieved fractions whenever there are valid reflective band retrievals and an invalid thermal retrieval due to no thermal ice tie point.

An ice/water threshold is derived to select the pixels used for the water distribution for scenes containing open water. We assume that a scene-corrected threshold corresponds to the minimum probability of reflectance and/or temperature located between values associated with water and ice. Location of the minimum is found by use of a sliding integral taken over the probability density of the parameter (reflectance or temperature). The range of measured parameter values is divided into a specified number of histogram bins. This number is obtained from the Ice Concentration LUT. The histogram of the distribution for the scene is computed. The histogram is smoothed by a running boxcar filter of specified width, producing a sliding integral of the parameter distribution. The width of the filter is also obtained from the Ice Concentration LUT. The lowest value of the sliding integral is adopted as the ice/water threshold.

The water tie point is selected as the maximum in probability density distribution corresponding to the maximum of the sliding integral over water reflectance (temperature). We analyze water characteristics only in the immediate vicinity of the ice zone. It allows us to improve the accuracy of water tie point determination as it eliminates water characteristics for areas far away from ice cover. Those characteristics can differ from open water properties in the vicinity of the ice zone.

A scene-corrected ice threshold is derived as the first minimum of the sliding integral of the parameter distribution. The water tie point is selected as the maximum of the sliding integral below the ice/water threshold. Figure 8 illustrates the process.

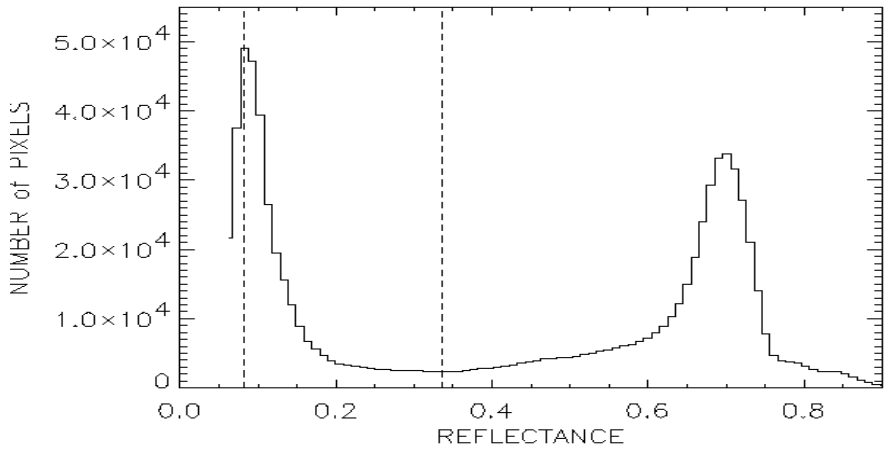

Figure 8. Distribution of 640 nm reflectance for an ice/water scene.

The ice/water threshold reflectance (0.336) and the water tie point (0.083) are indicated in Figure 8 by the vertical dashed lines.

For every imaged pixel, ice reflectance and/or surface temperature corresponding to an ice tie point (pure pixel) is calculated as the most probable reflectance and/or ice surface temperature in the vicinity of the pixel under consideration.

The ice tie point is derived locally for each pixel whose parameter value is on the ice side of the ice/water threshold. The distribution of parameter values in a local search window is acquired. The ice tie point is selected as the maximum value for a sliding integral of the local parameter distribution. Figure 9 illustrates the process.

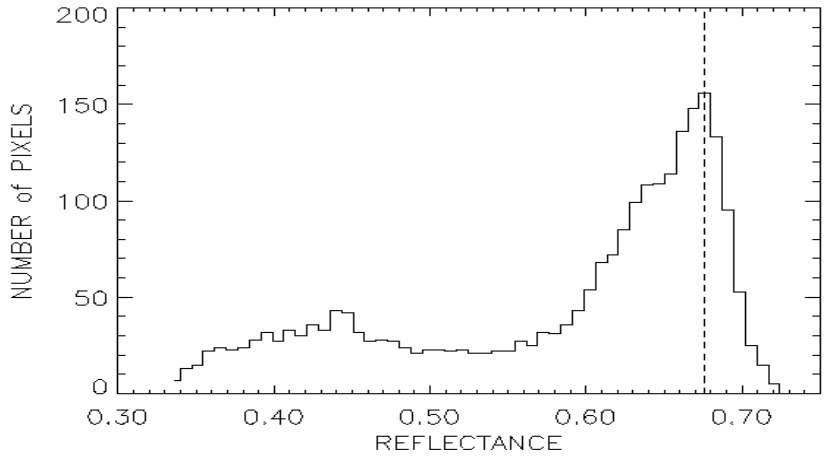

Figure 9. Distribution of 640 nm reflectance for a local search window

For each pixel, a search window is used to establish the ice tie points from the local distribution of reflectance and/or surface temperature at the spatial scale of the window. The ice tie point is selected as the maximum value for a sliding integral of the local parameter distribution within the search window. For the example presented in Figure 9, the ice tie point for the pixel is equal to 0.676, indicated by the vertical dashed line. The accuracy of the ice tie point selection depends on the size of the local search window, which is obtained from the Ice Concentration LUT. A larger search window will contain more pixels, thereby increasing the statistical robustness of the distribution. This is achieved at the expense of greater intrinsic variation in the condition of the ice within the search window, leading to an increased bias between the true ice condition of the central pixel and the derived ice condition of the search window. Optimization of the search window size, which will therefore improve algorithm performance, is a primary goal of algorithm initialization and validation.

Having selected the ice and water tie points appropriate to a given pixel, the algorithm applies equation 3.3.3.1 to retrieve the ice fraction for each pixel. Ice concentration is reported as the ice fraction of each pixel. Concentrations less than 0.0 are set to 0.0. Concentrations greater than 1.0 are set to 1.0.

In the case where open water pixels are not found in the search window, an ice concentration of 1.0 is assigned to the central pixel of the window and the observed reflectance and temperature values are adopted as the ice tie points. The assignment of 100% ice fraction in this case results in a bias in that fractional ice associated with sub-pixel open water in ice fractures and leads will not be detected. An alternative approach is thus provided as an algorithm option to compute an adjusted ice tie point for addressing such biases for this special case. An adjusted ice tie point is computed as a function of the observed reflectance and is allowed to take on values close to the central pixel value but may allowed to vary linearly up to the value of the computed ice tie point of the window.

$$m_p = (b_{jice} - b_{jice\_adj\_thinice\_thresh}) / (b_{jice} - b_{jwater\_global}) \quad (3.3.3.4)$$

$$b_{jice\_adj} = (m_{jp})(b_{jp} - b_{jwater\_global}) + b_{jice\_adj\_thinice\_thresh} \quad (3.3.3.5)$$

where:
b_{jice_adj} is the jth adjusted brightness value of pure ice pixel
$b_{jice\_adj\_thinice\_thresh}$ is the jth thin ice adjustment threshold brightness
b_{jwater_global} is the jth global default brightness value for water
b_{jice} is the jth brightness value of a pure ice pixel
b_{jp} is the jth brightness value of the pixel
m_p is the jth slope of the linear ice tie point adjustment for a pixel

Invoking the optional ice tie point adjustment and controlling the magnitude of the adjustment as well as limiting its application to regions with surface temperatures well below freezing are performed through use of tunable parameters (ice temperature threshold, ice tie point adjustment thresholds). The prelaunch values of the tunable parameters settings have been determined based on testing with MODIS proxy test

scenes and are documented in the [D42821] - Operational Algorithm Description Document for VIIRS Sea Ice Concentration Intermediate Product (D4280). The optimal values of the tunable parameters may be determined as part of calibration/validation activities. Although true ice fraction values may not be computed without prior knowledge of the ice type for this case, the adjustment scheme provides a mechanism for addressing correction of ice concentration biases and identification of ice fracture lead zones as fractional ice.

3.3.4 Mathematical Description of the Sea Ice Age Algorithm

The algorithm classifies ice type by using three methods:

(1) Discrimination of New/Young ice from All other thicker ice is achieved by an energy balance derivation of ice thickness from ice temperature. This method will be applied at nighttime and for low sun angle conditions.

(2) Discrimination of New/Young ice from All other thicker ice is achieved by application of a reflectance threshold. This method will be applied at daytime.

Both methods use reflectance and surface temperature corresponding to ice itself, corrected according to ice fraction retrieved by the *Ice Concentration* process (Section 3.3.3).

3.3.4.1 Energy Balance Model

We use data on ice surface temperature and surface air temperature to calculate ice thickness on the basis of a thermodynamic model of energy balance. Parameters of the thermodynamic model are determined as functions of season and region. Regional studies demonstrate that such calculations can effectively discriminate ice age for a range of sea ice age from new ice through medium First Year ice (Yu and Rothrock, 1996).

The equation of heat balance is usually used as a basis for calculating thermodynamic changes of sea ice mass. The equation includes the heat fluxes of different origination: radiation, turbulent fluxes, ice heat conductivity. If information on air temperature and ice surface temperature is available, we can transform the mathematical formulation and use the same equation of heat balance to determine ice thickness (age).

The equation of surface heat balance for ice (snow) surface reflects the conservation of vertical heat flux. In other words, heat flux between ice surface and the atmosphere is equal to resultant heat flux through ice.

In general, the equation of surface heat balance has the following form:

$$Q_s = Q_\Sigma(1-\alpha) + E_a - E_s + Q_t + Q_e, \qquad (3.3.4.1.1)$$

where: Q_S - resultant heat flux from the atmosphere to the ice (snow) surface,
Q_Σ - total incident short-wave solar radiation,
α - surface albedo,
E_a - long-wave radiation from the atmosphere,
E_S - long-wave radiation from surface,
Q_t - turbulent heat exchange,
Q_e - heat exchange due to evaporation.

Total incident shortwave solar radiation is a sum of direct solar radiation projected onto a horizontal surface and diffusive radiation. It depends upon solar zenith angle, latitude, day of seasonal cycle, atmosphere transparency, and cloudiness. We do not partition total short-wave solar radiation into direct and scattered radiation as their combined effect is important for energy calculation. We estimate as the product of the solar irradiance at the top of atmosphere and an atmospheric transmittance factor. For top of atmosphere solar irradiance, we use the 6S value of 1368 W/m^2. This differs from the AM0 (air mass zero) standard value of 1366.1 W/m^2 that is used by the American Society for Testing and Materials (http://rredc.nrel.gov/solar/spectra/am0/). The 0.2% difference is not significant, compared with the uncertainties in the atmospheric transmittance. The solar irradiance varies by ~ 0.1% over the 11 year solar cycle. This variation is also insignificant. The atmospheric transmittance factor is obtained from a Broad Band Transmittance LUT. This LUT stores atmospheric transmittance values for a solar zenith angle (SZA) range of 48 - 88 degrees, and an AOT range of 0.01 – 1.0. The LUT is populated by the 6S RTM for the SZA range of 48 – 80 degrees. Data for greater SZA are filled by extrapolation from lower SZA.

The absorbed fraction of solar radiation depends upon the state of ice (snow) surface. The surface reflectance varies in a very wide range, from a few percent for water surface up to 98% for fresh snow. Albedo is a very important factor determining variability of the surface heat balance. We use a model snow/ice surface albedo, obtained from the Ice Reflectance LUT (c.f. Section 3.3.1.3).

The second and the third terms of Equation 3.3.4.1.1 determine fluxes of long-wave radiation. Different mathematical forms were proposed by researchers to present these terms in the equation. Existing empirical formulae reflect dependence of the fluxes on air temperature, humidity, and cloudiness. As an appropriate approximation, we can use magnitudes of air temperature and humidity near the surface (2 m above surface is a standard height).

We propose to use the results of radiation balance studies in the polar areas to calculate long-wave heat fluxes near the surface. Magnitudes of air temperature and humidity at the level of 2 m are considered sufficient to calculate long-wave radiation from the atmosphere. We chose the following formula obtained on the basis of processing numerous measurements of radiation fluxes:

$$E_a = (a + b\sqrt{e})\,\sigma_B\,T_a^4 \qquad (3.3.4.1.2)$$

where:

σ_B - Stephan-Boltzmann constant,
T_a - Air temperature
e - absolute air humidity

Empirical coefficients a, and b characterize regional conditions in high latitudes. The humidity exerts a significant effect on variation of long-wave radiation from the atmosphere in low and moderate latitudes. In the polar regions, the effect of humidity is less noticeable.

The absolute air humidity is computed from the relative humidity (H_{REL}) and air temperature (T_a) at the surface:

$$e = 1.E5 * P_V / 461.51 / T_a \qquad (3.3.4.1.3)$$

where:

$$P_V = 6.112 * 10.\ **\ (7.5*T_{DEW}(\text{Celsius}) / (237.7+T_{DEW}(\text{Celsius}))) \qquad (3.3.4.1.4)$$

is the vapor pressure (mbar) and:

$$T_{DEW}(\text{Celsius}) = 1. / (1./T_a - 1.846E\text{-}4 * \ln(H_{REL})) - 273.16 \qquad (3.3.4.1.5)$$

is the dew point temperature.

Long-wave radiation flux from a surface is determined as:

$$E_s = \mu\,\sigma_B\,T_s^4 \qquad (3.3.4.1.6)$$

where:

μ - surface emissivity
T_s - surface temperature

The two last terms in Equation 3.3.4.1.1 reflect the influence of turbulent heat exchange. We propose to use the simple bulk formulae defining the turbulent fluxes as proportional to difference between air temperature and specific humidity (g) at two levels:

$$Q_t = K_t\,(T_a - T_s) \qquad (3.3.4.1.7)$$

$$Q_e = K_e\,(g_a - g_s) \qquad (3.3.4.1.8)$$

where:

K_t, K_e - coefficients of proportionality
g_a – specific humidity of air at 2 meters
g_s – specific humidity of saturation at ice surface

The specific humidity is computed as:

$$g_a = 0.62197 * P_V / (P – (0.37803 * P_V)) \quad (3.3.4.1.9)$$

$$g_s = 0.62197 * P_{VI} / (P – (0.37803 * P_{VI})) \quad (3.3.4.1.10)$$

where:

$$P_{VI} = 6.112 * 10. ** (9.5 * T_{DI}(\text{Celsius}) / (265.5 + T_{DI}(\text{Celsius})))$$

is the vapor pressure (mbar) at saturation, and:

$$T_{DI}(\text{Celsius}) = 1. / (1./T_S – 1.846E\text{-}4 * \ln(0.8)) – 273.16$$

is the dew point temperature at saturation, and P is the surface pressure (mbar).

These simple formulae can give us reliable results of determining turbulent fluxes only in the case when the coefficients of proportionality are defined as functions of influencing factors.

We assume the following form for K_t and K_e:

$$K_t = \rho_a C_a C_t V \quad (3.3.4.1.11)$$

$$K_e = \rho_a L_a C_e V \quad (3.3.4.1.12)$$

where:
ρ_a – air density (kg/m^3)
C_a – specific heat (J/kg/K)
L_a – latent heat of evaporation (J/kg)
V - wind velocity (m/s)
C_t, C_e - dimensionless coefficients of proportionality

C_a and L_a will be pre-set constants, stored in the Ice Age LUT. C_t and C_e are equal but depend upon atmospheric stratification. The magnitudes of these coefficients are approximately the same for unstable stratification in the lower levels of the atmosphere and for neutral stratification. For average conditions in polar regions, the magnitude of the dimensionless coefficients is 0.0017. The values for C_t and C_e are stored in the Ice Age LUT. The air density is derived from the surface air temperature and surface

pressure. The resultant heat flux from the atmosphere to the ice (snow) surface can be determined as:

$$Q_s = \lambda \frac{\partial T}{\partial Z} \qquad (3.3.4.1.13)$$

where λ is the thermal conductivity (W/m/K) of ice (or snow).

The heat flux through ice cover depends on ice thickness. This circumstance allows us to calculate ice thickness, assuming that the other components of the heat exchange between the atmosphere and underlying surface are known or can be approximated.

We intend to use the algorithm to calculate the thickness of New, Young, and First Year ice types. For these types, the ice is sufficiently thin to allow a linear approximation of the vertical ice temperature profile. In that case, the heat flux through ice cover can be determining on the basis of the following approximation of Equation 3.3.4.1.13:

$$Q_s = \lambda_i \frac{T_s - \theta}{H} \qquad (3.3.4.1.14)$$

where:

λ_i - thermal conductivity of ice
θ - freezing temperature of water
H - ice thickness (m).

The thermal conductivity of snow differs from ice. If ice is covered by snow, we must modify Equation 3.3.5.1.14 to account for the heat flux through the snow cover:

$$Q_s = \frac{T_s - \theta}{\frac{h}{\lambda_s} + \frac{H}{\lambda_i}} \qquad (3.3.4.1.15)$$

where:

h - snow depth (m),
λ_s - thermal conductivity of snow.

If we assume that all components in the right side of the Equation 3.3.4.1.1 are known, we can replace the left side of Equation 3.3.4.1.1 with 3.3.4.1.14 or 3.3.4.1.15, and express the ice thickness as:

$$H = \frac{\lambda_i (T_s - \theta)}{Q_\Sigma (1 - \alpha) + E_a - E_s + Q_t + Q_e} - \frac{\lambda_i h}{\lambda_s} \qquad (3.3.4.1.16)$$

The algorithm acquires snow depth (h), as a function of ice thickness (H), from the Snow Depth/Ice Thickness LUT, which is created by combining characteristic climatic rates of ice growth and snowfall (c.f. section 3.3.4.1.1)

Our approach uses an ice thickness threshold of 30 cm. Snow depth at the threshold ice thickness is computed by solving equation 3.3.5.1.16 with H = 30 cm. If the computed snow depth is greater than the climatological snow depth for H = 30 cm, we infer that the actual ice thickness is greater than 30 cm, and classify the ice as First Year or Multi-year. If the computed snow depth is smaller than the climatological snow depth for H = 30 cm, we infer that the actual ice thickness is less than 30 cm, and classify the ice as New or Young.

It should be noted that the algorithm for the NPOESS Net Heat Flux EDR (AER, 2004) derives equivalent energy flux components, using a similar theoretical basis. It is recommended that the Net Heat Flux and Sea Ice algorithms be reviewed to identify possible synergies and redundancies.

3.3.4.1.1 Analytical Snow Depth/Ice Thickness LUT

The calculations of ice thickness are very sensitive to the depth of snow, because of the relatively low thermal conductivity of snow. Therefore, it is necessary to get accurate estimates of snow depth. The snow accumulation on ice is a function of time interval that has elapsed since the beginning of ice formation.

Unfortunately, comparative analysis of ice growth and snow accumulation on the basis of direct systematic observations is possible only for the period on initial ice formation in the fall. The information on ice growth for all other times in the seasonal cycle should be modeled.

Ice growth depends mostly on air temperature and snow depth. Ice thickness can be calculated if surface air temperature and solid precipitation are known. Such calculations establish a relationship between snow depth and ice thickness that we can use to create a Snow Depth/Ice Thickness LUT.

Available models of ice growth replace surface temperature by air temperature assuming that the replacement of the temperature does not lead to essential errors in ice thickness calculations. But in our algorithm, the difference between air temperature and surface temperature can not be ignored as the consideration of this difference is used to retrieve ice thickness. Therefore, we need to develop the model of ice growth based on air temperature and include surface temperature as an unknown parameter of the model.

Our approach to derivation of ice thickness is based on using the equation of surface heat balance in the following general form:

$$Q_s = Q_\Sigma(1-\alpha) + E_a - E_s + Q_t + Q_e \qquad (3.3.4.1.17)$$

The vertical heat flux through snow can be determined as:

$$Q = \lambda_s \frac{\partial T}{\partial Z} \quad (3.3.4.1.18)$$

where λ_s is the thermal conductivity of snow.

A similar equation is also applicable to determine the vertical heat flux through ice:

$$Q_i = \lambda_i \frac{\partial T}{\partial Z} \quad (3.3.4.1.19)$$

where λ_i is the thermal conductivity of ice.

Heat flux related to ice growth could be calculated on the basis of the following equation:

$$Q_H = -l\rho \frac{dH}{dt} \quad (3.3.4.1.20)$$

where l is a specific heat of ice formation and ρ is the ice density.

In the case of stationary processes, the surface heat balance is equal to vertical heat flux through snow (ice) and is compensated by ice growth at the undersurface of ice cover. It means that all four fluxes in the last four equations are equal.

For New, Young, and to a certain degree, First Year ice types, the ice is sufficiently thin to allow a linear approximation of the vertical ice temperature profiles. In that case, the heat fluxes through snow and ice could be determining on the basis of the following approximations:

$$Q = \lambda_s \frac{T_s - T_0}{h} \quad (3.3.4.1.21)$$

$$Q_i = \lambda_i \frac{T_0 - \theta}{H} \quad (3.3.4.1.22)$$

where:

T_0 is the temperature at the interface between snow and ice
θ - freezing temperature of water
h – snow depth

H - ice thickness.

The temperature at the boundary between snow and ice is not known. After its elimination from the last two equations, we determine the heat flux through snow and ice as a function of surface temperature and known temperature of ocean water freezing

$$Q = \frac{T_s - \theta}{\frac{h}{\lambda_s} + \frac{H}{\lambda_i}} \qquad (3.3.4.1.23)$$

Surface temperature is a very important parameter in our algorithm. But there are no systematic observations on surface temperature that could be used to create climatic Snow Depth / Ice Thickness LUT. Therefore we need to eliminate surface temperature from consideration. It could be achieved when we consider equality between the last equation of heat flux and surface balance:

$$\frac{T_s - \theta}{\frac{h}{\lambda_s} + \frac{H}{\lambda_i}} = Q_\Sigma(1-\alpha) + E_a - E_s + Q_t + Q_e \qquad (3.3.4.1.24)$$

The members of the right part of this equation are functions of surface temperature, air temperature, and several supposedly known parameters of the lower surface atmosphere layer.

Heat flux due to evaporation is not significant at the low temperatures of ice growth season, turbulent heat flux is proportional to the difference between air and surface temperatures, and long-wave radiation fluxes could be approximated as linear functions of temperatures with great accuracy.

As a result of these described features, the surface heat balance in the last equation could be presented as a linear function of surface and air temperature

$$\frac{T_s - \theta}{\frac{h}{\lambda_s} + \frac{H}{\lambda_i}} = aT_a + bT_S + c \qquad (3.3.4.1.25)$$

After finding T_S from this equation, we can express vertical flux as a function of air temperature, snow depth and ice thickness.

$$Q = \frac{1}{(1 - b(\frac{h}{\lambda_s} + \frac{H}{\lambda_i}))}(aT_a + b\theta + c) \quad (3.3.4.1.26)$$

This vertical heat flux through ice is compensated by ice growth at the undersurface of ice cover:

$$\frac{1}{(1 - b(\frac{h}{\lambda_s} + \frac{H}{\lambda_i}))}(aT_a + b\theta + c) \quad = -l\rho\frac{dH}{dt} \quad (3.3.4.1.27)$$

This relatively simple equation can be used to get reliable calculations of thin ice growth even if thermodynamic parameters of snow and ice are constant.

The snow depth in the equation is assumed to be proportional to time – uniform climatic rate of snow accumulation for relatively short period of young ice growth:

$h = gt.$ (3.3.4.1.28)

If t is considered as a function of H, then the equation presents a linear differential equation of first order

$t' + pt = q(H) = AH + B$ (3.3.4.1.29)

where:

$$p = -\frac{l\rho bg}{\lambda_s(aT_a + b\theta + c)} \quad (3.3.4.1.30)$$

$$q = \frac{l\rho(\frac{b}{\lambda i}H - 1)}{(aT_a + b\theta + c)} \quad (3.3.4.1.31)$$

The solution of equation 3.3.4.1.29 is sought in the form

$t = u(H) * v(H)$ (3.3.4.1.32)

where v satisfies:

$$\frac{dv}{dH} + pv = 0 \quad (3.3.4.1.33)$$

and *u* is found from:

$$v\frac{du}{dH} = q(H) \qquad (3.3.4.1.34)$$

The solution of equation 3.3.4.1.33 is:

$$v = exp(-pH) \qquad (3.3.4.1.35)$$

Taking into account this solution the following equation

$$exp(-pH)\ \frac{du}{dH} = q(H) = AH + B \qquad (3.3.4.1.36)$$

is integrated:

$$u = \int (AH + B)e^{pH} dH = \frac{e^{pH}}{p^2}[(AH + B)p - A] + C \qquad (3.3.4.1.37)$$

The sought solution will be:

$$t = \frac{(AH + B)p - A}{p^2} + Ce^{-pH} \qquad (3.3.4.1.38)$$

The constant of integration will be found on the basis of the assumption that *H=0* for *t=0.*

Then the final solution of our main equation will be presented in the following form:

$$t = \frac{1}{p^2}[(A - pB)e^{-pH} + (AH + B)p - A] \qquad (3.3.4.1.39)$$

This equation, defining ice growth as a function of air temperature, snow accumulation, and prescribed thermodynamic parameters of snow, ice, and freezing water, is our basis to create a Snow Depth / Ice Thickness LUT that contains predicted snow depth.

3.3.4.2 Reflectance Threshold Method

Stage of ice development (ice age) can be considered as a thermodynamic characteristic of ice, reflecting its growth. One of the most prominent features of different stages of ice development is ice color (albedo or reflectance).

New ice is characterized by dark, mat, whitish color, young ice is gray and gray-white. First Year and Multi-year ice has higher reflectance (albedo). New ice and nilas as well as gray ice have a wet surface. Snow cover does not accumulate on these types of ice and does not modify their reflectance. Snow cover can be observed on gray-white ice, but this type of young ice still has lower reflectance than thicker ice. Thus, by definition, different stages of ice development are characterized by different reflectance (c.f. Table 11). This difference is used for discrimination between New/Yong and First Year/Multi-year ice types at daytime. Using the reflectance of visible (I1) and near-infrared (I2) bands is an effective and straightforward way to retrieve ice type for relatively thin ice cover.

This approach will complement the energy balance method, allowing us to meet Measurement Range objectives during daytime as well as night.

TOA reflectance for a range of snow depths, ice thickness, atmospheric conditions, and solar/viewing angles are pre-computed and stored in an Ice Reflectance LUT (c.f. Section 3.3.1.3).

For each band, we select the ice thickness (H) which matches the observed ice TOA reflectance for that band, using a model for the snow depth obtained from the Snow Depth / Ice Thickness LUT. This LUT is developed from climatological models for ice growth and snowfall, (c.f. Section 3.3.4.1.1).

Our approach uses an ice thickness threshold of 30 cm.

3.3.5 Archived Algorithm Output

Sea ice concentration will be written to an Ice Concentration Retained IP file. A file description can be found in the Ice Concentration Detailed Design Document *[Y-3235].*

3.3.6 Algorithm Watch List

Following its review of the Version 3 ATBDs, the VIIRS Operational Algorithm Team (VOAT) has produced a list of items requiring attention. One of these, item 8, directly affects the Sea Ice Characterization EDR:

> 8) *IMPACT OF CLOUD MASK – "Impact of Cloud Mask (clear, cloudy, aerosol distinction) for EDR production and performance."*

In our response to the watch list, we stated that "Raytheon agrees that the interplay between the Cloud mask and the rest of the VIIRS system is a central issue leading into CDR. Within the scope of Phase II, Raytheon will further refine the definitions of 'probably cloudy' and 'probably clear'."

We recognize that effective cloud masking is essential to the production of a global operational sea ice product from Vis-IR data. We have addressed this matter in Section 4.2.3. We are sensitive to the concern in the user community that very aggressive cloud masking can result in the unnecessary exclusion of useful surface data observable through thin clouds. We have been working with the VIIRS Cloud Integrated Product Team (IPT) to provide a Cloud Mask IP that will enable us to process and report the Sea Ice Characterization EDR for surfaces observable through thin cloud cover. Our plan is to identify three regions in the "Cloud Optical Thickness" phase space. In the "Green" region (small τ), the EDR will be reported to meet or exceed specification. In the "Red" region (large τ), the pixel will be masked and the EDR will not be reported. We plan to define a "Yellow" transition region, where the EDR will be reported with a quality warning attached. In this region, we expect the EDR performance to be degraded below specification, but still to provide useful information. The thresholds are TBD, and will require validation with MODIS data. We note that it is important to mask and exclude "Red" region pixels, as our algorithms use search windows.

We will continue to work with the Cloud IPT and the VOAT to ensure that the VIIRS Cloud Mask algorithm provides a product of sufficient quality for us to meet our specification for the Sea Ice Characterization EDR.

4.0 EDR PERFORMANCE AND VALIDATION

4.1 PERFORMANCE ANALYSIS

The performance of the algorithms with respect to the VIIRS requirements and the System Specification is reviewed in this section.

EDR performance shall be verified by analysis, modeling, and/or simulation based on the instrument design and performance characteristics and the algorithms. The analysis, modeling, and/or simulation shall be sufficiently extensive in scope to verify that EDR requirements are met under a broad range of conditions that are representative of those occurring in nature, include typical and extreme conditions.

4.1.1 Ice Concentration

We identified the following stratifications for ice concentration:

1) Ice concentration “truth”
2) Ice “type”
3) Day/Night
4) Viewing angle

Performance of the ice concentration algorithm is expected to depend on ice concentration “truth”. A sensible stratification must then include ice concentration “truth” as a parameter. We have selected 4 ranges of ice concentration, 0.0-0.35, 0.35-0.65, 0.65-0.85, and 0.85-1.0. These ranges correspond to the following ice concentration zones: very open floating ice, open floating ice, close floating ice, very close floating ice.

Ice conditions are widely variable, depending on its stage of development. The contrast between ice and water tie points is generally larger for ice in later stages of development. Algorithm performance is very sensitive to tie point contrast. Analytically, the error in concentration derived from a tie point equation scales inversely with the tie point contrast. A sensible stratification should include ice “type” as a parameter. We have selected 2 ice types, “Young”, and “First-Year or Older”. Young ice is characterized by a thickness of 0.1 – 0.3 meters. We select 0.3 meters as our boundary between ice types. We include a third stratification by type, which we call “Typical Scene”, to illustrate expected performance for a typical probability of ice types.

We specify performance at nadir and at edge of scan.

We report performance estimates for a representative sample of geophysical conditions:

Case 1: Clear, Nadir, Day (Solar Zenith Angle = 60 degrees)
Case 2: Clear, Nadir, Night, Air Temperature = -5 degrees Celsius
Case 3: Clear, Nadir, Night, Air Temperature = -10 degrees Celsius

Daytime performance will depend on solar zenith angle, as surface reflectance errors increase with decreasing sunlight and increased atmospheric path length. We have modeled surface reflectance error for a solar zenith angle of 60 degrees to represent a typical daytime solar elevation in the Great Lakes region during the winter-spring ice season.

Nighttime performance will depend on the surface air temperature. The thermal contrast between ice and open water increases as air temperature decreases. For an air temperature of 0 Celsius, the thermal contrast between most first year ice types and water is negligible. For an air temperature of –5 Celsius, the thermal contrast between most first year ice types and water is 3 – 4 degrees. For air temperatures colder than –10 Celsius, the thermal contrast between most first year ice types and water is greater than 8 – 10 degrees. We have selected two cases of nighttime air temperature (-5 Celsius and –10 Celsius) to illustrate the relative effect on performance. We have found that performance at colder temperatures is similar to the performance at –10 Celsius.

Ice Concentration is derived by a tie point equation:

$$C = (P-W) / (I-W) \qquad (4.1.1.1)$$

Where:

P = measured parameter (either surface temperature or surface reflectance)
W = water parameter value (tie point)
I = ice parameter value (tie point)

Errors in P, W, and I contribute to the measurement uncertainty:

$$\sigma^2_C = (\sigma^2_P + C^2 \sigma^2_I + (1-C)^2 \sigma^2_w) / (I-W)^2 \qquad (4.1.1.2)$$

Errors in P are derived from sensor and algorithm, and are taken from the stratified performances of the Surface Reflectance and Surface Temperature IPs. These were documented in the VIIRS System Specification *[SS 154640-001]* and in the VIIRS Imagery Technical Interchange Meeting (TIM) *[Y4963]*. Precision and accuracy errors were applied to our test data sets.

I and W are derived from a scene, using search windows. Errors in I and W, caused by deviations of the derived ice and water tie points from the “true” pixel tie points, have been an obstacle to achieving global operational ice concentration retrieval. Our algorithm greatly reduces these errors by deriving tie points from the scene.

Our analysis of ice concentration measurement uncertainty was performed as follows:

We applied our algorithm to MODIS Airborne Simulator (MAS) scenes at a 50 meter pixel resolution. The test scenes are discussed in the VIIRS Test Data Set Specification Document. Reflectances in MAS band 3 (648 nm) and 7 (866 nm) were calculated from the top of atmosphere (TOA) radiances. Brightness temperatures in MAS bands 45 (11

μm) and 46 (12 μm) were calculated from the TOA radiances. Surface temperature was computed by the Surface Temperature IP algorithm *[D43761].* The surface reflectances and surface temperature at 50 meter resolution were used as input data for our algorithm. The retrieved ice concentration was adopted as “truth”. The 50 meter truth was aggregated to a VIIRS pixel size at nadir (8 x 8 aggregation to 0.4 km pixels) and adopted as VIIRS “true” concentration at nadir. An additional 16 x 16 aggregation was made to obtain VIIRS “true” concentration at 0.8 km (edge of scan).

A model modulation transfer function (MTF) with HSR = 0.4 km was then applied to the surface reflectance and surface temperature images to simulate VIIRS imagery at nadir. An additional MTF with HSR = 0.8 km was applied to simulate the edge of scan imagery.

We then perturbed the MTF-smeared reflectances, using our model errors for the Surface Reflectance IP in VIIRS band I1 (640 nm), which is the daytime visible (DV) imagery band. The errors depend on surface reflectance truth, which is correlated with ice concentration. Accuracy and precision errors were applied. Accuracy errors include a 2% calibration bias and an aerosol optical thickness bias of 0.05. Precision errors are derived from the sensor noise. Reflectance errors were calculated for a solar zenith angle of 60 degrees. We note that VIIRS band I2 (865 nm) is also available as a performance enhancement band. The daytime performance reported here is from the 640 nm VIIRS band only.

We perturbed the aggregated temperatures, using model errors for the Surface Temperature IP. Surface Temperature IP performance was derived as follows:

The split-window Ice Surface Temperature algorithm was applied to MODIS Airborne Simulator (MAS) scenes at a 50 meter pixel resolution. Brightness temperatures in MAS bands 45 (11 μm) and 46 (12 μm) were calculated from the unperturbed TOA radiances in those bands, and used as input data to the algorithm. The retrieved surface temperatures were adopted as “truth”. The 50 meter truth was aggregated to VIIRS imagery pixel sizes at nadir (8 x 8 aggregation to 0.4 km pixels). The aggregated temperatures were adopted as VIIRS “truth”. The MAS TOA radiances were then aggregated to VIIRS pixel size. A proxy for the VIIRS Long-Wave Infrared (LWIR) imagery band radiance was made from the average of the band 45 and 46 radiances. The VIIRS model radiances were then perturbed by our models for sensor noise and calibration bias. A 0.5% calibration bias was applied to all radiances. Sensor noise models for VIIRS bands M15 (11 μm), M16 (12 μm), and I5 (11.45 μm) were applied to the corresponding radiances. The perturbed radiances were converted to brightness temperature, and used as input data to the Surface Temperature IP algorithm. Surface Temperature IP accuracy, precision, and uncertainty errors were calculated from comparison of the retrieved surface temperature to the “truth”. At nadir, these errors are 0.278 K in accuracy and 0.378 K in precision. At edge of scan, the precision error is 0.508 K.

We applied the algorithm to the perturbed VIIRS scenes to retrieve ice concentration, and computed measurement uncertainty by comparing the retrieved concentration to

the “VIIRS truth”. The pixel deviations between retrieved and true concentration were aggregated 2 x 2 to a horizontal cell of 0.8 km to represent a VIIRS nadir retrieval. The aggregated deviations were sorted into the four truth stratification bins. For each bin, the RMS of the deviations was computed as the measurement uncertainty for that bin. We did this for three sea ice daytime scenes (A Bering Sea scene in early April (AK_74_14) from the Alaska-April 95 campaign and two Beaufort Sea scenes in late May (ACE_65_3 and ACE_65_8) from the First International Satellite Cloud Climatology Project (ISCCP) Regional Experiment–Arctic Cloud Experiment (FIRE-ACE) campaign) and for a lake ice daytime scene (a Lake Superior scene in February (WIN_46_16) from the WINCE campaign. An example of the procedure is illustrated for scene ACE_65_3 in Figure 10.

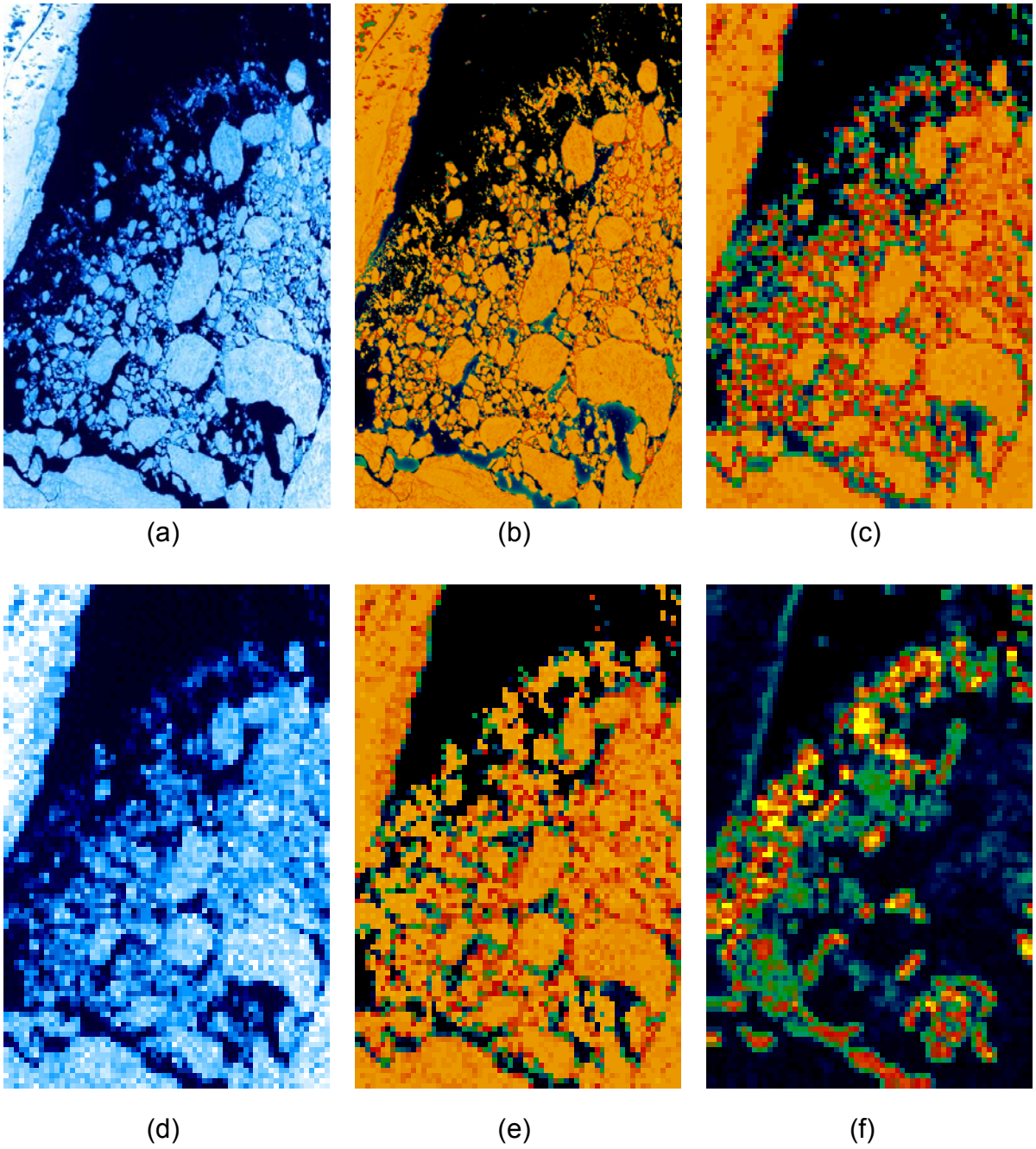

Figure 10. Illustration of Ice Concentration performance analysis methodology.

The scene in Figure 10 is from the FIRE-ACE campaign of the MODIS Airborne Simulator (ACE_65_3). The original MAS scene (a), is used as input to the ice concentration algorithm, which derives ice concentration at the 50 meter MAS resolution (b). The concentration is aggregated to the VIIRS pixel size of 0.4 km to produce VIIRS truth (c). Scene (a) is then perturbed by our model for the sensor effects to simulate

expected VIIRS imagery at nadir (d). Scene (d) is used as input to the ice concentration algorithm, which derives the simulated VIIRS ice concentration (e). A comparison of result (e) with truth (c) produces an error estimate (f).
For daytime performance analysis, we use the reflectance data. For nighttime performance analysis, we use the surface temperature data, adjusted to simulate conditions when air temperature is –5 Celsius and –10 Celsius. The adjustment is necessary, because the nighttime thermal contrast between ice and water scales linearly with the thermal contrast between air and water:

$$T_W - T_I = 16.2\ H\ (3.61 + 0.049\ T_W + (T_W - T_A)) / (1.5 + 17\ H) \qquad (4.1.1.3)$$

Where: T_W = Water Temperature (Celsius)

T_I = Ice Temperature (Celsius)

T_A = Air Temperature (Celsius)

H = Ice Thickness (meters)

Equation 4.1.1.3 is derived from energy balance, and is approximately correct for ice thickness less than 1 meter and for typical nighttime conditions.

An illustration of the process is shown as Figure 11. The MAS scene AK_74_14 was processed to create simulated nighttime surface temperature imagery for conditions where surface air temperature = 0^0 Celsius, -5^0 Celsius, -10^0 Celsius, and -20^0 Celsius.

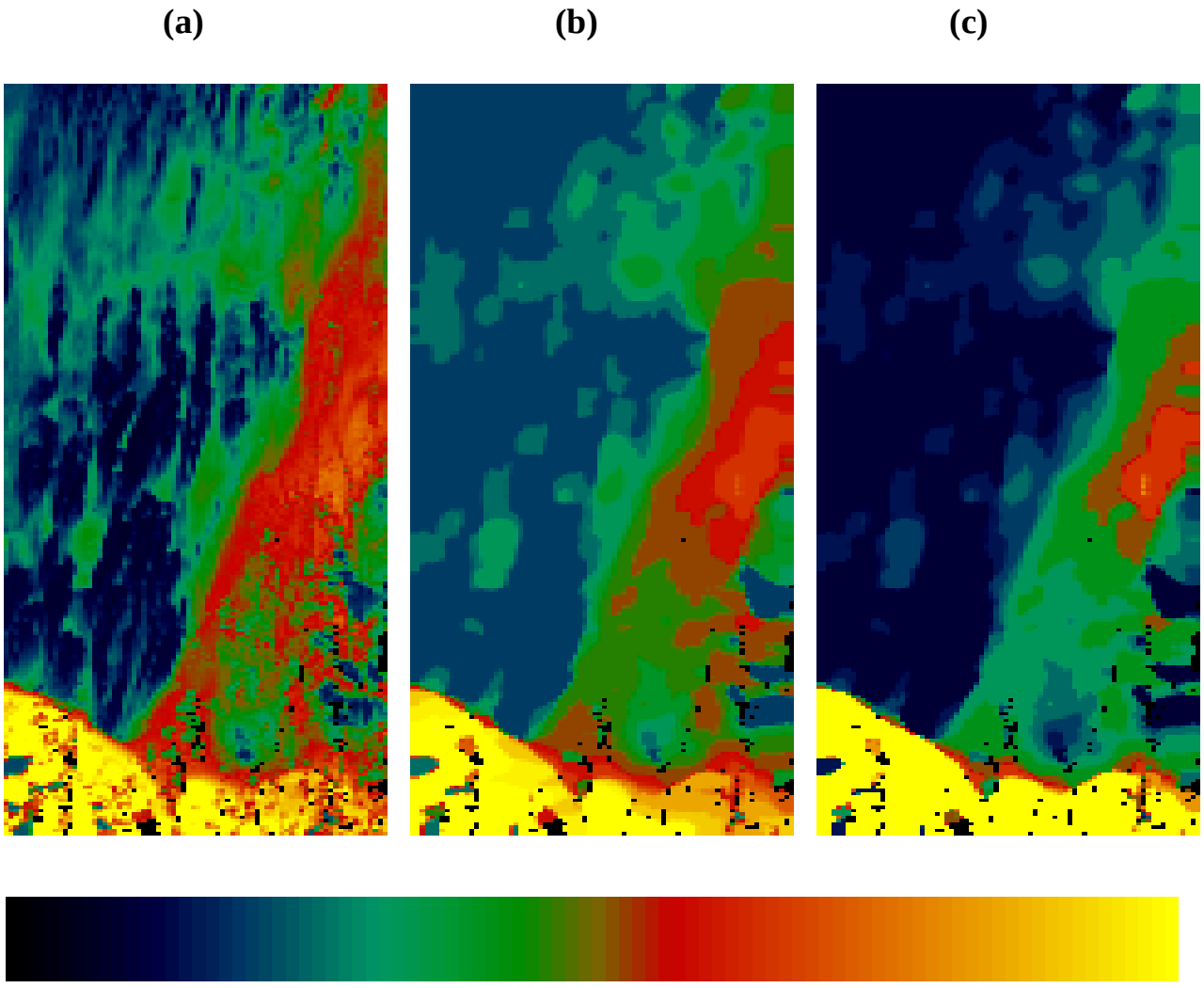

Figure 11. Ice Reflectance tie point retrieval for the Bering Sea scene AK_74_14.

Figure 11(a) shows the simulated VIIRS daytime visible band imagery. Figure 21(b) shows the retrieved tie points. Figure 11(c) shows the derived ice thickness. The color table displays a reflectance range of 0.0 (blue) to 0.7 (yellow) and a thickness range of 0.0 (blue) to 0.2 meters (yellow). The ice thickness is calculated from a fourth order polynomial thickness-reflectance relation, which was determined empirically by matching temperature and reflectance distributions from a number of ice scenes.

The ice temperature was then calculated from equation 4.1.1.3, for a given air temperature. The surface temperature was computed as:

$$T_S = T_I * C + T_W * (1-C) \qquad (4.1.1.4)$$

Sensor perturbations were added as a precision error of 0.378 K and an accuracy error of 0.278 K. The resulting images are illustrated in Figure 12.

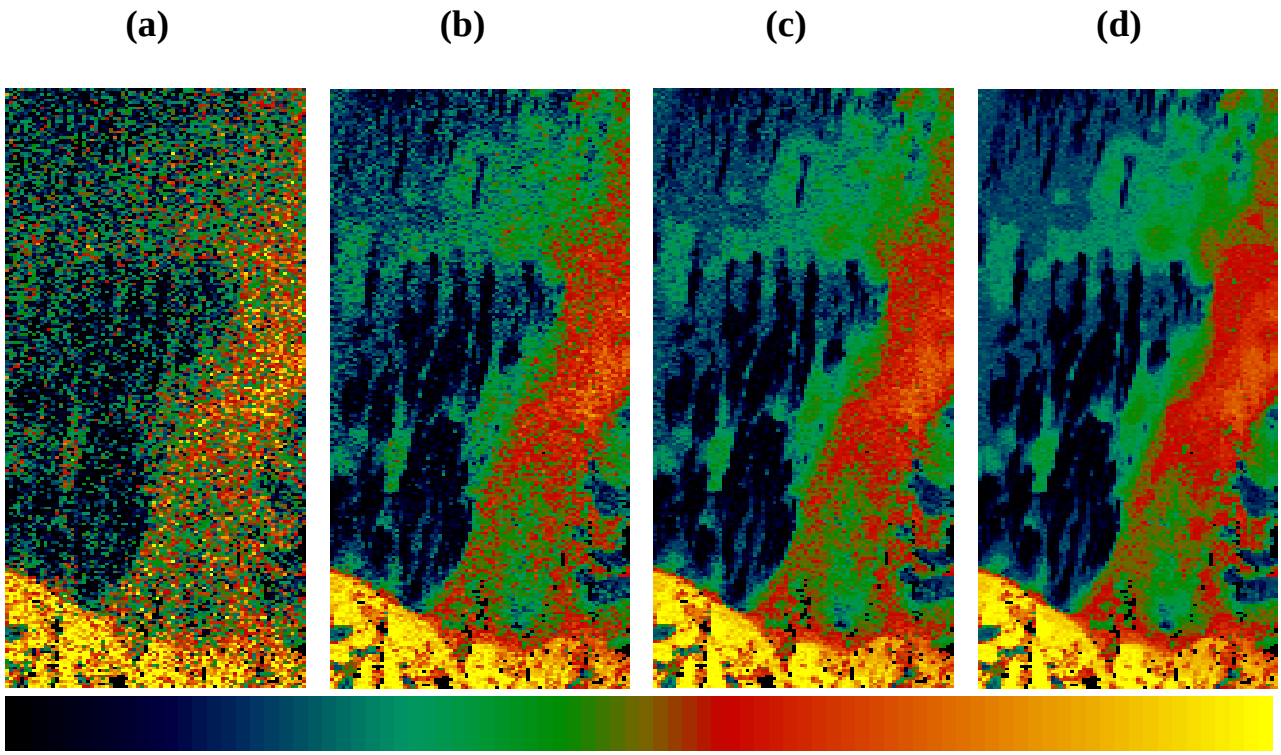

Figure 12. Simulated VIIRS nighttime imagery of the Bering Sea scene AK_74_14

Figure 12 simulations are for air temperatures of 0 degrees Celsius (a), -5 degrees Celsius (b), -10 degrees Celsius (c), and -20 degrees Celsius (d).

Figure 12 shows how lower air temperatures increase the thermal contrast between ice and open water, resulting in smaller ice concentration measurement uncertainty. We will specify nighttime performance for the –5 and –10 cases.

The process was repeated for a fresh water ice scene, the Lake Superior MAS scene WIN_46_16. In this case, the water temperature was set to the fresh water freezing point, ice thickness was calculated, and ice temperatures calculated for air temperatures of 0, -5, -10, and –20 Celsius.

Simulations were performed at for a VIIRS nadir view and for a VIIRS edge of scan view. The simulated thermal imagery is illustrated in Figures 13 (nadir) and 24 (edge of scan).

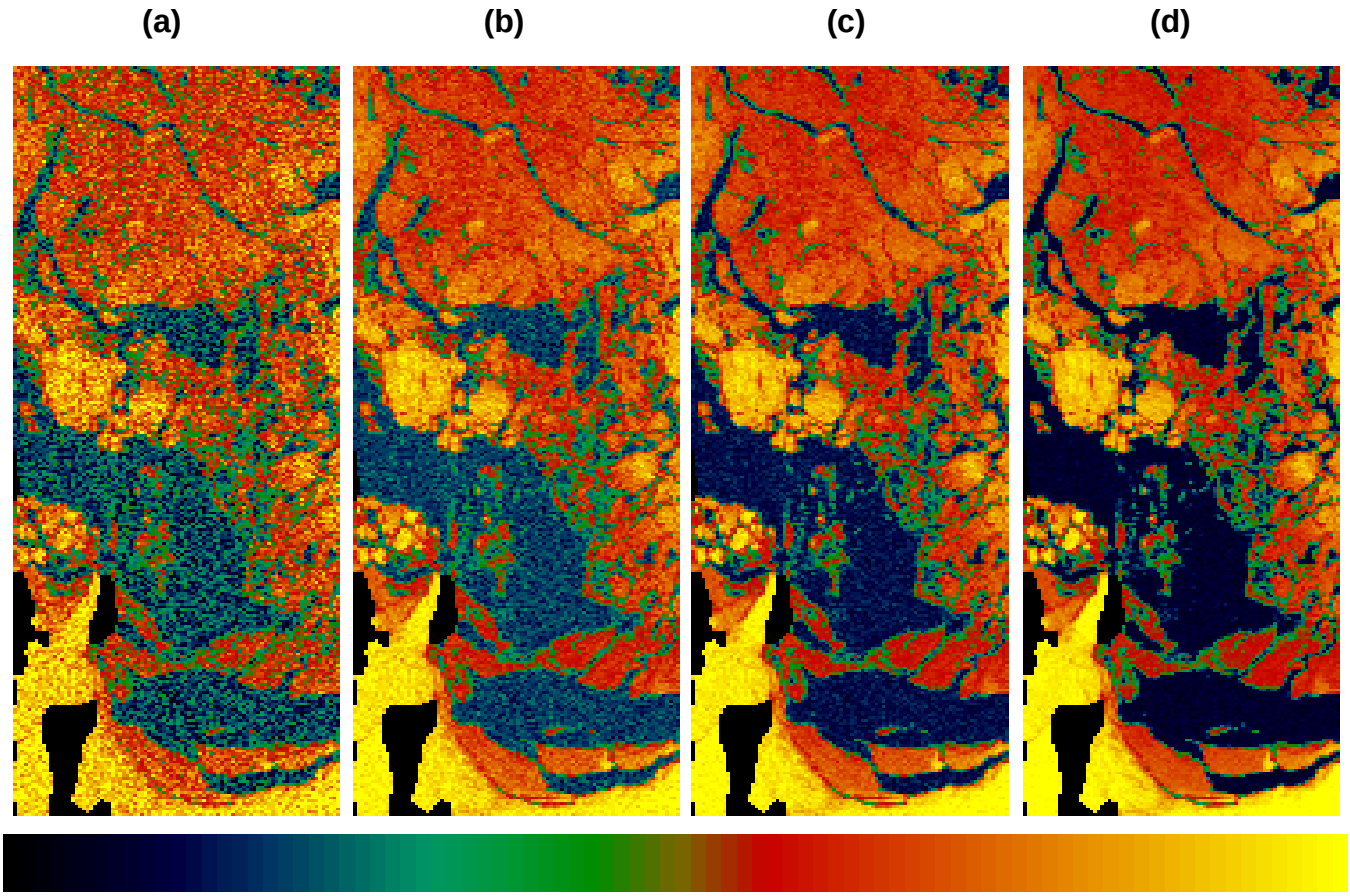

Figure 13. Simulated VIIRS nighttime imagery of Lake Superior (nadir view).

The scene in Figure 13 is the MAS scene WIN_46_16. Figure 13 simulations are for air temperatures of 0 degrees Celsius (a), -5 degrees Celsius (b), -10 degrees Celsius (c), and -20 degrees Celsius (d). The imagery is simulated for a VIIRS nadir view, with Surface Temperature IP system errors added. The black pixels are land masked.

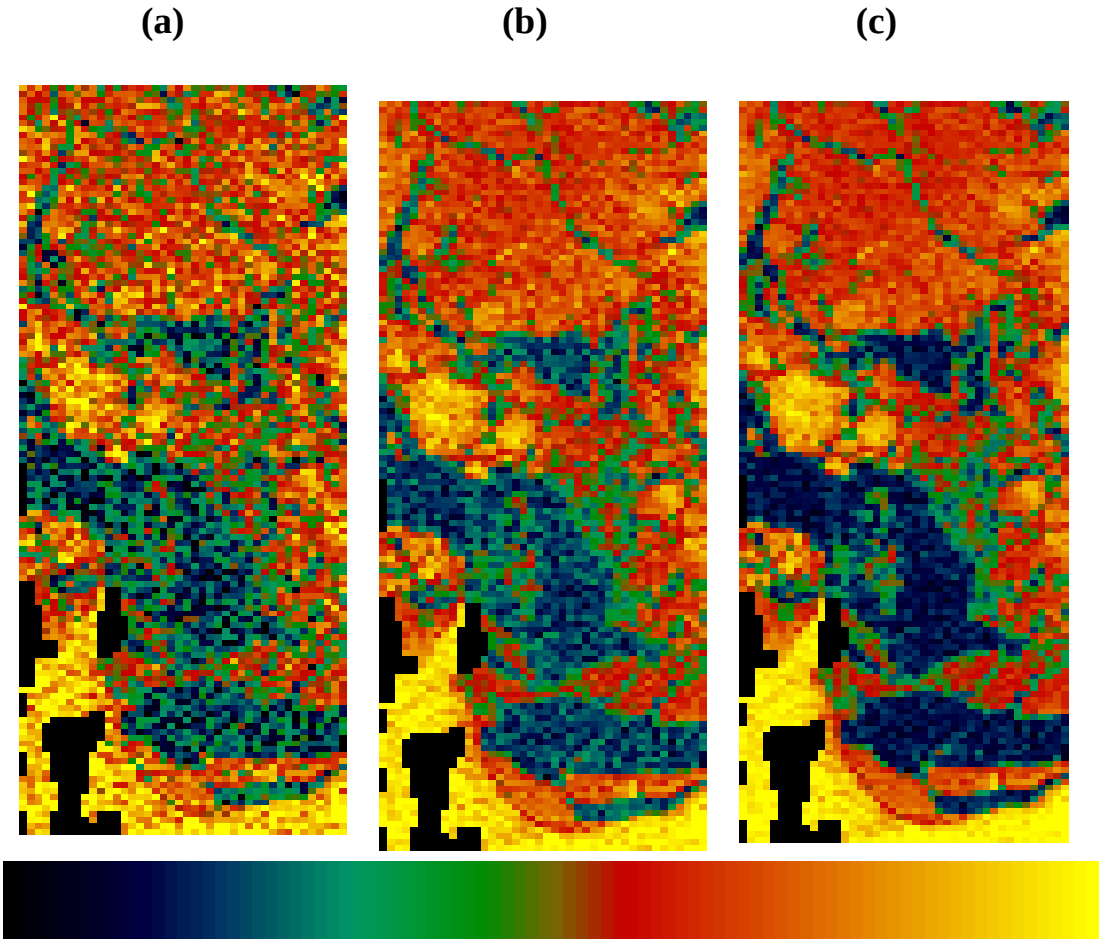

Figure 14. Simulated VIIRS nighttime imagery of Lake Superior (edge of scan)

The scene in Figure 14 is the MAS scene WIN_46_16. Figure 14 simulations are for air temperatures of 0 degrees Celsius (a), -5 degrees Celsius (b), and -10 degrees Celsius (c). The imagery is simulated for a VIIRS edge of scan view, with Surface Temperature IP system errors added. The black pixels are land masked.

Measurement uncertainties were computed from the scenes for each stratification of ice concentration truth. To assign these measurement uncertainties to an ice type bin, the mean tie point difference for each truth bin was computed. The truth / type bin error was then derived as:

$$\sigma_{mn} = \sigma_m \, (I\text{-}W) / (I\text{-}W)_n \qquad (4.1.1.5)$$

where: σ_{mn} = measurement uncertainty for (truth,type) bin (m,n)

σ_m = observed measurement uncertainty for truth bin (m = 1,4)

(I-W) = observed mean difference in ice/water tie points

$(I\text{-}W)_n$ = mean difference in ice/water tie points for ice type (n = 1,2)

and the scaling factor (1 / (I-W)) is based on equation 4.1.1.2.

Tables 6, 7, 8, 9, and 10 show the errors stratified by ice concentration and ice type. The errors are for horizontal cells of 0.8 km at nadir and 3.2 km at edge of scan, under clear conditions. The third row of each table is derived as a weighted mean of the first two rows to represent a typical distribution of lake ice thickness.

Table 6. Ice Concentration Measurement Uncertainty, Case1
(Clear, Nadir, SZA=60 degrees)

Ice Type	Ice Concentration Truth			
	0.00 – 0.35	0.35 – 0.65	0.65 – 0.85	0.85 – 1.00
Young	.0537	.0755	.0769	.0844
First-Year/Multi-Year	.0265	.0373	.0380	.0417
Typical Scene	.0495	.0696	.0709	.0777

Table 7. Ice Concentration Measurement Uncertainty, Case 2
(Clear, Nadir, Night, Air temperature = -5 Celsius)

Ice Type	Ice Concentration Truth			
	0.00 – 0.35	0.35 – 0.65	0.65 – 0.85	0.85 – 1.00
Young	.0359	.0730	.0663	.0662
First-Year/Multi-Year	.0277	.0563	.0511	.0510
Typical Scene	.0344	.0700	.0636	.0635

Table 8. Ice Concentration Measurement Uncertainty, Case 3,
(Clear, Nadir, Night, Air temperature = -10 Celsius)

Ice Type	Ice Concentration Truth			
	0.00 – 0.35	0.35 – 0.65	0.65 – 0.85	0.85 – 1.00
Young	.0331	.0672	.0611	.0610
First-Year/Multi-Year	.0255	.0518	.0471	.0470
Typical Scene	.0317	.0644	.0586	.0585

Table 9. Ice Concentration Measurement Uncertainty, Case 4
(Clear, Edge of Scan, SZA = 60 degrees)

Ice Type	Ice Concentration Truth			
	0.00 – 0.35	0.35 – 0.65	0.65 – 0.85	0.85 – 1.00
Young	.0642	.0996	.0874	.0724
First-Year/Multi-Year	.0317	.0492	.0432	.0358
Typical Scene	.0592	.0917	.0806	.0667

Table 10. Ice Concentration Measurement Uncertainty, Case 5
(Clear, Edge of Scan, Night, Air temperature = -5 Celsius)

Ice Type	Ice Concentration Truth			
	0.00 – 0.35	0.35 – 0.65	0.65 – 0.85	0.85 – 1.00
Young	.0350	.0956	.0707	.0547
First-Year/Multi-Year	.0270	.0737	.0545	.0422
Typical Scene	.0335	.0916	.0678	.0525

It should be noted that the (1/(I-W)) factor in the equation for ice concentration measurement uncertainty is the primary determinant of performance. As the contrast between ice and water (I-W) decreases, errors increase inversely. Our simulations indicate that we do not attain our specification when the thermal contrast between ice and water is less than 2.2 K and the visible reflectance contrast is less than 0.14. The effect of reducing all of our system errors by a factor of 2, for example, would allow us to attain our specification for an additional range of 1.1 K in ice temperature. Performance is limited more by the geophysical conditions of the scene than by the sensor/algorithm limitations.

We identify the following factors as possibly contributing to the total error budget for ice concentration:

- Tie Point errors
- Sensor noise
- Calibration
- MTF
- Band Registration

Tie Point Errors: The real variation in ice and water tie points can not be entirely accounted for with a data set of finite spatial resolution. We model these errors by comparing the retrieval of ice concentration at VIIRS resolution with the retrieval at MAS resolution. We make the reasonable assumption that the tie point errors at a resolution of 50 meters are negligible compared with the errors at a resolution of 0.4 km.

Sensor Noise: Precision error is due to sensor noise and to variations in atmospheric condition on the spatial scale of the VIIRS pixel. Our analysis shows that sensor noise will be the dominant precision error for most cases. We therefore model these errors by

perturbing our “true” reflectances and temperatures by adding sensor noise to the radiances.

Calibration: Our algorithm is not expected to be sensitive to accuracy errors in reflectance and temperature, since the measured parameter, the ice tie point, and the water tie point will all be shifted by the same error. To test this hypothesis, we applied a calibration bias of 2% to the reflectance and 0.5% to the temperature.

MTF: MTF smearing of the radiances will alias real horizontal variability into errors in measured reflectance and/or temperature for a given pixel. We model these errors on our scenes by applying the sensor MTF specification to the images.

Band Registration: Band-to-band registration errors will also alias horizontal variability into measurement error. These errors only apply to a retrieval that uses more than one band. Since our performance analysis is based on single band retrieval, band registration errors were not simulated. If the retrieval were to use more than one band to enhance performance, band registration error must be considered. For now, we note that the current performance analysis can always be achieved with a single band. If a multi-band result is worse, due to the effects of band registration or non-optimum band weighting, we always have the option of using the single band.

An error budget for ice concentration is shown in Table 19. This error budget was determined from our sensitivity analysis, using the VIIRS Sensor Specification and the MAS scene.

Table 11. Error Budget for Ice Concentration

ICE CONCENTRATION **Specification v5 (CDR)**	**Case:** **Measurement Uncertainty (km)**	**Clear, Nadir, SZA = 60 degrees, Truth = 0.85-1.0, Typical Scene** **Reference**
Threshold	TBD	VIIRS SRD
Objective	TBD	VIIRS SRD
System Specification	0.1	Raytheon VIIRS Specification v5
System Performance	0.0777	This document, Section 3.4.2.1
System Margin	0.0630	RSS Difference of Specification and Performance
Algorithm Performance	0.0732	This document, Section 3.4.2.1
Sensor Performance	0.0261	This document, Section 3.4.2.1

Our post-CDR performance analysis consists of a comparison of the MODIS ICEMAP output to the VIIRS Ice Concentration output for a MODIS scene (Figure 15).

The scene is taken from a MODIS Terra observation of the Chukchi Sea/Bering Sea region on March 27, 2001 at 2240 GMT.

The MODIS L1b data was converted into a proxy VIIRS SDR that was input to our algorithm to produce a proxy VIIRS ice concentration output. The proxy output was then compared to the MODIS “truth”, determined from the MODIS ICEMAP swath product (MOD029). Note that the MOD029 product is at the moderate resolution.

The first comparison was made by assigning a concentration of 1.0 to pixels classified as “ice” in the MOD029 product and a concentration of 0.0 to pixels classified as “no ice” in the MOD029 product. We then compared the 2 x 2 aggregated VIIRS concentration to the MOD029 “truth” at moderate resolution. This comparison results in an accuracy error of 0.05 and a Measurement Uncertainty of 0.1215. An illustration of this comparison for a spatial subset of the MODIS scene is shown in Figure 16.

The second comparison was made by comparing the ice concentration for a 5 x 5 aggregation of the moderate resolution “truth” to the 10 x 10 aggregated VIIRS concentration. This comparison results in an accuracy error of 0.05 and a Measurement Uncertainty of 0.1269.

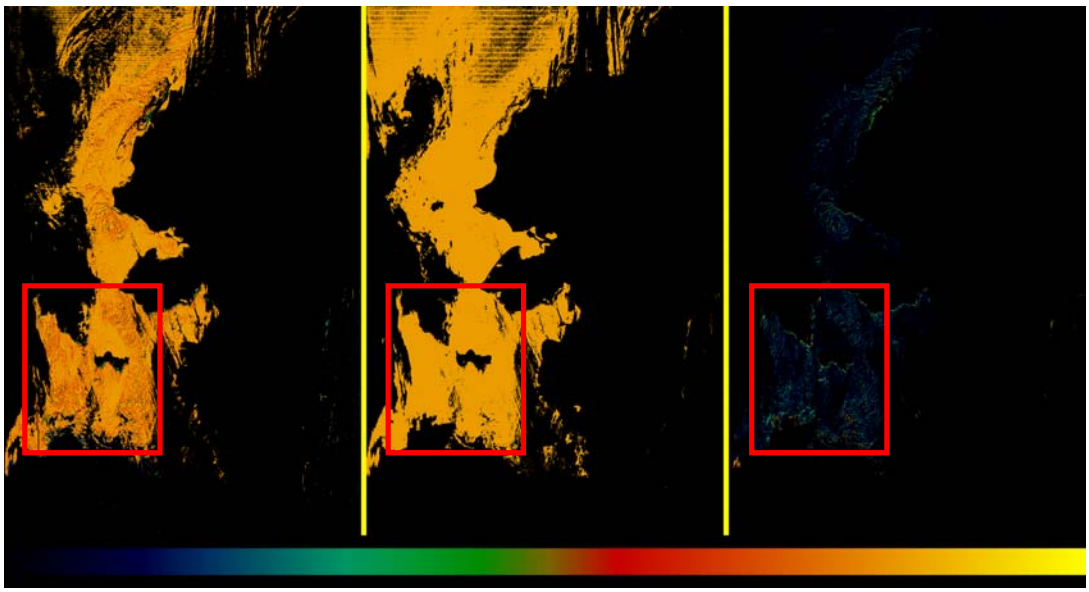

0.0 **1.2**

Figure 15. Ice Concentration Unit Test: Ice_8 Test Scene

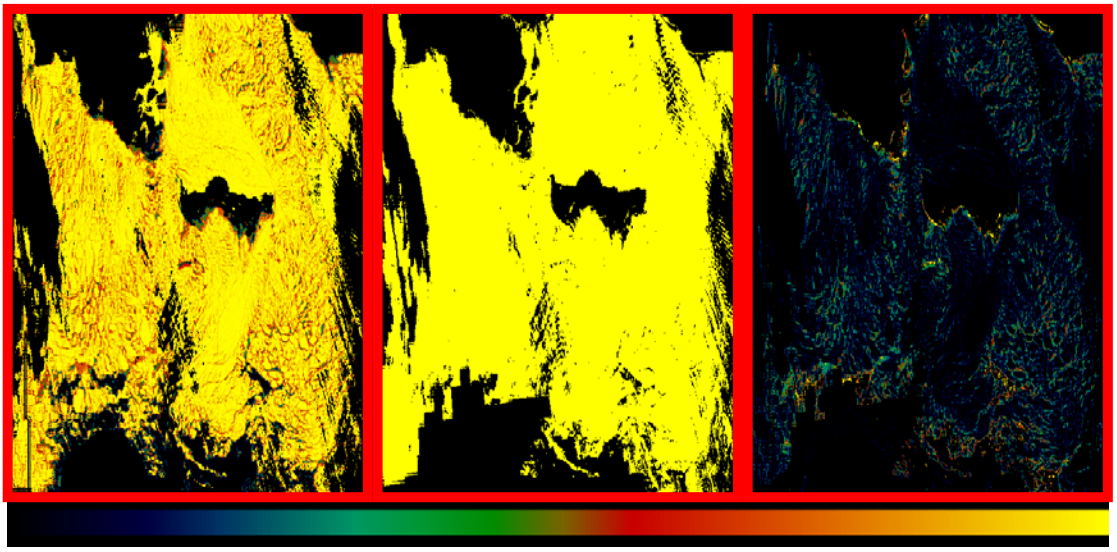

0.0 **1.0**

Figure 16. Ice Concentration Unit Test: Ice_8 Test Sub-Scene

The left image in each of Figures 15 and 16 shows the VIIRS ice concentration output. The middle image shows the MODIS binary map output. The right image shows the difference between the VIIRS ice concentration and the ice concentration from MODIS.

The first two comparisons suffer from the limitation that the MODIS “truth” is a binary product, so the ice concentration derived from the aggregation is an average of zeros

and ones, and therefore suffers from round off error. It is desirable to find a comparison method that does not include this error in the “truth”.

We used an alternative method that turns the VIIRS concentration into an ice/no ice binary map and then compares the VIIRS binary map to the MOD029 product. We found that the fraction of pixels for which the VIIRS map match the MODIS map was 0.986175 (i.e. a “probability of correct typing = 98.6175%). We then perturbed the VIIRS concentration by the accuracy and uncertainty errors derived from the second comparison above, turned the perturbed VIIRS concentration into a perturbed binary map, and compared the perturbed and unperturbed VIIRS binary maps.

We found that the probability of correct typing was 98.93%, somewhat better than the match between the MODIS and unperturbed VIIRS binary maps. This suggests that our error estimates from the second comparison are somewhat lower than they should be. Finally, we perturbed the VIIRS concentration by a range of uncertainty errors, and determined which perturbation resulted in a probability of correct typing equal to the VIIRS/MODIS match. We found that a perturbation with an uncertainty of 0.162 resulted in a probability of correct typing between the VIIRS perturbed/unperturbed maps equal to 98.62%. We therefore determine that the best estimate of measurement uncertainty between the VIIRS ice concentration and the MODIS “truth” is 0.162.

We note that the measurement uncertainty must be stratified according to “truth”. We have run a simulation to estimate the measurement uncertainty binned according to “truth”, using the actual distribution of ice concentration for the scene. Our best estimate for the stratified measurement uncertainty that would produce the observed match between VIIRS and MODIS binary maps is shown in Table 12.

Table 12. Ice Concentration Measurement Uncertainty (MODIS Scene)

Ice Concentration Truth			
0.00 – 0.35	**0.35 – 0.65**	**0.65 – 0.85**	**0.85 – 1.00**
0.139	0.228	0.221	.157

A comparison of Table 12 to Tables 6-10 shows that the error derived from the MODIS scene is substantially larger than the errors obtained from the MAS scene. If we average the daytime/nighttime and nadir/edge of scan MAS errors, we derive the errors shown in Table 13.

Table 13. Ice Concentration Measurement Uncertainty (MAS/MODIS Comparison)

	Ice Concentration Truth			
	0.00 – 0.35	**0.35 – 0.65**	**0.65 – 0.85**	**0.85 – 1.00**
From MODIS scene	0.139	0.228	0.221	0.157
From MAS scene	0.045	0.081	0.071	0.066
RMS Difference	0.131	0.213	0.209	0.143

We see from Table 13 that the residual error (RMS difference between MODIS and MAS) is 2-3 times as large as the error from MAS. Some of this extra error is probably due to the fact that the MAS errors are based on simulated perturbations and therefore do not include any additional error sources that were not simulated. Though we expect these to be minor, we currently cannot verify this. We expect that most of the additional error is due to the error in the MODIS product (i.e. that estimating ice concentration from the MODIS binary map results in larger errors than estimating ice concentration from the VIIRS algorithm. If the MODIS error is 2-3 times as large as the VIIRS error, then the results in Table 13 are consistent and suggest VIIRS errors comparable to the errors obtained from the MAS scene. If, however, VIIRS errors are as large as MODIS errors, the expected VIIRS errors are estimated as the errors from the MODIS scene divided by SQRT(2.) Finally, if the MODIS errors are much smaller than the VIIRS errors, the estimated VIIRS errors are comparable to the errors obtained from the MODIS scene. All of these possibilities are summarized in Table 14.

Table 14. Ice Concentration Measurement Uncertainty (Final Estimates)

	Ice Concentration Truth			
	0.00 – 0.35	**0.35 – 0.65**	**0.65 – 0.85**	**0.85 – 1.00**
From MAS scene	0.045	0.081	0.071	0.066
MODIS error = 3 * VIIRS error	0.044	0.072	0.070	0.050
MODIS error = 2 * VIIRS error	0.062	0.102	0.099	0.070
MODIS error = VIIRS error	0.098	0.161	0.156	0.111
MODIS error = 0	0.139	0.228	0.221	0.157

It is desirable to extend the performance analysis to additional scenes. It is especially desirable to combine the MAS-based and MODIS-based test methods. The MAS-based method has the advantage of accurate high resolution truth, but has the disadvantage that the test data are not from a full swath sensor in Earth orbit. The MODIS-based method has the advantage of providing the full swath Earth orbit test data, but has the disadvantage of not providing reliable truth.

It is recommended that additional performance analysis be conducted, using MODIS data as a source of VIIRS proxy data and using Landsat data as a source of truth. It is our expectation that this analysis will demonstrate that the VIIRS errors are small enough to satisfy Measurement Uncertainty < 0.1 for most stratifications.

4.1.2 Ice Age

The requirement is to classify a cell containing sea ice as one of two types: New/Young, or All other the thicker ice. New/Young ice is separated from other thicker ice by a thickness threshold of 0.3 meters.

Ice concentration “truth” is not included as a stratification parameter. There will be a correlation between ice concentration error and error in the ice condition (reflectance and/or temperature). To the extent that ice concentration error depends on ice concentration “truth” (c.f. Section 4.1.1), there will be a dependence of ice age error on ice concentration “truth”. Identification of this dependence, though desirable, has been deferred to future work.

Classification of New/Young from Energy Balance: We will calculate errors at nadir and edge of scan.

Classification of New/Young from Reflectance: We will calculate errors at nadir and edge of scan.

4.1.2.1 Classification from Energy Balance

All components of the surface energy balance, Equation 3.3.5.1.16, or parameters determining these components, can be directly retrieved from VIIRS, NCEP data. At the present time, we do not have all necessary information, and need to use an alternative approach for verification.

Analysis of the performance of the energy balance algorithm was made as follows:

Ice thickness is derived from the energy balance equation (3.3.5.1.16). Differentiation of equation 3.3.5.1.16 with respect to each contributing error term yields the analytic dependence of the error in H on each error source. At night, the solar radiation term vanishes, leaving us with three major error sources:

T_s – surface temperature
T_a – surface air temperature
h – snow depth

A typical ice growth season in the vicinity of Barrow, Alaska was modeled, with a climatological history of air temperature and snow depth. Ice thickness error is then derived analytically from estimates of error in air temperature, snow depth, and observed surface temperature. From the distribution of ice thickness and ice thickness measurement error, probability of correct classification is calculated.

Ice temperature does not adjust to changes in air temperature immediately. Due to thermal inertia, ice temperature follows changes in air temperature with a lag of 1 to 12 hours, depending on ice thickness. Thus, the most exact mathematical description of

thermal processes in ice cover can be obtained if we combine current ice temperature with average air temperature during the previous 12 hours. This does not degrade algorithm performance.

Performance also depends strongly on the depth of snow cover on the ice, which varies inter-annually. Snow depth for a given horizontal cell depends on the precipitation history over the ice in that cell during its growth. We will acquire the estimated snow depth from a climatologically based LUT, based on characteristic precipitation rates and ice growth rates for a given region and season. We adopt an error in snow depth of 0.5 * truth, based on typical variability of these rates.

Ice surface temperature errors are obtained from the specification and performance of the Surface Temperature IP. The Surface Temperature IP is not a system level requirement and therefore does not have a system specification. Surface Temperature IP performance requirements are this driven by the system specifications for the sea ice and fresh water ice products. Surface temperature IP errors were estimated as follows:

(1) The split-window Ice Surface Temperature algorithm was applied to MODIS Airborne Simulator (MAS) scenes at a 50 meter pixel resolution. Brightness temperatures in MAS bands 45 (11 μm) and 46 (12 μm) were calculated from the unperturbed TOA radiances in those bands, and used as input data to the algorithm. The retrieved surface temperatures were adopted as “truth”. The 50 meter truth was aggregated to VIIRS imagery pixel sizes at nadir (8 x 8 aggregation to 0.4 km pixels). The aggregated temperatures were adopted as VIIRS “truth”.

(2) The MAS TOA radiances were then aggregated to VIIRS pixel size. A proxy for the VIIRS I5 band radiance was made from the average of the band 45 and 46 radiances. The VIIRS model radiances were perturbed according to our models for sensor noise and calibration bias. A 0.5% calibration bias was applied to all radiances. Sensor noise models for VIIRS bands M15 (11 μm), M16 (12 μm), and I5 (11.45 μm) were applied to the corresponding radiances. The perturbed radiances were converted to brightness temperature, and used as input data to the Surface Temperature IP algorithm.

(3) Surface Temperature IP accuracy, precision, and uncertainty errors were calculated from comparison of the retrieved surface temperature to the “truth”. The accuracy error (bias) is 0.278K. The precision error is 0.378 K at nadir and 0.508 K at edge of scan.

It may seem at first glance that this performance is much better than would be expected from the Noise Equivalent Delta Temperature (NEdT) specification for the I5 band (see VIIRS Radiometric Calibration Algorithm Theoretical Basis Document ATBD [D43777]). There are two reasons for this:

1) The NEdT specification for band I5 is at a reference temperature (Ttyp) of 210K. Surface temperatures in regions where we need performance (the marginal ice zones) are ~ 270K, where NEdT is significantly smaller.

2) NEdT performance is better than specification, since our specification includes margin.

NEdT performance for the three thermal bands used by the algorithm is shown in Figure 17.

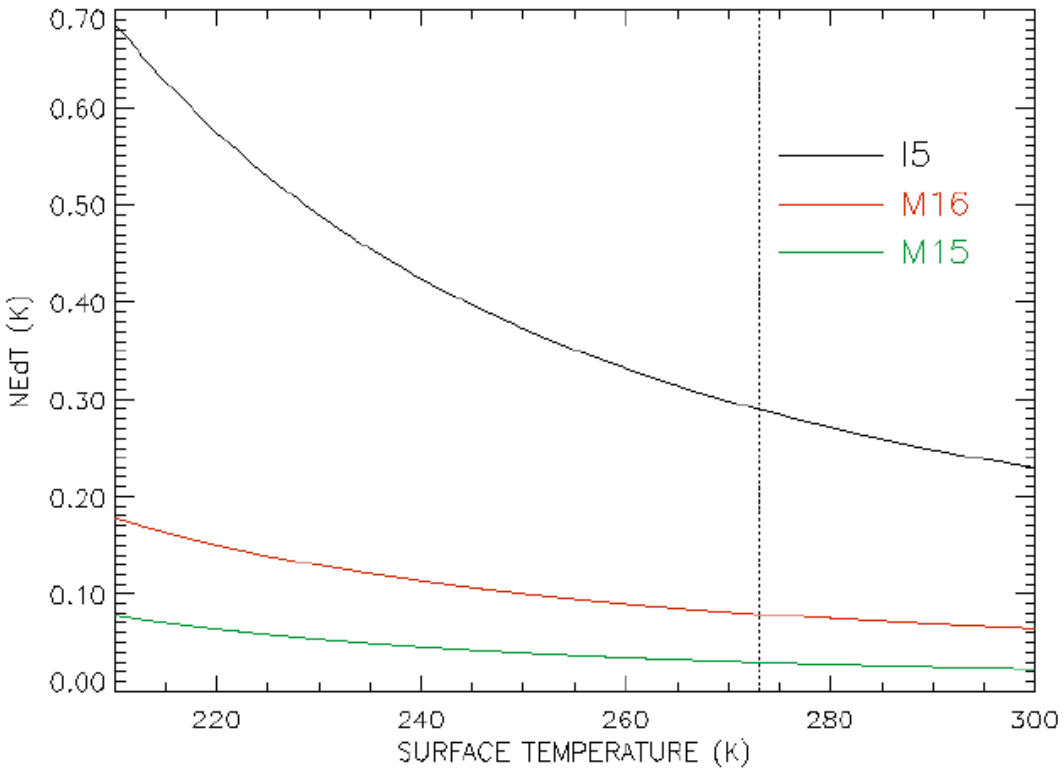

Figure 17. NEdT performance estimates for bands I5, M15, and M16

At the ice/water temperature boundary (~ 273 K, indicated by the vertical dotted line in the figure 17, band I5 NEdT performance is 0.289 K. This is somewhat smaller than our derived precision error (0.378K at nadir). We assume that the additional derived error is due to band misregistration and/or atmospheric variance, and that the error derived from MAS data is still a good estimate of the Surface Temperature IP error in the marginal ice zones.

The accuracy and precision errors are RSS summed to give the total measurement uncertainty errors. They are 0.578 K (performance at edge of scan (EOS)), and 0.469 K (performance at nadir).

Errors in surface air temperature and snow depth are assumed to be independent of scan angle, as these are obtained from external data sources (NCEP or CMIS) that are not related to the current VIIRS swath.

Tables 15, 16, and 17 show the errors stratified by scan angle, snowfall, and ice type. It is assumed that surface air temperature will be available with a measurement uncertainty of 0.6 K.

Table 15. Ice Age Probability of Correct Typing, Case 1 (Night, Light Snowfall)

Scan Angle	Ice Age Type	
	New or Young	First Year or Multi-year
Nadir	.841	.907
Edge of Scan	.823	.894

Table 16. Ice Age Probability of Correct Typing, Case 2 (Night, Average Snowfall)

Scan Angle	Ice Age Type	
	New or Young	First Year or Multi-year
Nadir	.777	.737
Edge of Scan	.762	.723

Table 17. Ice Age Probability of Correct Typing, Case 3 (Night, Heavy Snowfall)

Scan Angle	Ice Age Type	
	New or Young	First Year or Multi-year
Nadir	.721	.637
Edge of Scan	.705	.628

The wide range in EDR performance indicates the sensitivity to snow depth.

We also performed an energy balance error analysis from a MODIS scene. The scene is a terminator scene obtained on September 30, 2002 at 0825 UT. The scene covers an Arctic Sea region that includes the North Pole. We retrieved ice thickness and ice age with our energy balance algorithm. We then perturbed the input data with the following errors:

Ice temperature accuracy error = 0.278K
Ice temperature precision error at nadir = 0.378K
Ice temperature precision error at edge of scan = 0.508K
Surface air temperature precision error = 0.6K
Snow depth error = 50% of truth
Surface wind error = 10% of truth
Surface humidity error = 5% of truth
Surface pressure error = 5% of truth

We retrieved ice thickness and ice age with the perturbed input data, and compared the results to the results from our retrieval with the unperturbed data. The resulting probability of correct typing for a nadir view is shown in Figure 18.

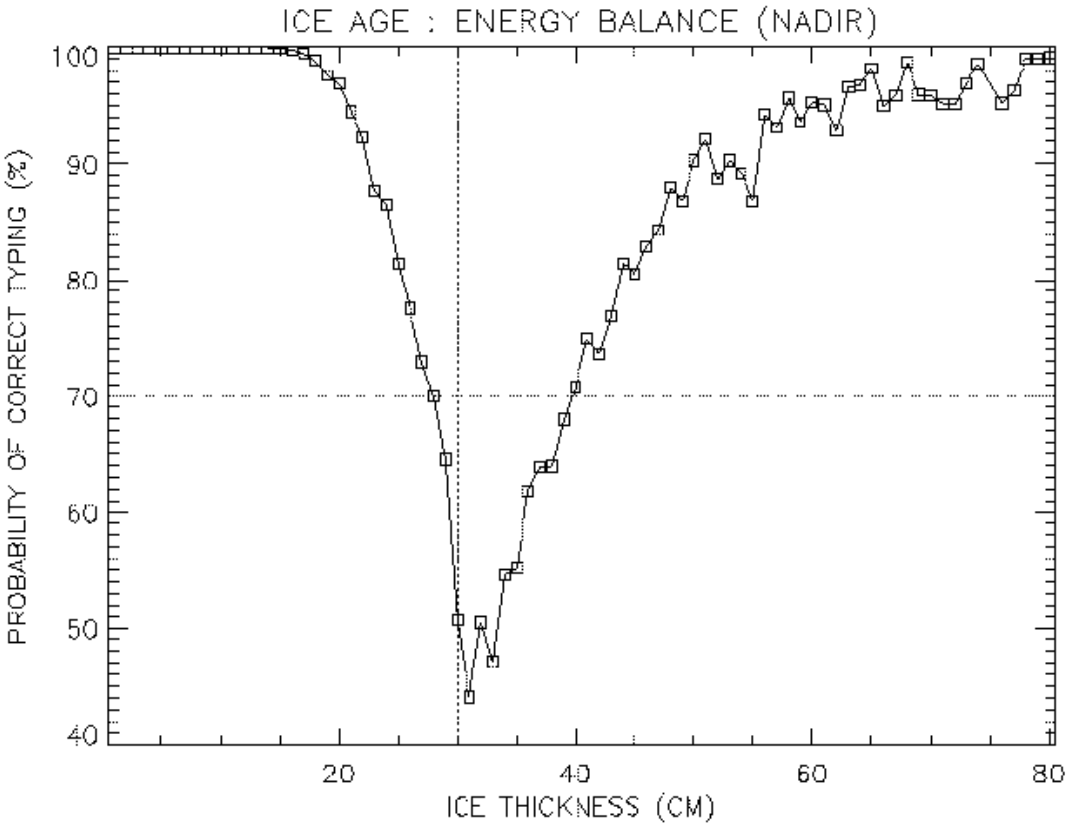

Figure 18. Probability of Correct Typing from Energy Balance (Nadir view)

Figure 18 displays the expected behavior. For very thin ice or very thick ice, there is a high probability of correctly typing the ice as New/Young or First Year/Multi-year respectively. The vertical dashed line in Figure 18 indicates the threshold ice thickness of 30 cm. Thinner ice is New/Young. Thicker ice is First Year/Multi-year. The horizontal dashed line indicates the performance requirement (70% Probability of Correct Typing) in the NPOESS System Specification. It can be seen that the performance drops below the requirement for ice thickness near 30 cm. This is an inevitable characteristic of any binary classification scheme, since the probability must be 50% when the true ice thickness equals the threshold value. The necessity for good performance is that the Probability of Correct Typing rises rapidly when the true ice thickness deviates from the threshold value. This behavior can be seen in Figure 18. The mean Probability of Correct Typing for the entire range of ice thickness is 87.6%. The mean Probability of Correct Typing of New/Young ice is 92.3%. The mean Probability of Correct Typing of First Year/Multi-year ice is 84.1%.

The performance for an edge of scan view is only slightly degraded, because the dominant error source (snow depth) does not depend on swath position. The mean Probability of Correct Typing for the entire range of ice thickness is 86.5%, compared with the nadir view result of 87.6%. The mean Probability of Correct Typing of

New/Young ice is 91.8%, compared with the nadir view result of 92.3%. The mean Probability of Correct Typing of First Year/Multi-year ice is 82.6%, compared with the nadir view result of 84.1%.

A comparison of the performance analysis from the MODIS scene to that from the MAS scene for average snowfall (Table 31) shows that the performance estimate from the MODIS scene is significantly better. We believe that the performance analysis from the MODIS scene is a better indicator of current algorithm performance, for several reasons. The MAS scene errors tabulated in Table 16 are errors averaged over the actual distribution of ice thickness in the MAS scene. This distribution may have been skewed toward the 30 cm threshold value, because we selected a MAS scene that contained ice near the threshold. The MODIS scene contains a broader distribution of ice thickness, more representative of typical conditions. In addition, the snow depth derivation has been improved since CDR, and the ancillary data for the MODIS scene comes from actual NCEP sources.

4.1.2.2 Classification from Reflectance Threshold

Verification of performance was by analysis. Ice thickness is calculated from a modeled ice thickness/reflectance relation obtained from the Ice Reflectance LUT. We identify three sources of error:

1) Derived ice reflectance (ice tie point)
2) Snow depth
3) Modeled ice reflectance

These sources of error contribute to an error in derived ice thickness, from which a classification error can occur.

Derived ice reflectance: To estimate the error in derived ice reflectance, we re-write the ice concentration error formula (equation 4.1.1.2), as:

$$\sigma^2_I = ((I-W)^2 \sigma^2_C - \sigma^2_R - (1-C)^2 \sigma^2_w) / C^2 \quad (4.1.3.1)$$

Where:

σ^2_I = error in derived ice reflectance
I = ice reflectance (tie point)
W = water reflectance (tie point)
σ^2_C = ice concentration error
σ^2_R = error in observed TOA reflectance
C = ice concentration
σ^2_w = error in derived water reflectance

Because the ice concentration error is stratified by ice concentration "truth" (C), we can simplify equation 4.1.3.1 by setting C=1 and using σ^2_C for the C=1 case:

$$\sigma^2_I = (I-W)^2 (\sigma^2_C)' - \sigma^2_R \quad (4.1.3.2)$$

where $(\sigma^2_C)'$ is the ice concentration error when ice concentration "truth" = 1.

The ice reflectance will depend on many factors, including band, ice thickness, snow depth, BRDF, and atmospheric conditions. We choose to simplify our analysis by averaging over all conditions except ice thickness. We therefore approximate the ice reflectance by:

$$I = 0.23 + 0.32 * (H / 30 \text{ cm}) \quad (4.1.3.3)$$

Where H = ice thickness. Note that σ^2_I, and therefore ice age error, will depend on H. We assume an even distribution of "true" ice thickness to compute the ice reflectance error.

We adopt a water reflectance, W = 0.07.

The ice concentration error $(\sigma^2_C)'$ is taken from Table 22. We use the third row (MODIS error = 2 * VIIRS error as our estimator, and adopt the error for the C=0.85-1.0 stratification ($(\sigma^2_C)' = 0.07$).

Errors in observed TOA reflectance are caused primarily by calibration bias and sensor noise. We adopt a total error of $\sigma^2_R = 0.02$.

Combining all of these factors, and applying equation 4.1.3.2, we derive an ice reflectance error $\sigma^2_I = 0.021$.

Snow depth: As discussed in Section 4.1.3.2, we adopt a snow depth error = 0.5 * the value obtained from climatology.

Modeled ice reflectance: The model ice reflectance is computed from the 6S and DISORT RTMs for a range of snow depths, ice thickness, atmospheric conditions, and solar/viewing angles and stored in an Ice Reflectance LUT (c.f. Section 3.3.1.3). The error in modeled ice reflectance will depend on the range of these contributing factors. The estimate of these errors is discussed in Appendix A. We adopt an error averaged over all conditions of 5%.

Probability of correct typing: The New/Young vs. First Year classification error from reflectance is presented as probability of correct typing. We estimate Probability of Correct Typing by performing the retrieval on a MODIS scene for unperturbed and perturbed cases, and comparing the classifications. The perturbation is made as follows:

1) We apply the estimated errors in ice reflectance to the values in the Ice Concentration IP.

2) We perturb the derived snow depth by a 50% error.

3) We apply model ice reflectance errors to the ice reflectance obtained from the LUT.

We retrieved ice thickness and ice age with the perturbed input data, and compared the results to the results from our retrieval with the unperturbed data. The resulting probability of correct typing for a nadir view is shown in Figure 19.

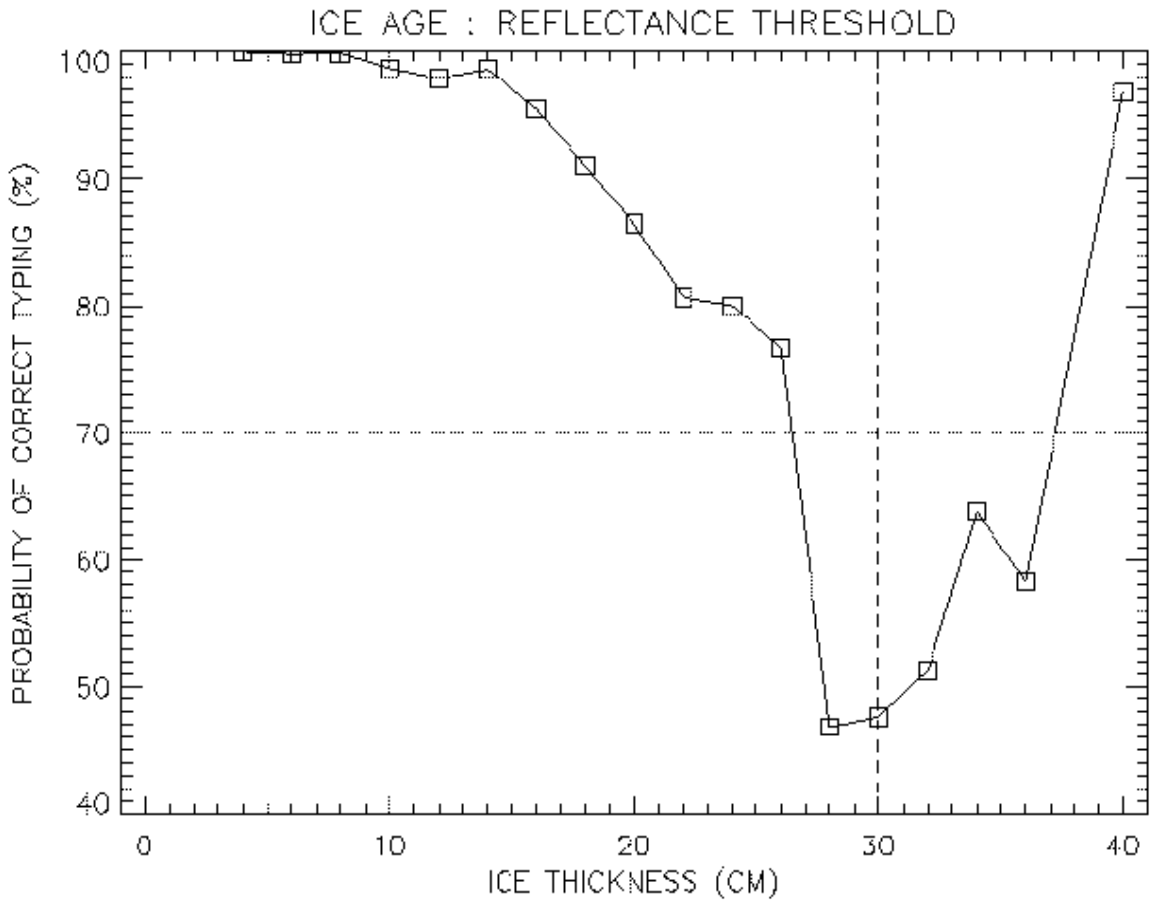

Figure 19. Probability of Correct Typing from Reflectance Threshold

Figure 19 displays the expected behavior. For very thin ice or very thick ice, there is a high probability of correctly typing the ice as New/Young or First Year/Multi-year respectively. The vertical dashed line in Figure 19 indicates the ice thickness of 30 cm. Thinner ice is New/Young. Thicker ice is First Year/Multi-year. The horizontal dashed line indicates the performance requirement (70% Probability of Correct Typing) in the NPOESS System Specification. It can be seen that the performance drops below the requirement for ice thickness near 30 cm. This is an inevitable characteristic of any binary classification scheme, since the probability must be 50% when the true ice thickness equals the threshold value. The necessity for good performance is that the Probability of Correct Typing rises rapidly when the true ice thickness deviates from the threshold value. This behavior can be seen in Figure 19. The mean Probability of Correct Typing for the entire range of ice thickness is 86.7%. The mean Probability of Correct Typing of New/Young ice is 87.1%. The mean Probability of Correct Typing of First Year/Multi-year ice is 86.4%.

Table 18 shows the probability of correct typing stratified by ice thickness.

Table 18. Ice Age from Reflectance Threshold: Probability of Correct Typing

Ice Thickness	5 – 16 cm	16 - 20 cm	20 - 24 cm	24 - 32 cm	32 - 36 cm	> 40 cm
Probability of Correct Typing	98.6%	91.4%	80.7%	55.2%	58.2%	83.5%

4.1.3 Conditions Under Which the Specification Cannot be Attained

Cloudy: VIS/IR retrievals are not feasible under cloudy conditions. The VIIRS Cloud Mask will mask cloudy pixels. Cloud error assessment will require an analysis of cloud masking performance over ice surfaces. Cloud-masked gaps in the images can be a hindrance to correlation methods. The problem is mitigated by the application of an accurate cloud mask, and the de-weighting of pixels that are cloud masked in either member of the image pair.

Melt Conditions: During the summer, air temperatures rise above freezing and the ice sheet forms melt ponds. This algorithm assumes the absence of melt ponds (i.e., a condition where there are distinct layers of ocean water, ice, snow, and air).

Heavy Snowfall (New/Young versus First Year): If recent snowfall has been greater than 6 cm/month, snow depth errors will degrade performance

Low Light During Summer: A reliance on solar reflectance bands suffers from limitations during low light conditions. A solar zenith angle threshold will be applied to flag pixels with suspect quality due to low light. We expect that atmospheric correction error will drive the setting of a solar zenith angle threshold. The threshold will depend on region and season, as atmospheric conditions dictate.

Low thermal contrast at night: The thermal contrast between ice and open water is too low during the summer and part of other seasons to allow for ice age derivations from thermal bands.

Ice Thickness near 30 cm: Probability of correct typing between New/Young and First year/Multi-year ice must approach 50% as the ice thickness approaches the threshold value of 30 cm. It must be understood that performance requirements apply to a range of ice thickness.

4.2 PRACTICAL CONSIDERATIONS

4.2.1 Numerical Computation Considerations

The processing time for the VIIRS Sea Ice algorithm must be fast enough to meet the latency requirement of 8 hours (c.f. Table 50.1 in the NPOESS System Specification).

This means that the VIIRS Sea Ice Characterization EDR must be completely processed from VIIRS raw data, including calibration and geolocation, within 8 hours from the time the raw data are available. This requirement is a strong reminder that VIIRS is an operational instrument.

The challenges posed by the latency requirement are minimal. The latency requirement is much less stringent than the 20 minute requirement listed in the Sensor Requirements Document prior to Critical Design Review. Our algorithm was designed to meet the pre-CDR requirement, so should not have difficulty in meeting the new requirement.

4.2.2 Programming and Procedural Considerations

All procedures are automatic, to perform in the operational environment. The EDR will be produced in an integrated software system within the VIIRS Ground Segment of the IDPS. The software is composed of a set of independent testable units. These include the Ice Quality, Ice Concentration, and Ice Age Units. The software designs relevant to these units are summarized in the VIIRS Context Level Software Architecture *[Y2469]*, Snow Ice Module Level Software Architecture *[Y2477]*, Ice Quality Unit Level Detailed Design *[Y0011649]*, Ice Concentration Unit Level Detailed Design *[Y3235],* and Ice Age Unit Level Detailed Design *[Y3231]*. These designs will be tested at the system level as described in the most recent versions of the VIIRS Software Integration and Test Plan *[Y3236]*, Algorithm Verification and Validation Plan *[Y3237]*, and System Verification and Validation Plan *[Y3270]*. A summary of the ultimate strategy for operational application of the system of VIIRS algorithms is provided in the VIIRS Operations Concept document *[Y2468]*. The VIIRS Interface Control Document (ICD *[Y2470]*) provides more detail on the specifics of ancillary data requirements for VIIRS EDR products.

4.2.3 Configuration of Retrievals

The algorithm requires the availability of input data from a variety of sources, including VIIRS SDRs, VIIRS IPs, and a number of LUTs. A detailed list of these sources can be found in the Build SDR Module Level Software Architecture *[Y2479]*, Snow Ice Module Level Software Architecture *[Y2477]*, Ice Quality Unit Level Detailed Design *[Y0011649]*, Ice Concentration Unit Level Detailed Design *[Y3235],* and Ice Age Unit Level Detailed Design *[Y3231]*. The EDR is not needed as input ancillary data by any other algorithm in the VIIRS system. The NPOESS/VIIRS processing configuration is designed to satisfy these expectations *[Y2469].*

4.2.4 Quality Assessment and Diagnostics

Quality flags will be attached to the EDR. Ice concentration flags are at the imagery pixel resolution. Ice Age flags are at the horizontal cell resolution. A description of the quality flags can be found in the detailed design documents.

4.2.5 Exception Handling

The software is designed to handle a wide variety of processing problems, including bad and missing data and fatal errors. The Sea Ice Age algorithm will utilize thermal data and the thermal algorithm branches for pixels with good surface temperature tie points but bad I1 and I2 reflectance tie points. In the event that processing problems prevent the production of useful EDR data, error flag information will be written to the output EDR file as metadata.

4.3 VALIDATION

Validation of the Sea Ice Characterization EDR will be conducted as part of the VIIRS System Verification and Validation Plan *[Y3270]* and the VIIRS Cal/Val Plan, and should be coordinated with the National Ice Center, with the purpose of assuring that the VIIRS data products can be incorporated into their strategic product.

Polar atmosphere radiative transfer models including an Arctic haze component will be applied to large solar zenith angle data to optimize the models for polar conditions. MODIS data taken at solar zenith angles greater than 70 degrees will be studied to assist in determining the reflectance band weighting function. The limiting factor is believed to be the reliability of atmospheric correction at larger solar zenith angles. Plane parallel radiative transfer algorithms are inaccurate for angles greater than 70-75 degrees. Development of improved radiative transfer models at larger angles will allow us to relax this constraint. To solve the Radiative Transfer Equation appropriately one would have to take into account the spherical shell atmosphere geometry (Thomas and Stamnes, 1998). It is expected that “truth” can be established from *in situ* data obtained from MODIS validation campaigns.

The pre-launch plan includes sensitivity studies, analysis of simulated VIIRS data, and verification using MODIS data. Observations from the Airborne Visible/Infrared Imaging Spectrometer (AVIRIS), MAS, MODIS, Global Imager (GLI), and NPP/VIIRS will be used in the pre-launch phase to study the error characteristics and optimum techniques for the algorithm. It is expected that MODIS validation data will be of great value. The NPP/VIIRS will be critical in adjusting and verifying the values of the parameters in our LUTs. This process will be essential in making the algorithm operational prior to the NPOESS mission. We recommend an NPP/VIIRS validation campaign that includes *in situ* field measurements, ER-2 under flights (AVIRIS and MAS), and low-level aircraft measurements at spatial resolutions as fine as 10 meters (e.g. RC-10 camera data). NPP/VIIRS data can be re-processed many times with various combinations of band weight functions and search window parameters, and resulting ice concentration and edge location can be compared to “truth” established from the auxiliary data. In this way, optimum band weight functions and search window parameters can be selected.

Creation of snow depth LUTs will be accomplished from regional/seasonal climatological histories of snow precipitation and air temperature, to support nighttime discrimination of New or Young ice from First year ice. Creation of thickness/reflectance LUTs will support daytime discrimination of New or Young ice from First year ice.

Our plan is designed to interface smoothly with post-launch validation activity. The availability of NPP/VIIRS data prior to the NPOESS mission will be of enormous benefit. We would propose to conduct an NPP/VIIRS validation campaign similar to the MODIS validation activity, and use it as a model for the post-launch NPOESS/VIIRS validation campaign. In this sense, post-launch validation will already have been simulated by the pre-launch validation activity. Following launch, we would substitute real VIIRS data for the pre-launch simulated data. Cross-validation with NPOESS/CMIS will provide a

highly valuable extra capability. Cross-validation with RADARSAT, when possible, will also be valuable.

The potential for VIIRS/CMIS data fusion to produce First Year/Multi-year classification can be studied with the use of MODIS data and Advanced Microwave Scanning Radiometer (AMSR) data. We expect our pre-launch MODIS/AMSR validation activity to merge smoothly with VIIRS/CMIS validation. We expect that MODIS/AMSR ground truth resources will be maintained for the VIIRS post-launch validation. Our use of a Previous Ice Age IP derived in part from CMIS ice age retrievals is a step in the direction of a comprehensive combined Vis-IR/passive microwave retrieval.

5.0 ASSUMPTIONS AND LIMITATIONS

5.1 ASSUMPTIONS

The statements and conclusions in this document are subject to the validity of the following assumptions:

1) An effective cloud mask over snow and ice surfaces will be available from the VIIRS Cloud Mask IP *[Y2412]*.

2) TOA reflectance will be derived from TOA radiance and supplied by the VIIRS 375 m SDR, with errors as specified in the VIIRS Radiometric Calibration Basis Document ATBD *[D43777]*

3) Surface temperature will be derived from TOA radiance and supplied as a Surface Temperature IP, with errors as specified in the VIIRS Ice Surface Temperature ATBD *[D43761]*

4) Directional reflectance corrections for a variety of shallow snow cover over thin ice will be available from look up tables. The generation of these look up tables is a required initialization activity.

5.2 LIMITATIONS

The following limitations apply to the algorithm described in this document:

- ***Clouds:*** The specified performance applies to clear conditions only. The definition of "clear" will be developed in coordination with the development of the VIIRS Cloud Mask IP *[D43766]*. Our Ice Quality process de-weights pixels with cloud cover. Pixels with thin cloud cover are partially de-weighted. These pixels are still process, but a quality flag is set to warn of degraded performance.
- ***Season:*** In the summer there is no significant contrast between surface temperature for different ice types or even open water. Retrieval from thermal bands will not be reliable under these conditions. The EDR specification includes a provision that specified EDR performance is not guaranteed when the thermal contrast between ice and open water is less than 2.2K, and that there is no useful result when the thermal contrast is less than 1.5K (TBR). Moreover, reflectance becomes non-informative in the summer time also. The cases where reflectance is non-informative are correlated with the cases where there is low thermal contrast between ice and open water. Operationally, it may be useful to exclude all pixels with surface temperature greater then 1.5K below freezing.
- ***Snow Cover:*** Deep snow cover on the ice sheet is perhaps the greatest impediment to Vis-IR retrieval of ice age. Snow depths greater than 3-4 cm completely mask the reflectance properties of the underlying ice sheet. Because snow conductivity is seven times smaller than ice conductivity, uncertainty in snow depth results in a

seven times larger uncertainty in ice thickness derived from energy balance. We addressed this problem in Section 4.1.3.2. The NPOESS System Specification includes a provision that the ice age EDR performance will be degraded when there has been heavier than usual recent snowfall.

6.0 REFERENCES

Boardman, D. *et al*., “Development of a sea-ice workstation for the automated monitoring of sea ice,” *Polar Record,* 31(177), 155 – 160, 1995.

Bohren, C.F., and B.R. Barkstrom (1974). Theory of the optical properties of snow. *J. Geophys. Res.*, 79, 4527-4535.

Bolsenga, S.J., “Spectral reflectances of snow and fresh-water ice from 340 through 1100 nm,” *J. Glaciology,* 29(102), 296-305, 1983.

Bromwich, D.H. and Tzeng, R.-Y., “Simulation of the modern arctic climate by the NCAR CCM1,” *J. Climate,* 7, 1050-1069, 1994.

Crane, R.G. and M.R. Anderson (1984). Satellite discrimination of snow/cloud surfaces. *Intl. J. Remote Sens*., 5(1), 213-223.

De Abreu, R.A., D.G. Barber, K. Misurak, and E.F. LeDrew, “Spectral albedo of snow-covered first-year and Multi-year seaice during spring melt,” *Ann. Glaciology, 21,* 337-342, 1995.

Dozier, J. (1984). Snow reflectance from Landsat-4 Thematic Mapper. *IEEE Trans. Geosci. Remote Sens.*, 22(3), 323-328.

Dozier, J. (1989). Spectral signature of alpine snow cover from the Landsat Thematic Mapper. *Remote Sens. Environ*., 28, 9-22.

Eppler, D.T., Farmer, L.D., Lohanick, A.W. *et al.*, “Passive microwave signatures of sea ice,” in Microwave Remote Sensing of Sea Ice, Geophysical Monograph 68, American Geophysical Union, 47-71, 1992.

Grenfell, T.C., D.K. Perovich, and J.A. Ogren (1981). Spectral albedos of an alpine snowpack. *Cold Regions Sci. Technol*., 4, 121-127.

Grenfell, T.C. and G. Maykutt, “The optical properties of ice and snow in the Arctic Basin, *J. Glaciology, 18*, 445-463, 1977.

Hall, D.K., Foster, J.L., Chang, A.T.C., and Rango, A., “Freshwater ice thickness observations using passive microwave sensors,” *IEEE Trans. Geosci. Remote Sens.,* GE-19(4), 189-193, 1981.

Hall, D.K., Fagre, D.B., Klasner, F., Linebaugh, G., and Liston, G.E., “Analysis of ERS-1 synthetic aperture radar data of frozen lakes in northern Montana and implications for climate studies,” *J. Geophys. Res.,* 99(C11), 22,473-22,482, 1994.

Jeffries, M.O., Morris, K., and Weeks, W.F., “Structural and stratigraphic features and ERS-1 synthetic aperture radar backscatter characteristics of ice growing on shallow

lakes in NW Alaska, winter 1991-1992," *J. Geophys. Res.,* 99(C11), 22,459-22,471, 1994.

Lee, J.S. and I. Jurkevich, "Segmentation of SAR images," *IEEE Trans. On Geoscience and Remote Sensing, 27,* 674-680, 1989.

Lee, J.S., "A simple speckle smoothing algorithm for synthetic aperture radar images," *IEEE Trans. On Systems, Man, and Cybernetics, 13,* 85-89, 1983.

Lindsay, R. and Rothrock, D., "The calculation of surface temperature and albedo of Arctic sea ice from AVHRR," *Ann. Glaciology,* 17, 1993.

Lythe, M., A. Hauser, and G. Wendler, "Classification of sea ice types in the Ross Sea, Antarctica from SAR and AVHRR imagery," *Int. J. Remote Sensing, Vol.20, No 15 & 16,* 3073-3085, 1999.

Massom, R. and Comiso, J.C., "The classification of Arctic sea ice types and the determination of surface temperature using AVHRR data," *J. Geophys. Res.,* 99(C3), 5201-5218, 1994.

Partington, K. C. and Steffen, K., "Proposed development of a joint scientific-operational Arctic-wide sea ice product," National Ice Center White Paper, 1998.

Planet, W.G. (ed.), (1988). Data extraction and calibration of TIROS-N/NOAA radiometers. NOAA Technical Memorandum NESS 107 – Rev. 1, Oct. 1988. 130 pp.

Smith, D.M., E.C. Barret, and J.C. Scott, "Sea ice type classification from ERS-1 SAR database on gray level and texture information," *Polar Record, 31,* 135-146, 1995.

Thomas, G. and Stamnes, K., "Radiative Transfer in the Atmosphere and Ocean," textbook, in press, Cambridge Atmospheric and Space Sciences Series, 1998.

Warren, S.G., "Optical properties of snow," *Rev. Geophys. Space Phys.,* 20(1), 67-89, 1982.

Warren, S.G., and W.J.Wiscombe (1980). A model for the spectral albedo of snow.II. Snow containing atmospheric aerosols, *J. Atmos. Sci.,* 37(12), 2734-2745.

Wiscombe, W.J., and S.G. Warren (1980). A model for the spectral albedo of snow,1,pure snow*. J. Atmos. Sci.,* 37(12), 2712-2733.

Yu, Y. and Rothrock, D.A., "Thin ice thickness from satellite thermal imagery," *J. Geophys. Res.,* 101(C10), 27,753 – 25,766, 1996.

APPENDIX A

Introduction

This appendix describes the quantitative assessment of errors associated with modeling top-of-atmosphere reflectance over homogeneously snow-covered surfaces. Computing reflectance over snow requires computation of reflectance from the snow surface and accounting for atmospheric scattering and absorption. For this purpose, two models are used: (1) the Discrete Ordinates Radiative Transfer (DISORT) model (Stamnes et al., 1988) and (2) the 6S atmospheric radiative transfer model (Vermote et al., 1997). Errors are associated with each model and these are addressed in separate sections below. Because of the paucity of data, this description of errors is incomplete and should not be assumed to be a full error analysis.

Before describing the various errors associated with the two models, we define the commonly used terms for reflectance, Bidirectional Reflectance Factor and Hemispherical-Directional Reflectance Factor.

Bidirectional Reflectance Factor (BRF) is defined as the ratio of upwelling radiance from a target (as measured by a detector with a specified viewing geometry) to that of a perfectly reflecting Lambertian surface. It assumes that the incident light is composed of direct beam illumination only (no diffuse illumination). This is a top-of-atmosphere reflectance quantity.

Hemispherical-Directional Reflectance Factor (HDRF) is defined as the ratio of upwelling radiance from a target (as measured by a detector with a specified viewing geometry) to that of a perfectly reflecting Lambertian surface when the incident light is composed of a combination of direct beam and diffuse sky illumination. This is a surface reflectance quantity.

It is important to distinguish between these two quantities because BRF is what is modeled in the VIIRS snow product lookup table and HDRF is what has been measured in the snow reflectance validation of the DISORT model. They are closely related quantities but should not be considered interchangeable.

Errors Associated with Radiative Transfer Model (DISORT) and It's Inputs

Snow is less anisotropic than most land cover types but unlike soils and vegetation, snow is forward scattering. In addition, because of its high reflectance in the visible and near-infrared wavelengths, this forward scattering can result in measured and modeled HDRF values that exceed 1.0.

The core of the modeling effort that creates bidirectional reflectance factor (BRF) data for the snow surface is the Discrete Ordinates Radiative Transfer (DISORT; Stamnes et al., 1988) code. DISORT is a plane-parallel radiative transfer program that is highly

versatile for modeling scattering and absorption in particulate media. It works for a wide range of the electromagnetic spectrum from the UV to the microwave. It is a one-dimensional model with the vertical coordinate expressed in optical depth. DISORT can accommodate multiple layers of particulate media. Angular coordinates, for illumination and reflection, are expressed as azimuthal angles and polar angles. The number of computational polar angles ("streams") influences the accuracy of the result. For computation of intensities, 48 streams are recommended. While the computations are performed for specific polar angles, the radiant quantities can be computed for any angle desired by the user. For a more detailed explanation of the DISORT model, see Stamnes et al., 1988.

Comparison of Modeled and Measured HDRF over Snow

There has been limited assessment of the DISORT model's ability to estimate the hemispherical directional reflectance factor (HDRF) over homogeneously covered snow surfaces. In previous work, Painter and Dozier (2004) have shown that DISORT is able to accurately characterize snow reflectance over a range of angles. Using a goniometer and high spectral resolution field spectrometer (Analytical Spectral Devices-FR), Painter and Dozier (2004) measured surface HDRF for snow under a small range of solar zenith angles. They showed that the HDRF for a snowpack consisting of fine-grained snow with faceted crystals at the surface had a local backscattering peak. Backscattering is defined as the predominance of reflection into the direction of the source of illumination. Thus, a reflectance peak in the backscattering direction means that the viewing azimuth is the same as the illumination azimuth. In this work, the backscatter peak only appeared when the viewing zenith was very close to the solar zenith angle and only for faceted snow crystals. For medium-grained snow composed of multi-grained clusters at the snowpack surface, there was no backscattering peak. As grain size increased from 80 μm to 240 μm (radius of the effective sphere), their measured HDRF values decreased at all wavelengths. However, the decrease in HDRF in the visible wavelengths was largest at a solar zenith angle ($\theta_{\sigma\upsilon\nu}$) = 80° in the forward direction and largest for wavelength (λ) > 1.8 μm near $\theta_{\sigma\upsilon\nu}$ = 30° in the backward direction. As $\theta_{\sigma\upsilon\nu}$ decreased from 47° to 41° (the range of solar zenith angles in this investigation) the HDRF increased near nadir for $\lambda \leq 1.03$ μm but decreased with coherent angular structure for $\lambda > 1.03$ μm. We compared forward radiative transfer modeling results with the HDRF measurements. The forward model used single-scattering parameters for ice spheres with radii that matched the surface-area-to-volume ratio derived from stereological analysis of snow samples and a stratigraphic distribution of optical depths from measured density and modeled extinction efficiency. All HDRF models underestimated reflectance for $\lambda > 1.30$ μm and had large errors in the perpendicular plane. Mean RMS errors in reflectance for the fine-grained, faceted snow case were 0.09 at $\lambda = 1.3$ μm and 0.14 at $\lambda = 1.85$ μm.

The Root Mean Square (RMS) errors for the medium grained, clustered snow ranged from 0.04-0.06 at $\lambda = 1.3$ μm and from 0.04-0.06 at $\lambda = 1.85$ μm. The models for the more spherical medium-grained snow had better overall spectral and angular fits than those for the non-spherical fine grain snow. The spherical radii inferred from the

surface-area-to-volume ratio from stereological analysis of snow with non-spherical particles have a greater effective path length than the actual snow particles, resulting in underestimates of HDRF.

In a second comparison of DISORT with measured HDRF, Nolin and Stroeve used a sphere-scanning radiometer over homogeneous snow cover in the Yampa Valley near Steamboat Springs, Colorado. For this assessment, data were collected using the Portable Apparatus for Rapid Acquisition of Bidirectional Observations of Land and Atmosphere, version 3 (PARABOLA-3). PARABOLA-3 measures radiance in 5^{o} viewing increments over the upward and downward hemispheres. A full spherical scan takes approximately four minutes. Reflectance is computed by ratioing the downward viewing measurements to measurements made over a calibrated Spectralon standard reflectance panel. PARABOLA-3 has eight visible and near-infrared channels plus a PAR band.

In this field experiment, data collected on several days in March 2001 from post-dawn to post-solar noon. The solar zenith angle for valid measurements ranged from 10^{o} to 45^{o}. The snowpack consisted of medium-grained (250 μm radius) spheroidal snow crystals and crystal clusters. Using snow and atmospheric properties derived from concurrent measurements, HDRF was modeled using DISORT for at the same angular resolution (5^{o} in azimuth and zenith) as the PARABOLA-3 HDRF measurements.

Figure A-1 shows the HDRF differences when the solar zenith angle is large (75^{o}).

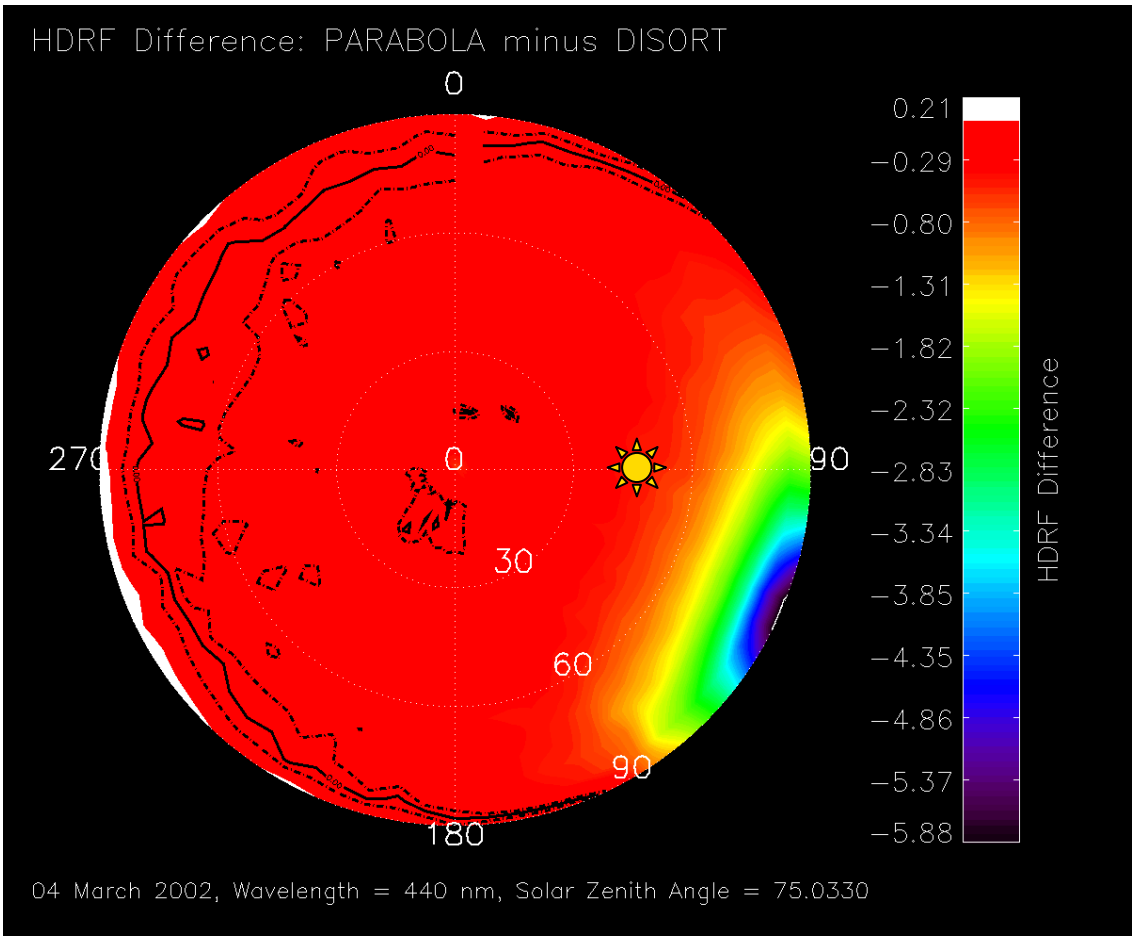

Figure A-1. HDRF difference between PARABOLA measurements and DISORT model output (wavelength=440 nm; solar illumination angle = 75 degrees).

Overestimation of the forward scattering peak is likely due to two sources 1) the model does not account for surface roughness, which has the effect of decreasing the anisotropy of the HDRF and 2) the phase function in the model does not completely characterize the scattering from snow surfaces.

The model greatly overestimates the forward scattering peak and underestimates HDRF outside of the forward peak. The PARABOLA instrument and tripod are located at the center of the Figure A-1 plot.

When the solar zenith angle is 50° or less, the HDRF differences are significantly less. Figure A-2 shows the HDRF differences when the solar zenith angle is smaller (46.6°).

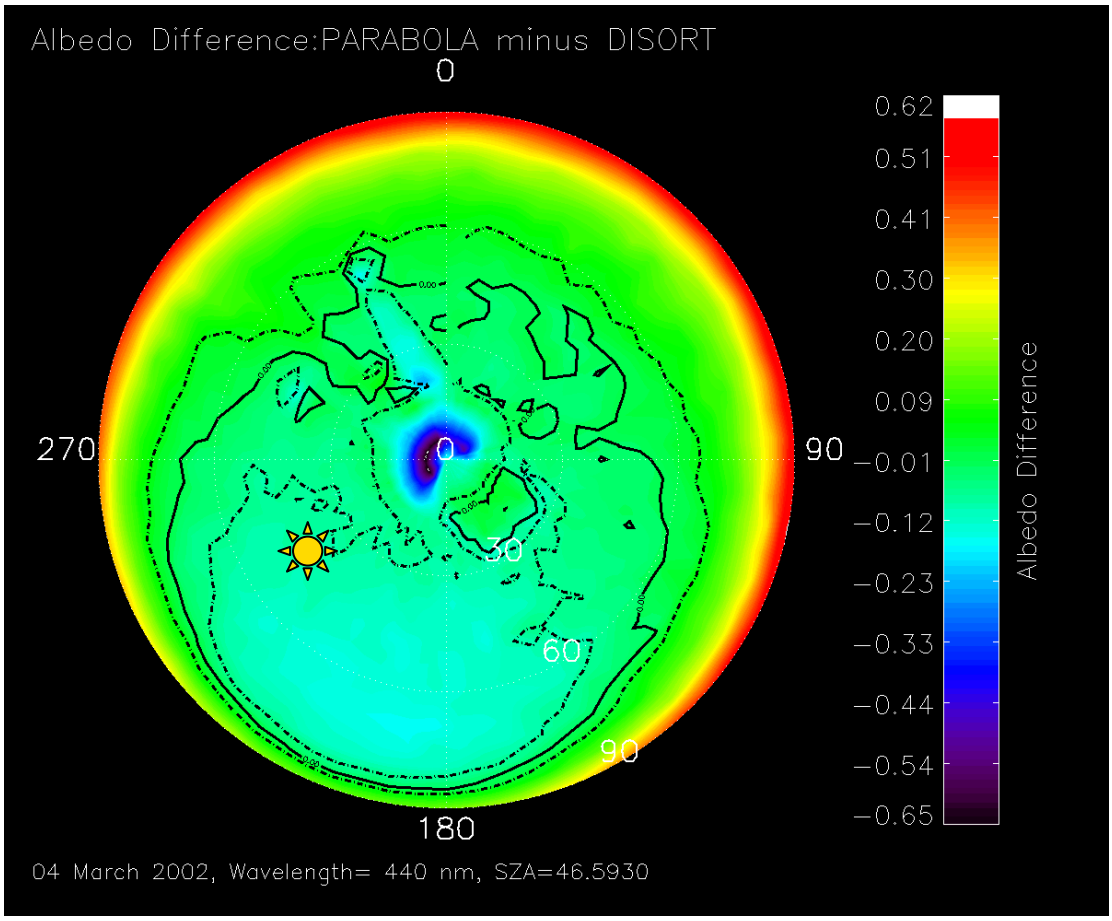

Figure A-2. HDRF difference between PARABOLA measurements and DISORT model output (wavelength = 440 nm; solar illumination angle = 46.6 degrees).

The forward scattering peak is still overestimated by the model (by about 22%) but the range of viewing angles for which the differences are less than 10% is much greater. Overall, we see that for solar illumination angles less than 60° and viewing angles less than 30 °, the reflectance is within 3% of its measured value.

Errors Associated with Atmospheric Model (6S)

This section discusses the accuracy of the atmospheric model and its impact on the VIIRS TOA reflectances in the LUTs. Both surface (e.g. modeled BRF uncertainties) and atmospheric uncertainties will contribute to uncertainties in the modeled TOA satellite reflectance. However, it is not possible to directly compare modeled VIIRS TOA bidirectional reflectance factors to measured hemispherical-directional reflectance factors. Thus, this section only gives a general estimate of the accuracy of the 6S atmospheric model in relation to ground-based measurements and the impact of uncertainties in atmospheric constituents in the model on TOA visible and near infrared reflectances.

The 6S radiative transfer model predicts the satellite signal from 0.25 to 4.0 μm assuming a cloudless and plane-parallel atmosphere. Thus, it is important to remember that the detection of clouds is critical to accurately retrieving the surface albedo from the VIIRS TOA LUTs. The main atmospheric effects considered in 6S include the following: gaseous absorption by water vapor, carbon dioxide, oxygen and ozone; scattering by molecules and aerosols. The user may select from heterogeneous or homogenous Lambertian surfaces or include bidirectional reflectances. Additional inputs into 6S include knowledge of the position of the sun and the sensor, day of the year, sensor channel (include spectral response functions) and surface and sensor elevation.

Comparison of Modeled and Measured Incoming Solar Radiation

Since we do not have a means to validate the TOA simulated VIIRS reflectance for each band, we instead opted to compare 6S-modeled to *in situ*-measured incoming solar radiation at the ETH/CU Greenland Climate Network (GC-Net) automatic weather station (AWS) on the Greenland ice sheet (Steffen and Box, 2001). This station was selected because detailed atmospheric measurements have been made during field campaigns at the station. Both downward and upward broadband shortwave radiation fluxes are measured hourly at the GC-Net AWS sites. These sites are equipped LI-COR 200SZ photoelectric diode pyranometers that measure the shortwave flux over the 0.4 μm – 1.1 μm wavelength region. The LI-COR instrument response is factory-adjusted to account for the partial spectral sensitivity under a standard atmosphere and gauges downward shortwave irradiance over the ice sheet within its 5% error specifications.

Modeled incoming solar radiation is produced using the 6S radiative transfer model. In the model simulations, an atmospheric profile based on summer radiosonde launches from the ETH/CU camp was used. This profile provides the vertical distribution of temperature and water vapor. Ozone was not measured and instead ozone distribution is taken from climatology for the Arctic. To take into consideration the effects of aerosols, a continental aerosol model and an aerosol optical depth of 0.8 is used in the model simulations (based on sun photometer measurements at the ETH/CU). Solar zenith angles are limited to a maximum of 75 degrees for which the 6S model may be considered valid and to also avoid errors in the *in situ* measurements at high solar zenith angles.

In Figure A-3, comparison between modeled and measured incoming solar radiation at ETH station (69.57°N, 49.29°W, 1149m.a.s.l.) during 2000 is shown.

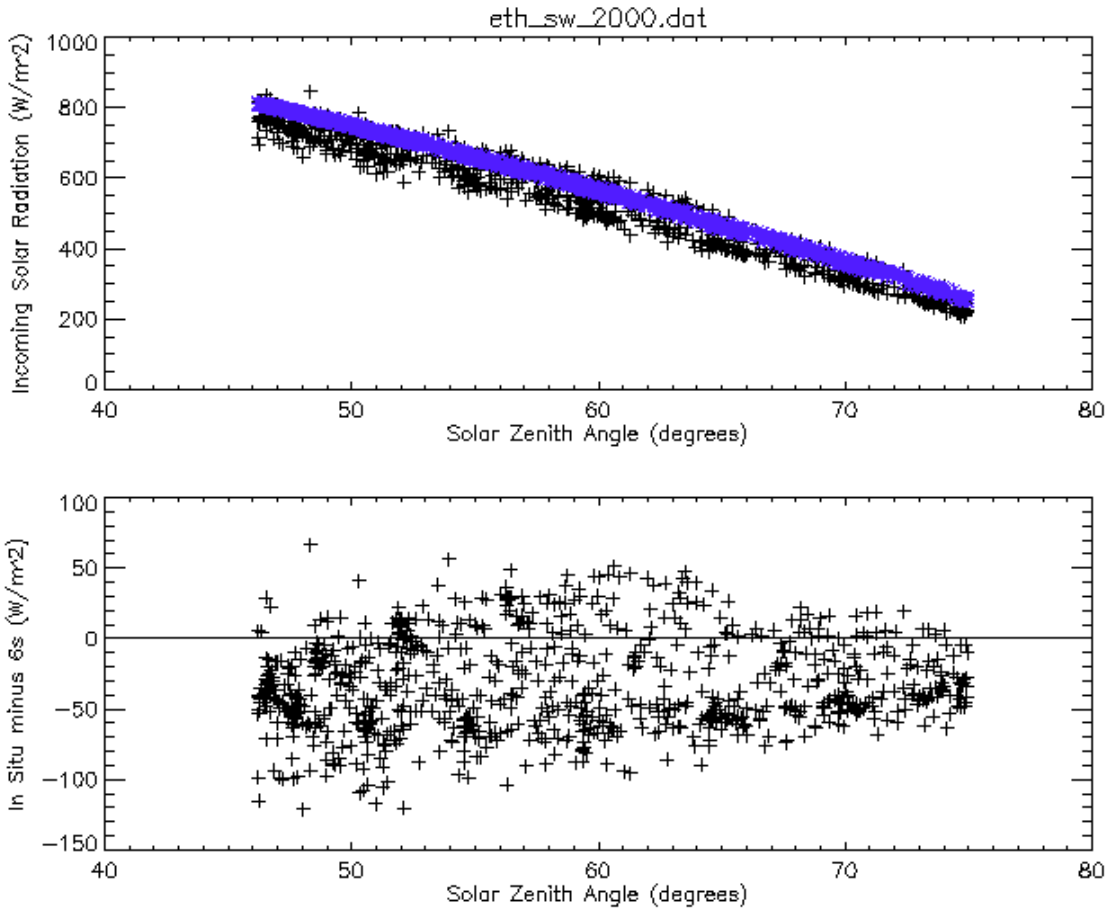

Figure A-3. Comparison between 6S modeled and station measured incoming solar radiation

The comparison shown in Figure A-3 assumed an aerosol optical depth of 0.08 and T_e > 0.8. The blue line represents the 6S modeled incoming shortwave radiation.

The blue line represents the modeled incoming solar radiation, and the black line is the measured incoming solar radiation. An attempt was made to cloud filter all the *in situ* data to avoid contamination by clouds. This method is based on radiative transfer simulations using the FluxNet radiative transfer model *(*Key and Schweiger, 1998). Effective cloud transmittance (T_e) was computed as a means of discerning clear sky conditions. T_e is defined as the ratio of measured incoming solar radiation to that computed by a radiative transfer model (Box, 1997). A value of 1.0 implies clear sky conditions. Although an increase in diffuse sky irradiance in the presence of thin clouds will cause underestimates of the true cloud amount, we aim only to discriminate between cloudy and clear conditions. The frequency distributions of T_e values suggest a threshold value of T_e > 0.8 for discriminating between clear and cloudy conditions. This method however isn't perfect so some of the large scatter seen in Figure A-3 between

the two values could be a result of clouds reducing the measured incoming solar radiation.

Figure A-4 shows that if we use $T_e > 0.9$, the scatter is reduced considerably.

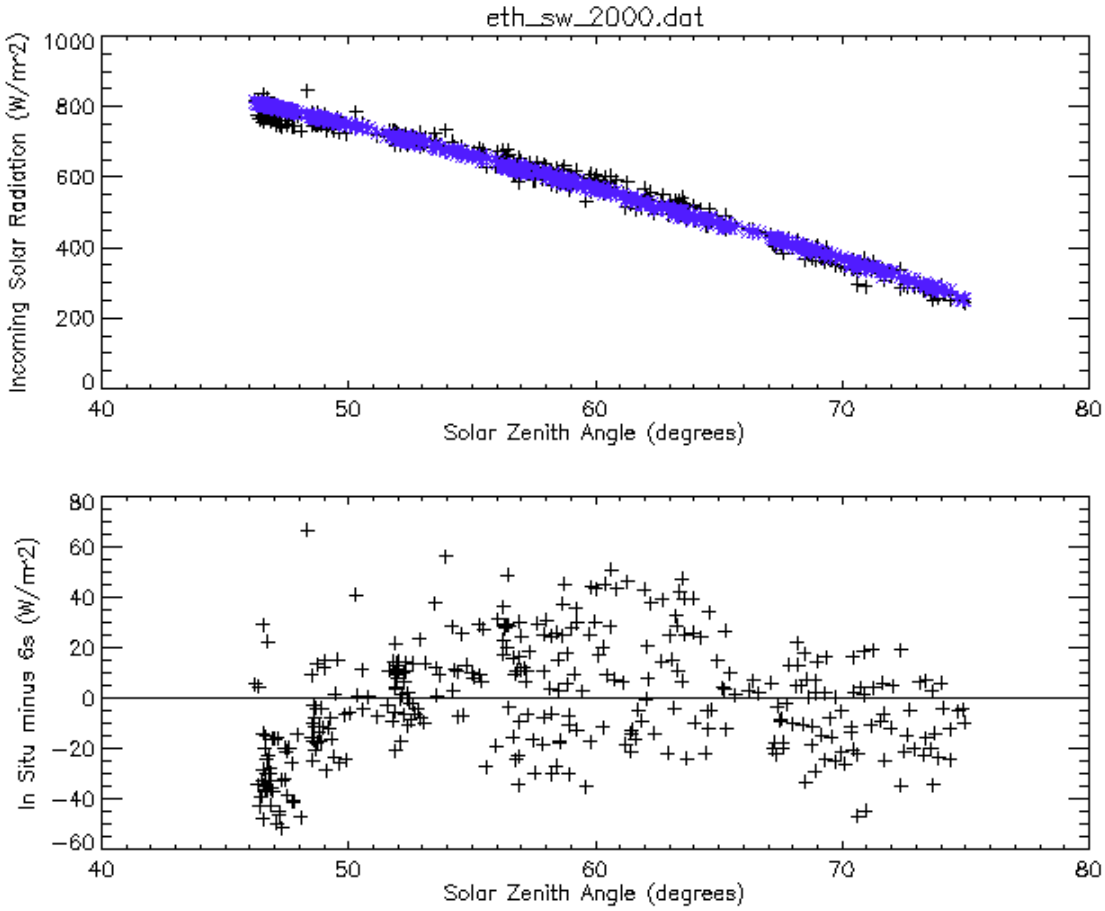

Figure A-4. Comparison between 6S modeled and station measured incoming solar radiation.

The comparison shown in Figure A-4 assumed an aerosol optical depth of 0.08 and $T_e > 0.9$. The blue line represents the 6S modeled incoming shortwave radiation.

Table A-1 summarizes the mean differences for three years (2000, 2001 and 2002) using $T_e > 0.9$ to remove the effects of clouds from the *in situ* data. On average, the 6S model overestimates the incoming solar radiation by less than 2%. The modeled incoming solar radiation matches better with the *in situ* measurements at the higher solar zenith angles than at the smaller ones in terms of absolute difference, but in terms of percent difference, the differences are larger. At times the differences can reach as high as 20%, perhaps as a result of clouds. A constant assumption of aerosol optical depth and atmospheric profile can also lead to errors when the actual atmospheric conditions are different from those observed. In general, atmospheric water vapor has a smaller impact than aerosol optical depth (see next section).

In terms of how these errors due to atmospheric conditions translate to TOA albedo we can do the following. First assume that the modeled incoming solar radiation at the ground level is in error by 2%. Next assume that the reflected solar radiation at ground level will equal the error in the incoming solar radiation. At the TOA we can assume that the reflected solar radiation will be the addition of the error in the incoming and reflected solar radiation at ground level, which is 2.8%. Larger errors would be expected in the VIIRS bands that are affected by aerosols, ozone and water vapor. Bands outside of absorption features will be less impacted.

Table A-1. Mean differences between modeled and measured incoming solar radiation at the ETH/CU AWS ($T_e > 0.9$).

Year	Mean Differences and Standard Deviation (W/m^2)	Mean in situ Incoming Solar Radiation (W/m^2)	Mean Modeled Incoming Solar Radiation (W/m^2)
2000	-1.33 $\pm$ 22.39	587.305	588.632
2001	-13.05 $\pm$ 26.79	574.117	583.053
2002	-8.03 $\pm$ 23.74	545.314	552.176

These comparisons should be considered together with comparisons between the 6S and MODTRAN radiative transfer models. Figure A-5 shows an example of model simulations for VIIRS channel I1 assuming no aerosols, nadir view, solar zenith angle of 48^{o}, and an arctic summer atmosphere of water vapor and ozone. Note however that the definition of an arctic summer atmospheric profile differs between MODTRAN and 6S. This simulation shows that the models are within 1% of each other.

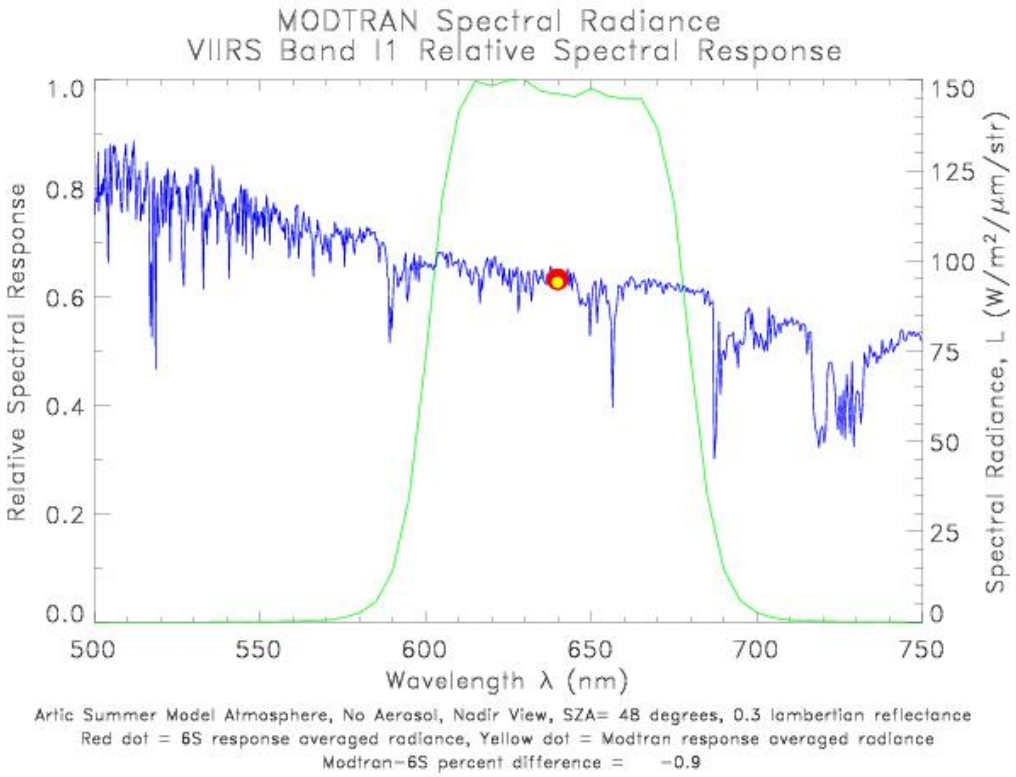

Figure A-5. Comparison between MODTRAN and 6S modeled spectral irradiance for VIIRS channel I1.

Atmospheric Sensitivity

This section discusses the sensitivity of satellite visible and near infrared radiances to atmospheric effects. Different atmospheric conditions from those used to model the VIIRS channel reflectances will impact the resulting albedo. Stroeve et al. (1997) discuss the sensitivity of AVHRR visible (channel 1) and near infrared (channel 2) radiances to variations in aerosol, water vapor and ozone optical depth. Results from this comparison study reveal that uncertainty in aerosol optical depth will have the largest impact on albedo derived from visible and near infrared satellite observations.

Over snow and ice-covered surfaces, the presence of atmospheric aerosols will tend to decrease the TOA reflectance. The decrease is greatest at high solar zenith angles and greatest for channels in the blue wavelengths. Figure A-6 shows an example of the dependence of the VIIRS M1 channel reflectance on aerosol optical depth.

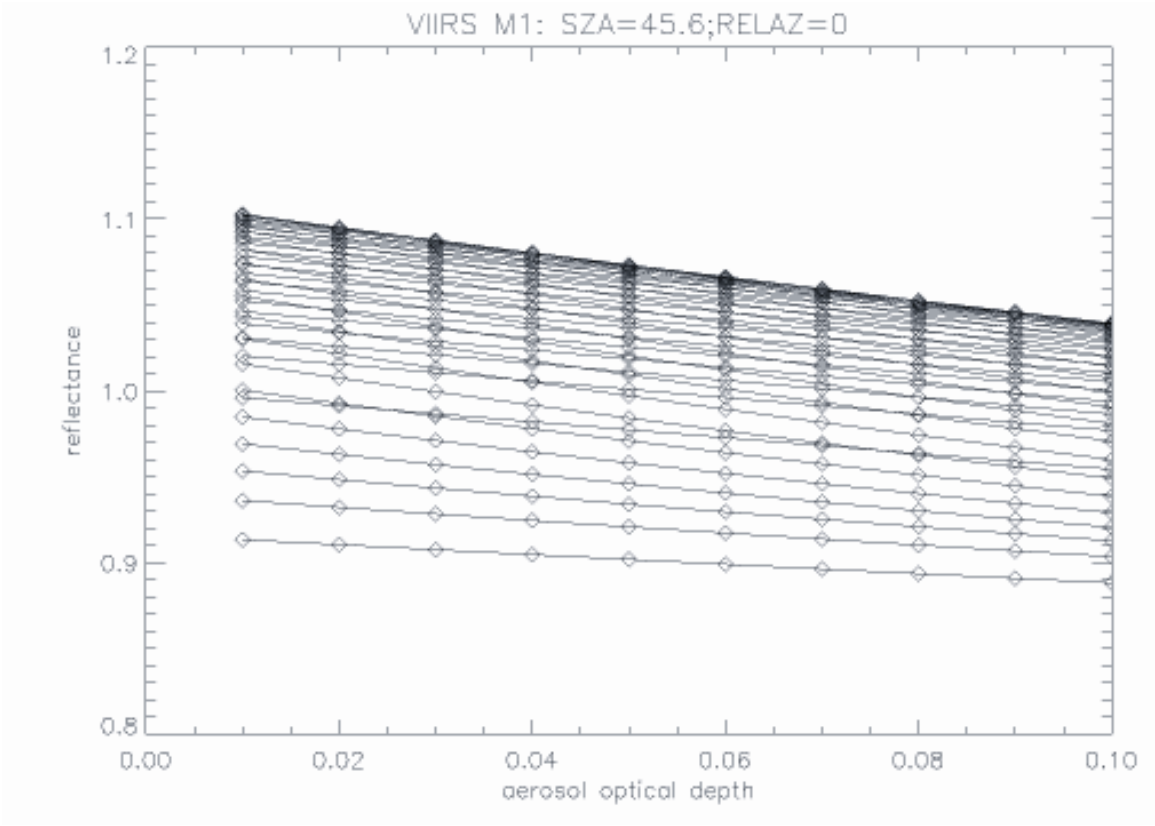

Figure A-6. Dependence of VIIRS channel M1 TOA reflectance as a function of aerosol optical depth.

Each line in Figure A-6 represents the dependence for a different sensor viewing angle, with the lowest values occurring at nadir. A continental aerosol model is assumed. Shown is the decrease in TOA reflectance as a function of aerosol optical depth and satellite viewing zenith angle. The decrease in reflectance with aerosol optical depth is stronger for more oblique viewing angles.

Table A-2 gives an example of the change in TOA reflectance for 4 different wavelengths as the aerosol optical depth increases by 0.01, assuming a solar zenith angle of 60^o and a continental aerosol model. The dependence of TOA reflectance on aerosol optical will be stronger for urban and dust-like aerosol models and weaker for maritime aerosol models.

Table A-2. Sensitivity of TOA reflectance to AOT.

Relative Azimuth Angle	**0.43 μm**	**0.55 μm**	**0.67 μm**	**0.87 μm**
180^o	0.031	0.030	0.029	0.027
100^o	0.033	0.032	0.031	0.029
0^o	0.034	0.033	0.032	0.030

Results are presented in terms of absolute albedo for a 0.01 change in aerosol optical depth using a continental aerosol model at three different relative azimuth angles, a solar zenith angle of 60^o. In general, constant values for aerosol optical depth are assumed since it is not possible to retrieve aerosol optical depths over snow and ice-covered surfaces from satellite measurements. Thus, if the aerosol optical depth has an uncertainty of 0.01 (in units of optical depth), the retrieved albedo will have an uncertainty of 0.03 (absolute albedo). In general, the polar regions have very clear atmospheres and thus the aerosol optical depths are quite low. However, Arctic haze events can significantly increase the amount of aerosols in the atmosphere. Knowledge of these events will help reduce the uncertainty of the albedo retrievals. At lower elevations, estimates of aerosol optical depths made over vegetated surfaces and extrapolated over snow-covered areas would help to reduce the uncertainty in aerosol optical depths.

Ozone and water vapor uncertainties have a much reduced impact on the retrieved albedo. However, they may still be significant. For example, running a simple test using 6S we find that there is about a 6% difference in the model-derived surface albedo assuming a surface at sea level versus a surface at 3000m. Most of this difference is caused by the difference in atmospheric water vapor between sea level and 3000m. In this regard, elevation affects should be taken into account when deriving the surface albedo from satellite observations. In addition, the seasonal variability in atmospheric water vapor should be considered.

Summary

It is not clear how the errors associated with DISORT and 6S combine to create an overall error estimate. Therefore, no accurate overall error estimate is possible. However, if one examines the possible errors in terms of their magnitude and possibility of occurrence, it is possible to make a gross error estimate. For instance, if the solar

zenith angle exceeds 60^o, the viewing zenith exceeds 30^o and sensor is viewing forward scattered radiation, then the total error will almost certainly exceed 10% simply because the errors in estimating BRF from DISORT are quite high in that angular region. For channels in the visible, if the viewing zenith is near nadir and the solar zenith angle is less than 60 degrees then DISORT errors are quite small and the predominance of errors would come from the atmospheric modeling and would be in the range of 1-6%. Although atmospheric sensitivities are lower in the near infrared part of the spectrum, overall errors in modeled BRF are higher because the DISORT model does not perform as well in this part of the spectrum (the phase function overestimates the scattering peak). Errors are roughly 50% higher in the near infrared region than they are for the visible wavelengths.

References

Box, J., (1997), Polar day effective cloud opacity in the Arctic from measured and modeled solar radiation fluxes, MA thesis, University of Colorado, Boulder, Colorado.

Key, J. and A.J. Schweiger, (1998), Tools for atmospheric radiative transfer: Streamer and FluxNet. *Computers & Geosciences*, 24(5), 443-451.

Painter, T. H., and J. Dozier (2004), Measurements of the hemispherical-directional reflectance of snow at fine spectral and angular resolution, in press, Journal of Geophysical Research-Atmospheres.

Stamnes, K., S-C. Tsay, W. Warren, and K. Jayaweera, Numerically stable algorithm for discrete-ordinate-method radiative transfer in multiple scattering and emitting layered media, Appl. Opt., 27, 2502-2509, 1988.

Steffen, K. and J. E. Box, (2001), Surface climatology of the Greenland ice sheet: Greenland Climate Network 1995-1999. *Journal of Geophysical Research*, 106(D24), 33951-33964.

Stroeve, J., A. Nolin and K. Steffen, 1997. Comparison of AVHRR-derived and *in situ* surface albedo over the Greenland ice sheet, *Remote Sensing Environment*, 62, 262-276.

Vermote E., D. Tanre, J. L. Deuze, M. Herman, and J. J. Morcrette, Second Simulation of the Satellite Signal in the Solar Spectrum, 6S User Guide, Version 2, 218pp. 1997.